University of Alberta

Multiaxial Behavior and Viscoelastic Constitutive Modeling of Epoxy Polymers

by

Yafei Hu

A thesis submited to the Faculty of Graduate Studies and Research in partial fulfillment of the requirements for the degree of Doctor of Philosophy

Department of Mechanical Engineering

Edmonton, Alberta

Fall 2002

National Library of Canada
Acquisitions and Bibliographic Services
395 Wellington Street
Ottawa ON K1A 0N4
Canada

Bibliothèque nationale du Canada
Acquisitions et services bibliographiques
395, rue Wellington
Ottawa ON K1A 0N4
Canada

Your file Votre référence

Our file Notre référence

The author has granted a non-exclusive licence allowing the National Library of Canada to reproduce, loan, distribute or sell copies of this thesis in microform, paper or electronic formats.

L'auteur a accordé une licence non exclusive permettant à la Bibliothèque nationale du Canada de reproduire, prêter, distribuer ou vendre des copies de cette thèse sous la forme de microfiche/film, de reproduction sur papier ou sur format électronique.

The author retains ownership of the copyright in this thesis. Neither the thesis nor substantial extracts from it may be printed or otherwise reproduced without the author's permission.

L'auteur conserve la propriété du droit d'auteur qui protège cette thèse. Ni la thèse ni des extraits substantiels de celle-ci ne doivent être imprimés ou autrement reproduits sans son autorisation.

0-612-81201-4

Canada

University of Alberta

Library Release From

Name of Author: Yafei Hu

Title of Thesis: Multiaxial Behavior and Viscoelastic Constitutive Modeling of Epoxy Polymers

Degree: Doctor of Philosophy

Year this Degree Granted: 2002

Permission is hereby granted to the University of Alberta Library to reproduce single copies of this thesis and to lend or sell such copies for private, scholarly or scientific research purposes only.

The author reserves all other publication and other rights in association with the copyright in the thesis, and except as herin before provided, neither the thesis nor any substantial portion may be printed or otherwise reproduced in any material form whatever without the author's prior written permission.

Yafei Hu
607C, Michener Park
Edmonton, AB T6H 5A1
CANADA

Sept. 27, 2002

University of Alberta

Faculty of Graduate Studies and Research

The undersigned certify that they have read, and recommended to the Faculty of Graduate Studies and Research for acceptance, a thesis entitled Multiaxial Behavior and Viscoelastic Constitutive Modeling of Epoxy Polymers by Yafei Hu in partial fullfilment of the requirements for the degree of Doctor of Philosophy.

Dr. Z. Xia (Supervisor)

Dr. F. Ellyin (Co-supervisor)

Dr. C. Ru

Dr. W. Chen

Dr. G. Thornton

Dr. C.T. Sun (External Examiner)

Dated: Sept. 27, 2002

ABSTRACT

Polymers play an increasingly important role in critical load-bearing structures. An efficient design and effective material utilization usually require a good understanding and modeling of the nonlinear deformation behavior of the polymers involved. The present research is aimed at characterizing and modeling the multiaxial nonlinear deformation behavior of epoxy polymers.

A series of creep and constant loading rate tests were conducted for two epoxy systems at different stress states at ambient temperature. Those tests can be generally divided into two groups which deal with different aspects of the mechanical behavior of epoxy polymers. One group is related to the deformation behavior such as viscoelastic behavior, hydrostatic stress effect, multiaxial behavior, as well as loading path effect. The second group deals with the failure behavior including failure modes and failure stress envelopes. These results provide an ample resource of data for the development and verification of constitutive models for polymers.

Based on the experimental data, a new nonlinear viscoelastic constitutive model, in differential form, is presented. A distinctive feature of this model is the inclusion of a criterion to delineate loading and unloading in multiaxial stress states, and different moduli for loading and unloading behavior. In addition, the model contains only five material constants and one modulus function, which can be calibrated in accordance with a well standard procedure.

A comparison with the experimental data shows that the current differential model is capable of predicting the deformation characteristics of the two epoxy polymers, including both the loading and unloading behavior. The predictions of an integral form of constitutive model are also included for a comparative purpose.

Acknowledgements

I wish to express my sincere appreciation to Dr. Zihui Xia and Dr. Fernand Ellyin for giving me the opportunity to pursue my Ph.D. in their research group and their invaluable guidance, stimulating discussion and financial support throughout this endeavor.

I also would like to thank the member of my supervisory committee: Dr. Chongqing Ru for useful and constructive interactions, and my examination committee: Dr. Weixing Chen, Dr. Gail Thornton and Dr. C.T. Sun (external examiner) for their time, effort and an excellent feedback to my thesis.

Gratitude is extended to all my past and current colleagues of the Department of the Mechanical Engineering, who have contributed in one way or another to the completion of this dissertation, in particular to Dr. John Wolodko for his help in the sample preparation and multiaxial testing system and many useful discussions, to Mr. Bernie Faulkner for his help and patient with all of my questions regarding testing equipment, to Mr. Don Fuhr, Mr. Dave Pape, and Mr. Albert Yuen for their preparation of specimens, to Raymond Suglo for his proofreading.

I am also very grateful to the members of the ACME group, past and present, for their comments, suggestions and friendship: Dr. Chingshen Li, Cecilia Grafman, Garrett Meijer, Pierre Mertiny, Dr. Yunfa Zhang, Mark Brown, Rachel Maser, and Xiangyi Zhang.

My special thanks go to my wife, Qiufang, to whom this thesis is dedicated, for her love, understanding and consistent support throughout this degree, as well as my life, and to my daughter, Vanessa (Jia), who always makes my computer go crazy.

1. Introduction 1

1.1 Polymers 4

1.2 Phenomenological Behavior 6

1.2.1 Linear viscoelastic behavior 7

1.2.2 Nonlinear viscoelastic behavior 11

1.2.3 Multiaxial behavior 17

1.3 Constitutive Modeling 19

1.3.1 Linear viscoelastic models 20

1.3.2. Nonlinear viscoelastic models 23

1.3.3 Multiaxial consideration 29

1.4 Failure Behaviors 33

1.5 Objectives of the Current Study 37

Bibliography 41

2 Test Methodology 49

2.1 Tested Materials 49

2.2 Specimen Fabrication 50

2.3 Loading Scheme and Stress State 52

2.4 Testing Facilities 58

2.5 Test Procedures 61

2.5.1 Creep tests 61

2.5.2 Hydrostatic stress effect 63

2.5.3 Multiaxial Behavior 65

2.5.4 Loading path effect 67

2.5.5 Failure tests 69

2.6 Specimen Preparation and Testing Considerations 70

2.6.1 Defect problems 70

2.6.2 Curing procedure 71

2.6.3 Creep tests 73

2.6.4 Reproducibility of experimental data 75

2.6.5 Physical aging effect 77

Bibliography 78

3 Mechanical Behavior of EPON 826/EPI-CURE 9551 **79**

3.1 Viscoelastic Behavior 79

3.1.1 Creep and recovery tests 79

3.2. Hydrostatic Stress Effect 84

3.3. Multiaxial Behavior 85

3.3.1 Stress envelope for octahedral shear rates 86

3.3.2 Stress envelope for octahedral shear strain amplitude 88

3.4 Loading Path Effect 89

3.5 Failure Behavior 92

3.6 Concluding Remarks 100

Bibliography 101

4 Mechanical Behavior of ColdCure epoxy **102**

4.1 Viscoelastic Behavior 102

4.1.1 Creep tests 102

4.1.2 Biaxial creep 106

4.2 Hydrostatic Stress Effect 107

4.2.1 Shear stress-strain behavior under hydrostatic pressure 107

4.2.2 Shear creep under hydrostatic pressure 109

4.3 Axial-shear Interaction 110

4.3.1 Axial stress effect on shear creep 110

4.3.2 Shear stress effect on axial creep 112

4.4 Mutliaxial Behavior 112

4.4.1 Stress envelope for the same octahedral shear strain 113

4.4.2 von Mises equation 115

4.4.3 Stassi equation 117

4.5 Loading Path Effect 118

4.5.1 Strain-controlled tests 118

4.5.2 Strain-rate effect 122

4.6 Failure Behavior 123

4.7 Concluding Remarks 128

Bibliography 130

5. Development of Nonlinear Viscoelastic Constitutitive Model for Polymeric Materials **131**

5.1 Developed Differential Model 133

5.1.1 General description of the model 133

5.1.2 Description of unloading behavior 136

5.1.3 Equivalent stress representation 139

5.1.4 Determination of material constants and modulus function 140

5.2 Integral Model 141

5.2.1 Model formulation 141

5.2.2 Model calibration 143

5.3 Concluding Remarks 146

Bibliography 148

6. Model Predictions for the Mechanical Behavior of Epon 826/ EPI-CURE 9551 Epoxy System **150**

6.1 Model Constants and Functions 150

6.1.1 Differential model 150

6.1.2 Integral model 152

6.2 Comparison of Predicted Results with Experiments 153

6.2.1 Creep and recovery tests 153

6.2.2 Multiaxial behavior 156

6.2.3 Proportional loading paths 158

6.2.4 Non-proportional loading paths 159

6.2.5 Transient loading paths 161

6.3 Unloading Behavior 167

6.3.1 Uniaxial tensileloading-unloading 167

6.3.2 Proportional loading/unloading along path O-C-O 168

6.3.3 Non-proportional loading/unloading path 170

6.4 Concluding Remarks 172

7. Mode Predictions for the Mechanical Behavior of ColdCure Epoxy System 174

7.1 Model Constants and Functions 174

7.1.1 Differential model 175

7.1.2 Integral model 175

7.2 Comparison of Predicted Results with Experiments 176

7.2.1 Creep and recovery behavior 176

7.2.2 Hydrostatic stress effect 178

7.2.3 Multiaxial behavior 181

7.2.4 Transient loading paths 183

7.2.5 Non-proportional loading paths 185

7.3 Concluding Remarks 189

8 Conclusions 191

8.1 Mechanical Behavior 191

8.2 Constitutive Modeling 193

8.3 Model Predictions 194

Table 4.1 The applied stress states for creep tests 110

Table 6.1 Nonlinear viscoelasticity parameters for differential model 152

Table 7.1 Nonlinear viscoelasticity parameters for differential model 176

Figure 1.1 Linear stress-strain behavior for typical fibers 2

Figure 1.2 Three types of polymer chains 4

Figure 1.3 The Van der Waals force between chain segments 5

Figure 1.4 Amorphous and crystalline polymers 6

Figure 1.5 Creep deformation of a viscoelastic material 8

Figure 1.6 Stress relaxation at constant strain 9

Figure 1.7 Representation of an arbitrary strain function and resulting stress response of a viscoelastic material 10

Figure 1.8 Three stages of creep deformation 12

Figure 1.9 Stress-strain-time relationship obtained from series of single step loading 13

Figure 1.10 (a) Loading program, (b) deformation and (c) direct comparison of creep $\varepsilon_c(t)$ and recovery $\varepsilon_r(t)$ for a non-linear viscoelastic solid 14

Figure 1.11 Mechanical models: (a) Maxwell model; (b) Kelvin model 21

Figure 1.12 Typical load-elongation curve for polymers 34

Figure 2.1 Thin-walled tubular specimen geometry 52

Figure 2.2 View of the multiaxial testing system 53

Figure 2.3 Description of the multiaxial testing machine components 54

Figure 2.4 Block diagram of the servo-hydraulic system 55

Figure 2.5 Block diagram of the feedback and control system 55

Figure 2.6 Strain gauge layout for tubular specimens 57

Figure 2.7 A schematic of the biaxial test apparatus 58

Figure 2.8 Loading Scheme (a) and Stress State (b) 60

Figure 2.9 Creep Isochronous experiment 62

Figure 2.10 Stress state of simple shear with superimposed hydrostatic pressure 64

Figure 2.11 Loading paths in principal strain space 65

Figure 2.12 Proportional and non-proportinal strain paths in strain space 68

Figure 2.13 Recorded temperature at the suggested curing procedure 72

Figure 2.14 Recorded temperature for a curing schedule of 50°C for 2 hours and 120°C for 2.5 hours 73

Figure 2.15 Idealized step loading (a) and ramped step loading used in practice (b) 74

Figure 2.16 (a) The strain response to a true step excitation of stress, compared with that a ramped step; (b) Discrepancy between the two responses 75

Figure 2.17 Comparison of tensile and compressive mechanical responses of two specimens at a constant $\dot{\varepsilon}_{oct}=10^{-4}s^{-1}$ for ColdCure epoxy 76

Figure 3.1 Creep and recovery curves at different stress levels 80

Figure 3.2 Recovery curves at different stress levels 81

Figure 3.3 Creep compliance curves at different stress levels 82

Figure 3.4 Poisson's ratio at the applied stress level of 45.68MPa 83

Figure 3.5 Shear stress-strain curves for $\dot{\varepsilon}_{oct}=10^{-4}\ s^{-1}$ and $\dot{\varepsilon}_{oct}=10^{-5}\ s^{-1}$ with or without a superposed hydrostatic pressure of 17.24MPa 84

Figure 3.6 Stress envelopes at three octahedral shear strain rates 86

Figure 3.7 Stress envelopes at three different octahedral shear strain values 88

Figure 3.8 Experimental axial stress-strain curves for two different loading paths with an octahedral shear strain rate of $10^{-5}s^{-1}$ 89

Figure 3.9 Experimental shear stress-strain curves for two different loading paths with an octahedral shear strain rate of $10^{-5}s^{-1}$ 90

Figure 3.10 Octahedral shear stress – strain curves for three different loading cases 91

Figure 3.11 Tensile stress-strain curves to failure at three different octahedral shear strain rates $10^{-3}\ s^{-1}$, $10^{-4}\ s^{-1}$ and $10^{-5}\ s^{-1}$ 93

Figure 3.12 Compressive stress-strain curves to failure at stress rate of 0.5MPa/s: (a) Engineering representation; (b) true representation 94

Figure 3.13 Compressive stress-strain curves to failure at three different octahedral shear strain rates $10^{-3}\ s^{-1}$, $10^{-4}\ s^{-1}$ and $10^{-5}\ s^{-1}$ 95

Figure 3.14 Shear stress-strain curves to failure at three different octahedral shear strain rates $10^{-3}\ s^{-1}$, $10^{-4}\ s^{-1}$ and $10^{-5}\ s^{-1}$ 96

Figure 3.15 Equibiaxial stress-strain curves to failure at an octahedral shear strain rate of $10^{-3}\ s^{-1}$ 97

Figure 3.16 A schematic of hydrostatic stress effect on failure modes 98

Figure 3.17 Comparison of experimental data with modified Tresca criterion 99

Figure 4.1 Creep and recovery curves at different stress levels 103

Figure 4.2 Strain curves at recovery at different stress levels 104

Figure 4.3 Compliance curves at different stress levels for ColdCure epoxy 105

Figure 4.4 Equibiaxial creep response for two stress level 106

Figure 4.5 Shear loading and unloading stress-strain curves for $\dot{\gamma} = 2\times10^{-4}\ s^{-1}$ with or without a superimposed hydrostatic pressure of 17.24MPa 108

Figure 4.6 Shear loading and unloading stress-strain curves for $\dot{\gamma} = 2\times10^{-5}\ s^{-1}$ with or without a superposed hydrostatic pressure of 17.24MPa 108

Figure 4.7 Shear creep deformations with or without a superimposed hydrostatic pressure of 17.24MPa 109

Figure 4.8 Effect of axial stress on the shear creep for two cases: Case 1: $\tau = 10$ MPa, $\sigma_a = 14$ MPa ; Case 2: $\tau = 10$ MPa, $\sigma_a = -14$ MPa 111

Figure 4.9 Effect of shear stress on the axial creep for two cases: Case 1: $\tau = 10$ MPa, $\sigma_a = 14$ MPa ; Case 2: $\tau = 0$, $\sigma_a = 14$ MPa 112

Figure 4.10 Stress envelopes at different octahedral shear strain rates 113

Figure 4.11 Stress envelope for ε_{oct}=0.8% at an octahedral shear strain rate of $10^{-4}\ s^{-1}$ 114

Figure 4.12 In-plane biaxiality regimes in terms of the principal stress and strain for axial-torsion, where υ is the Poisson ratio 116

Figure 4.13 Experimental axial stress-strain curves for two different loading paths with an octahedral shear strain rate of $10^{-4}\ s^{-1}$ 119

Figure 4.14 Experimental shear stress-strain curves for two different loading paths with an octahedral shear strain rate of $10^{-4}\ s^{-1}$ 120

Figure 4 15 Comparison of the axial stress-strain curves for two different loading path to determine the shear stress (strain) interaction effect 121

Figure 4.16 Experimental axial stress-strain curves for two different loading paths at two octahedral shear strain rates of $10^{-4}\ s^{-1}$ and $10^{-5}\ s^{-1}$ 122

Figure 4.17 Experimental shear stress-strain curves for two different loading paths at two octahedral shear strain rates of $10^{-4}\ s^{-1}$ and $10^{-5}\ s^{-1}$ 123

Figure 4.18 Tensile stress-strain curve to failure at an octahedral shear strain rate of $10^{-4}\ s^{-1}$ 124

Figure 4.19 Equibiaxial stress-strain curves to failure at two different octahedral shear strain rates $10^{-4}\ s^{-1}$ and $10^{-5}\ s^{-1}$ 125

Figure 4.20 Shear stress-strain curve to failure at the octahedral shear strain rate of $10^{-4}\ s^{-1}$ 126

Figure 4.21 Comparison of experimental data with modified von Mises criterion 127

Figure 4.22 Comparison of experimental data with modified Tresca criterion 128

Figure 5.1 Schematic representation of loading/unloading criterion 137

Figure 5.2 Loading/unloading behavior of EPON 826/EPI-CURE 9551 139

Figure 5.3 Creep-recovery stress history and corresponding strain response 144

Figure 6.1 Creep modulus as a function of applied stresses 151

Figure 6.2 Comparison of experimental data with predicted creep-recovery curves by the differential constitutive model 153

Figure 6.3 Comparison of experimental data with predicted creep-recovery curves by the integral constitutive model 154

Figure 6.4 Comparison of experimental data with predicted strain curves at recovery by the differential constitutive model 155

Figure 6.5 Comparison of experimental data with predicted strain curves at recovery by the integral constitutive model 155

Figure 6.6 Prediction of shear creep deformation by the integral and differential constitutive models 156

Figure 6.7 Comparison of the predicted stress envelopes by both the integral and differential models with the experimental data ($\varepsilon_{oct} = 2.5\%$) 157

Figure 6.8 Comparison of the predicted stress envelopes by both the integral and differential models with the experimental data ($\varepsilon_{oct} = 1.5\%$, 2.0% and 2.5%) 158

Figure 6.9 Comparison of combined axial-shear proportional test with the predicted stress responses by the two models ($\dot{\varepsilon}_{oct} = 10^{-5}\ s^{-1}$) 159

Figure 6.10 Comparison of the experimental data for Path OBC with the predicted stress response by the two models ($\dot{\varepsilon}_{oct} = 10^{-5}\ s^{-1}$) 160

Figure 6.11 Comparison of the experimental data for Path OAC with the predicted stress response by the two models ($\dot{\varepsilon}_{oct} = 10^{-5}\ s^{-1}$) 161

Figure 6.12 Comparison between the experimental and predicted tensile stress-strain curves to failure at three different octahedral shear strain rates ($10^{-3}\ s^{-1}$, $10^{-4}\ s^{-1}$ and $10^{-5}\ s^{-1}$) 162

Figure 6.13 Comparison between the experimental and predicted compressive stress-strain curves to failure at three different octahedral shear strain rates ($10^{-3}\ s^{-1}$, $10^{-4}\ s^{-1}$ and $10^{-5}\ s^{-1}$) 163

Figure 6.14 Comparison between the experimental and predicted compressive stress-strain curves to failure at three different stress rates (5MPa/s, 0.5MPa/s and 0.05MPa/s) 164

Figure 6.15 Comparison between the experimental and predicted shear stress-strain curves to failure at three different octahedral shear strain rates ($10^{-3}\ s^{-1}$, $10^{-4}\ s^{-1}$ and $10^{-5}\ s^{-1}$) 165

Figure 6.16 Comparison between the experimental and predicted equibiaxial stress-strain curves to failure at an octahedral shear strain rates of$10^{-3}\ s^{-1}$ 166

Figure 6.17 Comparison between the experimental and predicted loading-unloading curve for the octahedral shear strain rate of $10^{-5}\ s^{-1}$ 168

Figure 6.18 Comparison between the experimental and predicted loading-unloading curves for proportional Path O-C-O (a) Axial, (b) Shear 169

Figure 6.19 Comparison between the experimental and predicted loading-unloading curves for non-proportional Path O-B-C-B-O (a) Axial, (b) Shear 171

Figure 6.20 Comparison between the experimental and predicted loading-unloading curves for non-proportional Path OAC (a) Axial, (b) Shear 172

Figure 7.1 Comparison of experimental data with predicted creep-recovery curves by the differential constitutive model 177

Figure 7.2 Comparison of experimental data with predicted creep-recovery curves by the integral constitutive model 177

Figure 7.3 Model predictions of equibiaxial creep deformation for two stress levels 178

Figure 7.4 Model predictions on shear creep for two axial stress cases:

Case 1: $\tau = 10\,\text{MPa}$, $\sigma_a = 14\,\text{MPa}$;

Case 2: $\tau = 10\,\text{MPa}$, $\sigma_a = -14\,\text{MPa}$ 179

Figure 7.5 Model predictions on shear creep with or without hydrostatic pressure p 180

Figure 7.6 Comparison of the predicted stress envelopes by both the differential and integral models with the experimental data (ε_{oct}=0.4%) 181

Figure 7.7 Comparison of the predicted stress envelopes by both the differential and integral models with the experimental data (ε_{oct}=0.8%) 182

Figure 7.8 Comparison between the experimental and predicted tensile stress-strain curve at the octahedral shear strain rate of $10^{-4}\ s^{-1}$ 183

Figure 7.9 Comparison between the experimental and predicted shear stress-strain curve at the octahedral shear strain rate of $10^{-4}\ s^{-1}$ 184

Figure 7.10 Comparison between the experimental and predicted equibiaxial stress-strain curves at two different octahedral shear strain rates ($10^{-4}\ s^{-1}$ and $10^{-5}\ s^{-1}$) 185

Figure 7.11 Experimental and predicted axial stress-strain curves for two different loading paths with an octahedral shear strain rate of $10^{-4} s^{-1}$ 186

Figure 7.12 Experimental and predicted shear stress-strain curves for two different loading paths with an octahedral shear strain rate of $10^{-4} s^{-1}$ 186

Figure 7.13 Experimental and predicted axial stress-strain curves for two different loading paths at two octahedral shear strain rates of $10^{-4} s^{-1}$ and $10^{-5} s^{-1}$ 187

Figure 7.14 Experimental and predicted shear stress-strain curves for two different loading paths at two octahedral shear strain rates of $10^{-4} s^{-1}$ and $10^{-5} s^{-1}$ 188

Figure 7.15 Axial strain creep deformations and predictions under two different non-proportional stress paths at $\tau = 15$ MPa, $\sigma_a = 21$ MPa 188

Figure 7.16 Shear strain creep deformations and predictions under two different non-proportional stress paths at $\tau = 15$ MPa, $\sigma_a = 21$ MPa 189

a_T — temperature shift factor

$[A]$ — matrix related to Poisson's ratio

B — bulk compliance

B_0 — instantaneous bulk compliance

c — solvent concentration

D — mean diameter of a tubular specimen

$D(t)$ — elastic or creep compliance at current time

D_0 — elastic compliance

e — true strain

E, E_0 — elastic modulus

$E(t)$ — elastic or stress relaxation modulus at time t

E_i (i=1, 2, …, n) — i^{th} creep modulus

E_m — spring constant in Maxwell model

E_v — spring constant in Kelvin model

F — axial load applied to a tubular specimen

g_0, g_1, g_2, g_2, a_σ, h_1, h_2, a_ε — nonlinear stress functions for Schapery model

I_1, I_2 — first and second invariants of a stress tensor

J — shear compliance

J_0 — instantaneous shear compliance

J_2 —second invariant of a deviatoric stress tensor

l, l_0 — actual length and initial length of a tested specimen

M — torque applied to a tubular specimen

p — hydrostatic pressure

P_i, P_e — internal and external pressures applied to a tubular specimen

R — ratio of uniaxial compressive-to-tensile stress

t — thickness of a tubular specimen

t_e — aging effect

T — current temperature

T_g — glass transition temperature

T_{ref} — reference temperature

α_i (i=1, 2, …, n) — constants in Xia-Ellyin model

δ — phase angle between a sinusoidal strain input and its stress response

ε, $\varepsilon(t)$ — strain, strain at time t

ε_0 — constant step strain

ε_a, ε_h — axial and hoop strains

$\dot{\varepsilon}_a$, $\dot{\varepsilon}_h$ — axial and hoop strain rates

ε_c, $\varepsilon_c(t)$ — creep strain, creep strain at time t

ε_e, $\dot{\varepsilon}_e$ — elastic strain and elastic strain rate

ε_{ci}, $\dot{\varepsilon}_{ci}$ — creep strain and creep strain rate for i^{th} Kelvin element

ε_{oct}, $\dot{\varepsilon}_{oct}$ — octahedral shear strain and octahedral shear strain rate

$\varepsilon_r(t)$ — strain at recovery

$\dot{\varepsilon}_t$ — total strain rate

γ , $\dot{\gamma}$ — shear strain and shear strain rate

η_m — viscosity coefficient in Maxwell model

η_v — viscosity coefficient in Kelvin model

λ — non-dimensional recovery time

θ — mechanically induced dilatation

ρ , ρ' — strain-reduced times

σ , $\sigma(t)$ — stress, stress at time t

$\dot{\sigma}$ — stress rate

σ_a , σ_h — axial and hoop stresses inside a tubular wall

σ_{eq} — equivalent stress

σ_{ij} — stress component

σ_{kk} — hydrostatic stress

σ_m — one third of σ_{kk}

σ_1, σ_2 , σ_3 — three principal stresses of a stress tensor

σ^* — uniaxial tensile yield stress

τ — shear stress inside a tubular wall

τ_i (i=1, 2, …, n) — i^{th} stress relaxation time

τ_m — characteristic time for stress relaxation

τ_{oct} — octahedral shear stress

τ_v — characteristic time for strain creep

ξ, ξ' — temperature-reduced times

υ — Poisson's ratio

ψ, ψ' — stress-reduced times

ΔB — transient shear compliance

$\Delta D(t)$ — creep compliance at current time

$\Delta E(t)$ — stress relaxation modulus at current time

ΔJ — transient bulk compliance

$\Delta\varepsilon_1$ — creep component of strain at time t_1

Chapter 1

Introduction

Fiber-reinforced polymeric composites offer important structural advantages over conventional metals in many applications as a result of their high specific strength and stiffness, low density, tailorability of their properties and corrosion resistance, among others. Consequently, the use of polymeric composites has grown enormously, from daily life products such as frames for mountain bicycles to primary structures such as turbine engines and high speed aircraft skins.

Despite the aforementioned advantages and the progress already made in the application of composites, many issues remain to be solved. Among them creep and damage growth are two important ones which usually hinder wider applications of composites, especially in critical load-bearing structures. Creep and damage growth induce dimensional change, loss of stiffness and strength and leakage in the case of pressure vessels or pipelines. These changes and leakage will then limit the useful life or even cause accidents. Therefore, an improved fundamental understanding of the influence of creep and damage over service lifetimes in realistic environments is needed for composites to gain wider acceptance in commercial and military applications. The understanding, along with the capability to model the creep and damage behavior, is also essential for composites to achieve a significantly increased level of structural efficiency and reliability.

In polymeric composites, the fiber phase is basically linearly elastic and shows little time-dependent behavior (Fig.1.1). It also has much higher strength than matrix phase. Thus, the creep and damage behavior originates primarily from the matrix phase, including the polymer-fiber inter-phase zone. It is evident that in order to understand and to model the creep and damage behavior of composites, one must understand and be able to model the deformation and failure behavior of polymer matrices.

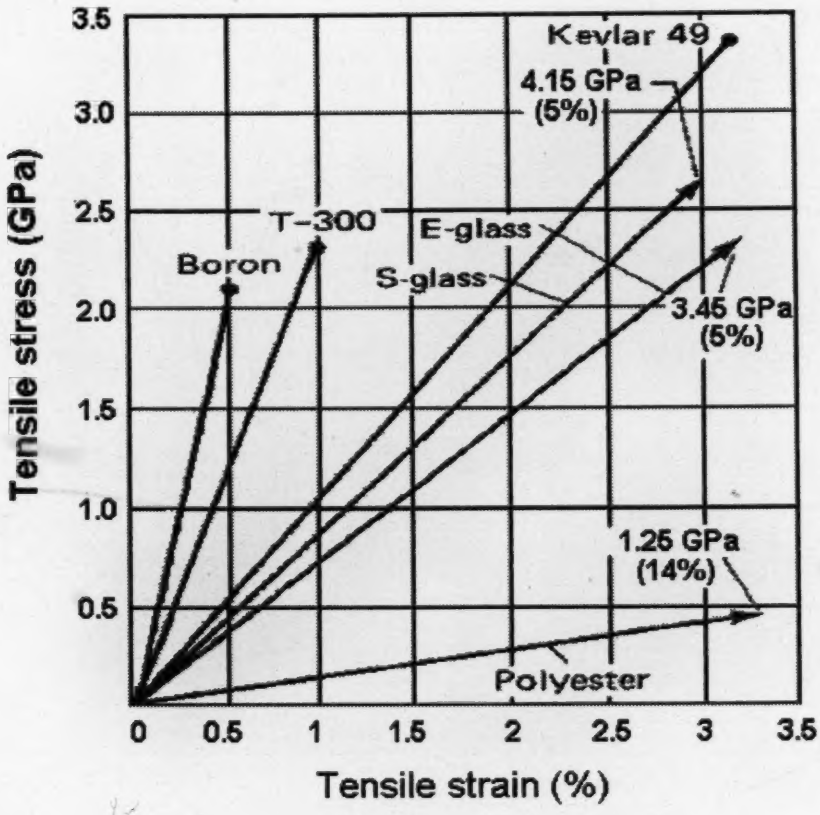

Fig.1.1 Linear stress-strain behavior for typical fibers

(adopted from Engineering Materials Handbook, Volume 1: Composites)

Polymers as matrices in composites have three main roles. First, they are used as adhesives to bind the adjacent fibers together. Second, they provide a barrier against an adverse

environment, and protect fibers from mechanical abrasion. Third, and the most important function is to carry transverse and shear loading, share loads with fibers and facilitate load transfer between fibers. The stress states in the matrix are generally multiaxial. Even in a unidirectional laminate under an off-axis uniaxial loading, the stress states in the matrix may still be multiaxial and non-uniform due to the interaction between the fiber and matrix. Therefore, three-dimensional models are required for accurate predictions of the deformation behavior of polymers. Linear three-dimensional models may be adequate for preliminary design purposes. However, in order to achieve structurally efficient designs that meet long-term performance requirements, nonlinear effects in constitutive models frequently must be taken into account. The choice or development of an appropriate model to predict the deformation behavior usually necessitates a general understanding of the properties of the material involved, and these properties are mostly found through experimental investigations. Thus, the multiaxial deformation and failure behavior of polymeric matrices must be explored experimentally, along with the multiaxial nonlinear viscoelastic constitutive models.

Due to the important role played by polymers in polymeric structural applications, extensive work on the mechanical behavior and models has been done, and this will be reviewed in the following sections. Because the mechanical behavior of polymers is closely linked to their molecular structures, some basic concepts on the structures of polymers are introduced in the first section. In the second section, the work done on the deformation and failure behavior of polymers is reviewed. The effort made to model the observed mechanical behavior of polymers is summarized in the third section. During the

review, the issues still to be dealt with are pointed out, which serve as the direction of this research. Finally the scope and the objective of this research are outlined.

1.1 Polymers

Polymers consist of long molecular chains of covalently bonded atoms, and are made by a process called polymerisation, whereby monomer molecules react together chemically to form three kinds of polymer chains: linear, branched, and cross-linked (Fig.1.2). Based on the extent of cross-linkage between molecular chains, polymers can be classified into three categories: thermosets, thermoplastics, and rubbers. Thermosetting polymers have a highly cross-linked structure. Thermoplastics consist of linear and branched chains. Rubbers are tightly kinked cross-linked structures and are capable of large elastic strains.

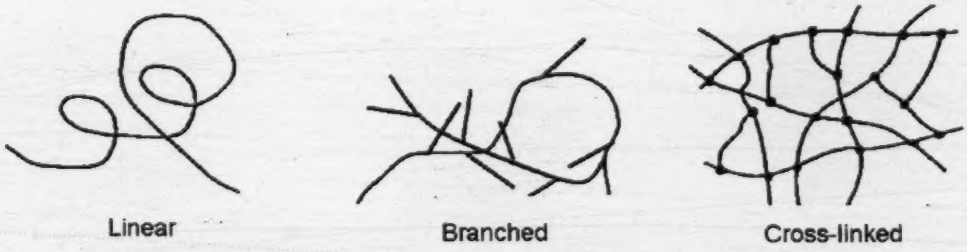

Fig.1.2 Three types of polymer chains (adopted from Anderson, 1991)

The presence of branching and cross-linking in polymers has a significant effect on properties. It is the basis of the difference between the three categories of polymers. Thermosets, normally formed by mixing a basic resin with a hardener, have quite strong atomic bonds. Once these atomic bonds are broken, they cannot be reformed, so thermosets are insoluble and infusible after cure. Examples of thermosetting polymers include epoxy, polyester, and vinylester. For thermoplastics, molecular bonding occurs primarily as weak

secondary bonding (Van der Waal forces) between adjacent molecules (Fig.1.3). These bonds slip under relatively low stress (compared with thermosetting polymers) and weaken considerably with temperature increase. Examples of thermoplastics include polyethylene, nylon, polypropylene, polystyrene, polycarbonate, etc. Thermoplastic polymers can be repeatedly softened and formed by increasing the temperature and hardened by decreasing the temperature.

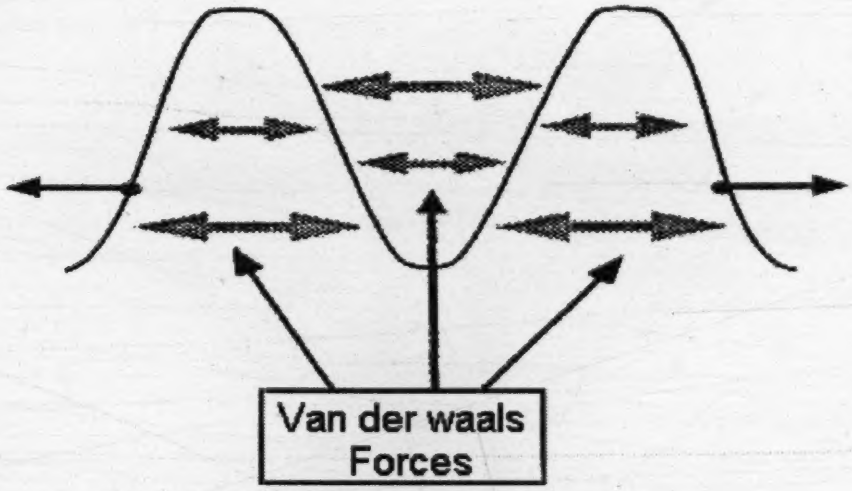

Fig.1.3 The Van der Waals force between chain segments

(adopted from Anderson, 1991)

The arrangement of molecular chains of polymers is another factor that influences the mechanical behavior. There are three types of polymers: amorphous, semi-crystalline, and crystalline polymers. As shown in Fig.1.4, the crystalline polymers are tightly packed and have a regular pattern of molecular chains, while the molecular chains for amorphous polymers are randomly entangled. Semi-crystalline polymers contain both crystalline and amorphous regions and can be obtained when cooled down slowly from the molten state.

Epoxy and polystyrene are examples of amorphous polymers. Crystalline polymers include high density polyethylene, polypropylene, and nylon.

Crystalline polymers often show anisotropic mechanical behavior due to the oriented molecular chains. Amorphous polymers have isotropic material properties. Owing to the complex coupling between the crystalline phase and the amorphous phase, the mechanical behavior of semi-crystalline polymers is more complicated.

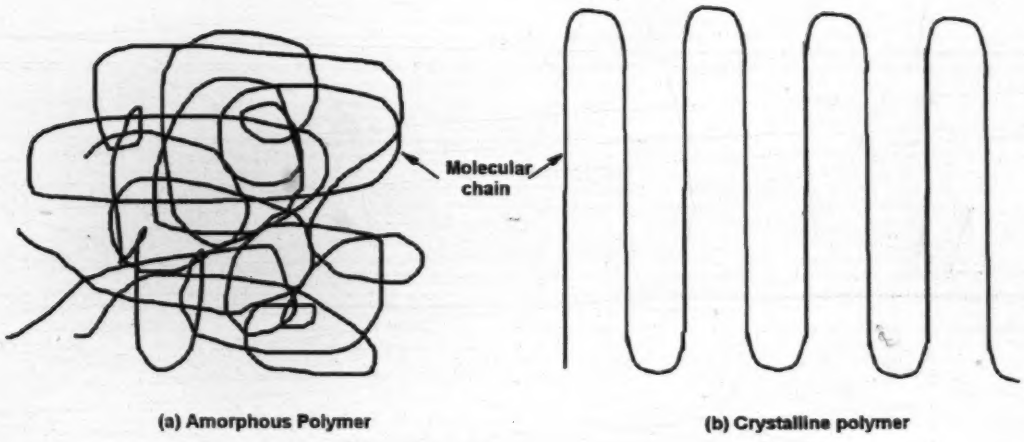

Fig.1.4 Amorphous and crystalline polymers

1.2 Phenomenological Behavior

The mechanical behavior of a material is closely related to its microstructures. Because of the complex molecular structures of polymers, it is expected that the mechanical behavior of polymers will be very complicated. However, if the initial focus is confined to small deformations, i.e., linear viscoelastic regime, it is found that the description of the mechanical behavior in this range is well established. From an experimental point of view, if each loading step makes an independent contribution to the final deformation, and the

final deformation can be obtained by the simple addition of each contribution, the polymer is said to be of linear viscoelastic. One of the mathematical statements of linear viscoelastic behavior is Boltzmann Superposition Principle (Ward, 1983), which will be further explored later on in Section 1.3.1.

1.2.1 Linear viscoelastic behavior

In linear viscoelasticity, effects are simply additive, as in classical elasticity, the difference being that in linear viscoelasticity it matters at which instant an effect is created, i.e., time is also a factor in the relationship. Generally there are three main types of experiments to characterize the linear viscoelastic behavior of polymers, i.e., creep (including subsequent recovery), stress relaxation, and dynamic mechanical experiments (Findley et al., 1976, Ward, 1983).

a. Creep

Figure 1.5 shows the strain response of a typical polymer under a fixed stress σ_0. It exhibits elastic action upon loading (if loading is rapid enough), then a slow and continuous increase of strain at a decreasing rate is observed. When the stress is removed a continuously decreasing strain follows an initial elastic recovery. As polymer shows both the solid elastic and fluid viscous behaviors, it is called viscoelastic material. Since time is a very important factor in its behavior, it is also called time-dependent material. If, following stress removal, a measurable portion of the deformation does not vanish after a long period of time, and this residual deformation is affected by the time under prior loading, then this deformation is commonly called viscoplastic. Viscoelastic materials may or may not exhibit viscoplasticity.

The above observed phenomenon is the direct result of the molecular structures of polymers. The deformation of a polymer consists of the deformation of molecular chains themselves and the cooperative motion among molecular chains. If a loading is applied very fast, the molecular chains have no time to start the cooperative motion process, only the molecular chains themselves are deformed, elastic response is then observed. However, when the loading is held, the molecular chains have time to move against each other and the material becomes compliant, thus, creeps. If the load is removed, the material attempts to return to its original shape, but molecular entanglements prevent instantaneous elastic recovery. For thermosets, the recovery process is complete because of its cross-link structures. Thermoplastics, however, do show a finite permanent deformation at temperatures above their glass transition temperatures (T_g, which is defined as the temperature at which long range, cooperative motions of individual chains start to occur) or at high stress level.

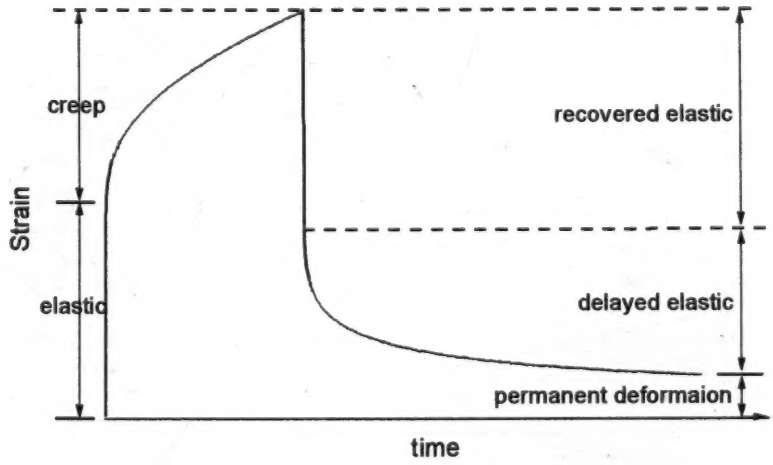

Fig. 1.5 Creep deformation of a viscoelastic material

b. Stress relaxation

The counterpart of creep is stress relaxation, where the strain is kept constant and the corresponding stress decreases continuously at a decreasing rate as shown in Fig.1.6. The stress relaxation is associated with the viscous, time-dependent behavior of the material as the long chains arrange themselves to accommodate the imposed deformation.

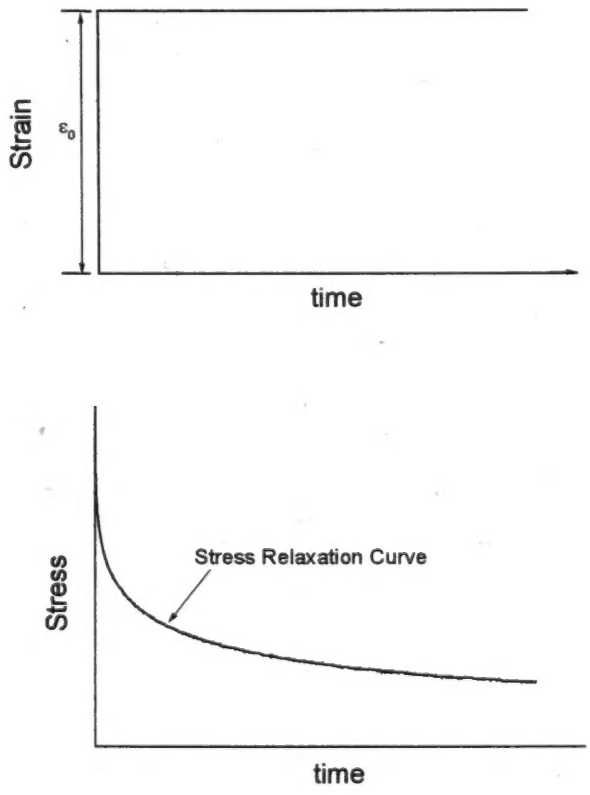

Fig. 1.6 Stress relaxation at constant strain

c. Dynamic mechanical analysis

To obtain a satisfactory understanding of the viscoelastic behavior, data are required over a wide range of time. Creep and relaxation experiments may provide the mechanical

behavior of polymers from seconds to years. In certain cases such as impact, the response of polymers to a loading for times shorter than seconds may be of practical importance (Ward, 1983). Then, dynamic mechanical analysis is more suitable. Figure 1.7 illustrates the dynamic mechanical behavior of a viscoelastic material (Fried, 1995). In dynamic testing, the stress is measured as a function of strain that is some periodic function of time, usually a sine wave. Different from fatigue tests, dynamic mechanical properties are measured at low strains so that deformation is not permanent.

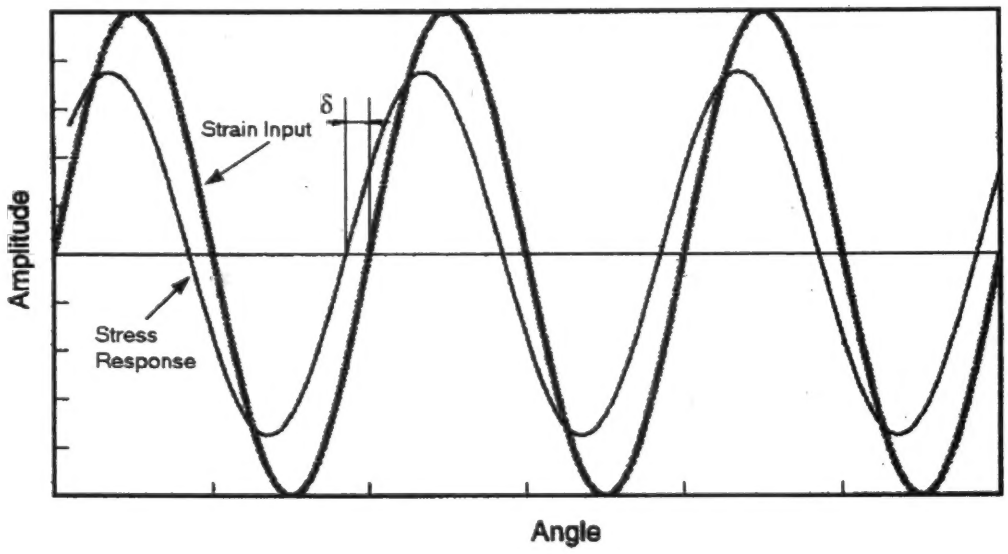

Fig. 1.7 Representation of an arbitrary strain function and resulting stress response of a viscoelastic material (modified from Fried, 1995)

Unlike elastic materials, where strain input and stress response coincide and the two curves have the same phase, a viscoelastic material displays a phase angle, δ, between the strain input and the stress response. From the two curves, the mechanical properties for the given frequency can be analyzed. For different frequencies, different mechanical properties can

be obtained and the frequency dependence of the mechanical properties can, therefore, be drawn, which can then be converted to time dependence (Ward, 1983, Fried, 1995).

As is the case for other forms of mechanical deformation, work is expended during dynamic mechanical testing. The amount of work, or power, consumed depends upon the viscoelastic properties of the polymer. When a viscoelastic material is subject to multiple stress – strain cycles, a significant amount of work is performed on the material. Much of this work is converted to heat, and the temperature in the material rises, and, thus, changes mechanical properties of the material. Therefore, dynamic mechanical tests can also be used to determine the glass transition temperature, T_g, of polymers (Christensen, 1982).

Another implication is that fatigue crack growth data from small laboratory coupons may not be applicable to structural components because heat transfer properties depend on the size and geometry of the sample.

1.2.2 Nonlinear viscoelastic behavior

In many practical applications of polymeric structures, although polymers can ultimately recover to its original state after unloading, the viscoelastic behavior does not satisfy the tests of linearity required by the Boltzmann Superposition Principle. For most polymers, it is quite usual to observe linear viscoelastic behavior at short times or at low stress levels, but the behavior becomes markedly nonlinear for long times or at high stress levels. Some polymers even do not show linear behavior, nonlinearity begins as early as the stress is applied (see Fotheringham and Charry, 1978, Lai and Bakker, 1995).

Owing to the vast differences in polymeric materials, and hence, the nature of the nonlinearity, a single test approach has not been developed to adequately describe the behavior of all polymeric materials. As such, considerably different experimental investigations have been performed in an attempt to capture the natures of wide-ranging nonlinear responses.

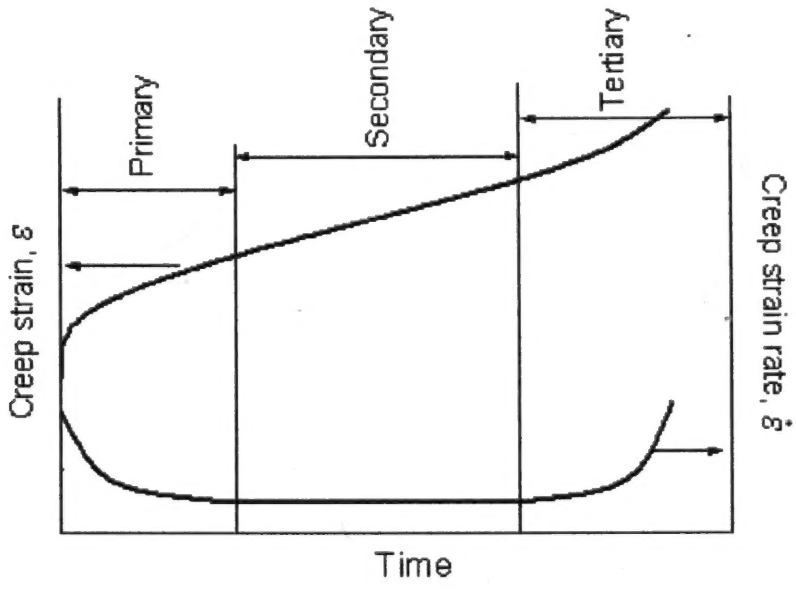

Fig. 1.8 Three stages of creep deformation

Nonlinear creep behavior of polymers is extensively studied and well documented (e.g., see a review by Turner, 1973a). Figure 1.8 illustrates a typical creep curve for polymers under uniaxial tensile stress. It may be generally described in terms of three different stages. The first stage in which creep occurs at a decreasing rate is called primary creep; the second, called the secondary stage, proceeds at a nearly constant rate, and the third or tertiary stage occurs at an increasing rate and terminates in fracture. The strain at the third stage may be so large that the specimen suffers irreversible changes. There may be the

appearance of 'stress whitening', the formation and growth of cracks or crazes, the development of deformation bands, necking or complete rupture. These phenomena usually mark the boundary between viscoelastic and rupture behavior (Bowden, 1973).

One of the tests that was widely used to study the nonlinear viscoelastic behavior of polymers was suggested by Turner (1966, 1973b). It consists of a series of creep experiments applied at different stress levels. The corresponding responses are shown in Fig.1.9. The section normal to the stress axis is the creep deformation under a given stress level and the section normal to the log time axis is the isochronous stress-strain curve which is the relationship between stress and strain for a fixed time of measurement.

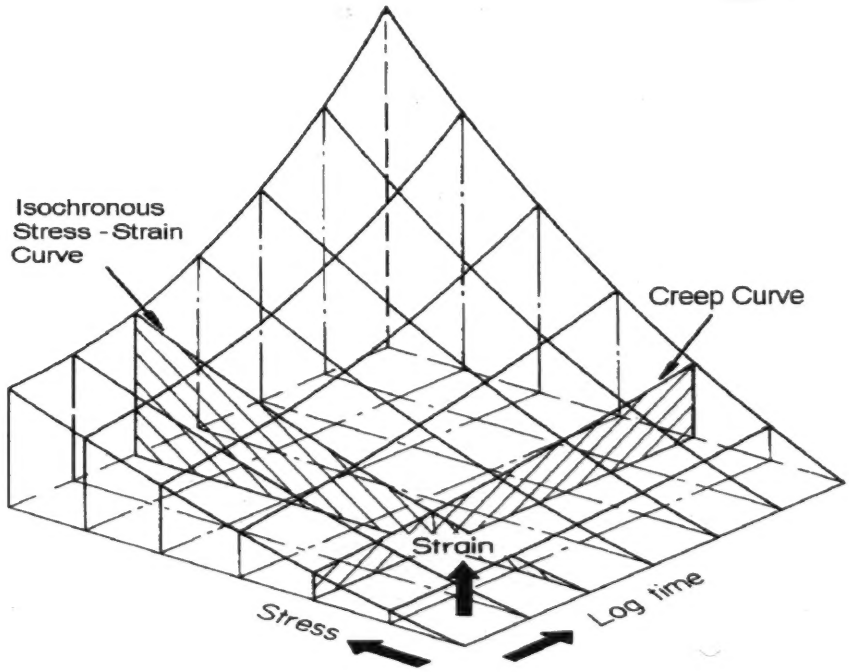

Fig. 1.9 Stress-strain-time relationship obtained from series of single step loading (adopted from Turner, 1966)

From the isochronous stress-strain curves, it can be seen that linear ranges only exist at low stress levels or at short times. At high stress levels or at long times, pronounced nonlinear behavior is noticed. The creep curves at high stresses are much steeper than ones at low stresses, i.e., creep can be accelerated by increasing stress.

Another property of nonlinear viscoelastic polymers is that the instantaneous recovery is larger than the instantaneous creep from a single step loading followed by the removal of load, as shown in Fig.1.10 (Turner, 1973a, Mindel and Brown, 1973, Ward 1983). If materials were linear viscoelastic, such creep-recovery experiments would not be needed because the recovery characteristics could be predicted from the creep compliance function by means of the Boltzmann Superposition Principle. But, in the absence of an equivalent rule for nonlinear materials, direct measurements are necessary. Because of this, recovery data are an essential part of the evaluation of nonlinear viscoelastic materials. The difference between the creep and recovery strain responses is attributed to strain-softening (Turner, 1973a) and may be explained by Struik's aging theory (Struik, 1978), although how applied stress affects the physical aging, according to Schapery (2000), is still a controversial issue.

Although step tensile loading is usually used to obtain the creep behavior of polymers, it can not reflect the compressive creep behavior for some polymers. It was found that tensile and compressive creeps were not necessarily identical (Marin et al. 1951) and in general the resistance to creep in uniaxial compression is superior to the resistance to creep in tension (O'Connor and Findley, 1962, Mindel and Brown, 1973, Kontou and Farasoglou,

1998). This may be attributed to hydrostatic stress effect and was confirmed by shear tests under superposed hydrostatic pressure (Pae, 1975, Silano, 1982).

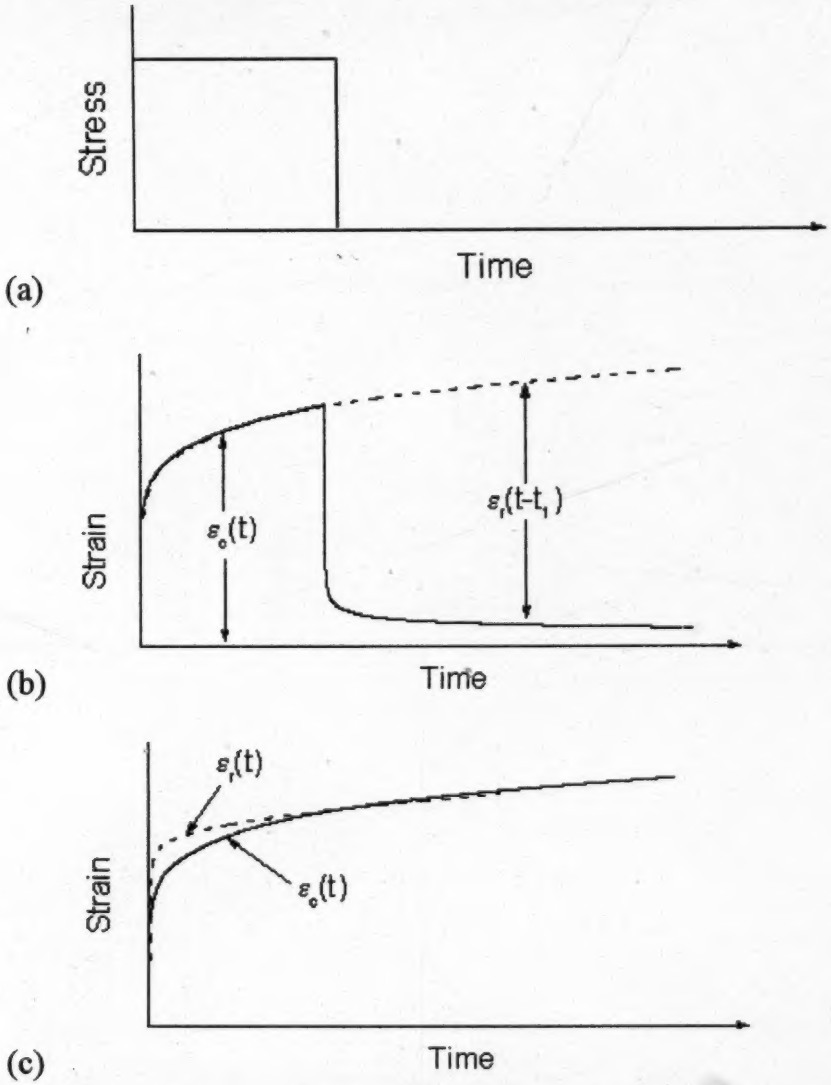

Fig.1.10 (a) Loading program, (b) deformation and (c) direct comparison of creep $\varepsilon_c(t)$ and recovery $\varepsilon_r(t)$ for a non-linear viscoelastic solid

The volume (especially free volume, which is defined as the difference between the apparent volume of the material and that actually occupied by the atomic structure) change

during loading is another important nonlinear viscoelastic parameter of polymers because it is the basis of some microscopically based constitutive models. It was observed that the creep in some polymers occurred without change in volume whereas in other polymers creep was accompanied by an increase in volume (Benham and McCammond, 1971). One possible explanation is that the increase in volume is merely indicative of the formation of microvoids, or zones of reduced density, because the tested samples were seen to stress whiten at high stress. The volume decrease observed in some polymers is attributed to the changes in molecular configuration and packing (Benham and McCammond, 1971, Read and Dean, 1984). Free volume can also explain the difference between tension and compression creep as the decrease in free volume in compression reduces the mobility of the chain segment with resulting lower deformation (Benham and McCammond, 1971). One challenge to this free volume theory is to accommodate the nonlinear behavior under pure shear (Popelar and Liechti, 1997).

Another way to study the viscoelastic behavior of polymeric materials is to load the specimens at different constant stress or strain rates. This is the kind of tests widely used in metals or alloys to investigate their rate effect at high temperature (Ellyin, 1997). It is observed that an increase in loading stress/strain rate causes an increase in stress level (Bordonaro and Krempl 1992, Zhang and Moore, 1997). The stress-strain curves at constant stress/strain rates are widely used in the characterization of model parameters and the comparison and verifications of various constitutive models (Smart and Williams, 1972, Chen and Zhou, 1998, Hasan and Boyce, 1995).

1.2.3 Multiaxial behavior

Most of the above cited works was generally focused on simple stress states such as uniaxial tension, uniaxial compression, plane strain compression, and simple shear. However, the stress state in engineering applications is generally of multiaxial nature. Also, multiaxial loading is necessary for the study on the effect of rotation of principal stress or strain axes and for the verification of multiaxial constitutive equations. Despite the importance of the need to understand multiaxial behavior of polymers, only a few experimental investigations have been reported in the literature.

A widely reported topic was the investigation of interaction between normal and shear creep deformations under combined axial/torsional stresses. It was found that the normal stress influences the shear creep response for many polymers and vice versa (Buckley and Green, 1976, McKenna and Zapas , 1979, Lu and Knauss, 1999). Buckley (1987) further showed that the bulk compliance of polypropylene was only time dependent, however, the shear compliance depends on both hydrostatic stress and deviatoric components of the stress history for the material. Therefore, the nonlinearity comes from the shear compliance.

The combined tension-torsion creep tests by Ewing et al. (1972, 1973) and transient tests with constant equivalent strain rates by Kitagawa and Takagi (1990) for polyethylene seem to show that the equivalent stress and strain equations can be used to describe the responses of the material to a variety of complex loading conditions. This is rather contradictory to test results by Mears et al. (1969), who showed that the mechanical behavior of polyethylene is hydrostatic pressure dependent.

The effect of hydrostatic component of stress on nonlinear behavior of polymers was studied in different ways. One of them is shear test with equal value but different sign of axial stresses superimposed on it (Lu and Knauss, 1999). The difference in shear strain responses was attributed to the hydrostatic stress effect. Pure shear with superposed hydrostatic pressure was used by many investigators (see e.g., Silano, 1982) for this study, although mainly for yield behavior. The response before yield did show a hydrostatic stress effect.

The mechanical behavior under non-proportional loading is another topic of significant interest. It is the kind of tests popular in elasto-plastic materials for a constitutive model verification. Tests on nylon 66 by Krempl and Bordonaro (1998) indicated that the mechanical behavior of this polymer was influenced by non-proportional loading paths, although these tests were very preliminary and further work is needed for more complex loading paths.

Although much effort has been made to investigate the mechanical behavior of polymers, the data available in the nonlinear range is still limited, especially for multiaxial stress states. Usually different behavior is obtained by different polymers and it is very rare that one specific polymer has been tested to investigate its behavior under different loading conditions. This points out to the difficulty that one model calibrated for one loading condition can only be compared with very limited other loading conditions, and therefore, there is not enough data to fully verify its predictive capability. The reason may be attributed to the complex structures of solid polymers as discussed in the first section of

this chapter. The complex structures and their strong dependence on environments and manufacturing process make it very difficult to obtain reliable and repeatable test data.

1.3 Constitutive Modeling

It was indicated in the previous section that the mechanical behavior of polymers in their applications is usually very complicated. The polymers, however, do share some deformation characteristics, among them, time effect and hydrostatic stress dependency. These deformation characteristics have design implications. For example, due to time-dependent behavior, dimensional changes in polymeric structures occur during their service life, and this has to be considered during the design phase of such structures. Although experimental investigations provide very useful information for the design of polymeric structures, they are generally expensive and time consuming to perform, especially for long-term behavior testing.

With the advent of high-speed computation hardware and software, numerical methods are finding more and more applications in evaluating the behavior of polymeric structures. For example, finite element methods have been widely used for the stress analysis and strength evaluation of polymeric structures (Chen et al, 2001, Yi and Hilton, 1997, among others). However, the success of such applications is largely dependent on the accurate description of the deformation behavior of constituents involved, especially the properties of matrices since fibers can generally be considered to remain linear elastic within their application range. Therefore, a proper constitutive modeling of deformation behavior of polymer matrices is a prerequisite in attempting to predict the overall stress-strain responses of the

fiber-reinforced composites, as well as an understanding of their long-term performance and failure mechanisms.

Owing to the difference in the molecular structures of polymers and the different manifestations of viscoelastic behavior, Currently there are a number of viscoelastic constitutive laws for polymers. Some may be suitable for describing a specific response of polymers; others are said to be more general. Some of those models are summarized as follows.

1.3.1 Linear viscoelastic models

Linear viscoelastic constitutive models are well established and widely used in theoretical and engineering analyses. They can generally be classified into two categories according to the mathematical operations used, i.e., differential and integral forms.

a. Differential formulation

This is the earliest mathematical representation of linear viscoelastic behavior of polymers. It comes from the intuition that viscoelastic materials may be represented by the combination of Hookean law and Newton's law because they exhibit the behavior of both elastic solid and viscous fluid. Maxwell model and Kelvin (Voigt) models are two of the earliest. In Maxwell model, a spring element, which represents the elastic solid, and a dashpot, which represents the viscous fluid, are connected in series (Fig 1.11(a)). In Kelvin (Voigt) model, the two elements are connected in parallel (Fig. 1.11(b)).

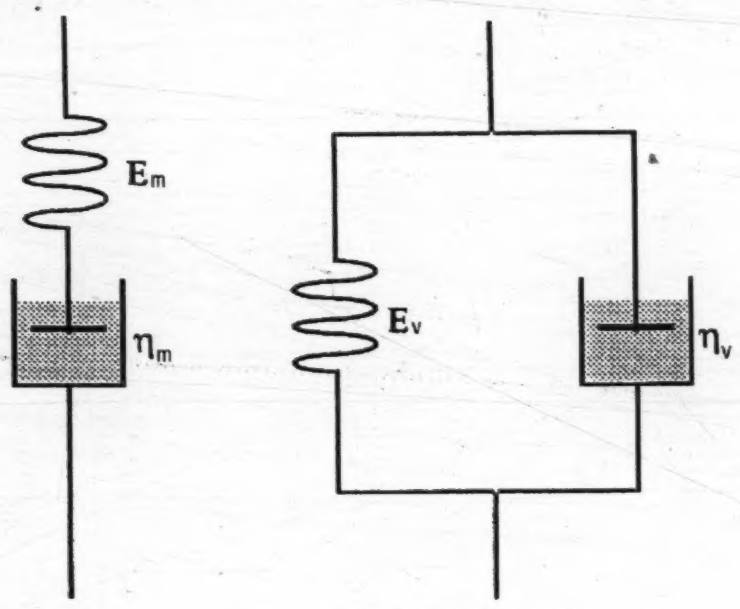

(a) (b)

Fig. 1.11 Mechanical models: (a) Maxwell model; (b) Kelvin model

It is expected that neither the Maxwell nor Kelvin (Voigt) model accurately represents the behavior of most viscoelastic materials. For one thing, the models described above have only one relaxation time ($\tau_m = \eta_m / E_m$, a characteristic time to represent stress relaxation) or retardation time ($\tau_v = \eta_v / E_v$, a characteristic time to represent strain creep), whereas real materials often behave as though they have several relaxation times because of their complex structure. To deal with this situation, more elements have to be included and this will inevitably bring in the difficulty of determining the model constants and the implementation of complex numerical procedures.

The general relationship between stress, strain and time for a linear viscoelastic material with finite number of Maxwell or Kelvin elements can be represented by

$$\sum_{i=1}^{n} a_i \frac{d^i \sigma}{dt^i} = \sum_{j=1}^{m} b_j \frac{d^j \varepsilon}{dt^j} \tag{1.1}$$

where a_i and b_j are constants.

a. Integral formulation

For linear viscoelastic materials, the Boltzmann superposition principle applies (Ward, 1983). It means that the final response can be obtained by the simple addition of contributions from each single loading step. For an arbitrary loading history $\sigma(t)$ or $\varepsilon(t)$, its corresponding response, $\varepsilon(t)$ or $\sigma(t)$, therefore, is

$$\begin{cases} \varepsilon(t) = \int_{-\infty}^{t} D(t-\tau) \dfrac{\partial \sigma(\tau)}{\partial \tau} d\tau \\ \sigma(t) = \int_{-\infty}^{t} E(t-\tau) \dfrac{\partial \varepsilon(\tau)}{\partial \tau} d\tau \end{cases} \tag{1.2}$$

where D(t) and E(t) are the creep compliance and the stress relaxation modulus, respectively. The integral starts from -∞ because the current response is related to the entire loading history for a viscoelastic material.

In general, the differential operator method is intuitive and has simple mathematical processes, however, it usually needs large number of Maxwell or Kelvin (Voigt) elements to accurately represent the actual viscoelastic behavior of polymers and, thus, causes the difficulty of model parameter calibration. On the other hand, the integral representation is able to describe the time dependence in a more general term, but it sometimes leads to rather involved mathematical operations during a stress analysis. The advantage of using integral representation over differential operator forms is believed to be in the flexibility of

representation of the experimentally measured viscoelastic material properties. The integral representation also can be extended readily to describe the behavior of aging material; and it is easy to incorporate temperature effects (Findley et al., 1976).

Both the differential operator method, (1.1), and integral representation, (1.2), can be easily generalized to a multiaxial state of stress (Zienkiewicz et al., 1968, Findley et al., 1976). By performing a proper set of experiments the material constants and the kernel functions for a given material can be determined and used to predict behavior under other stress histories.

1.3.2. Nonlinear viscoelastic models

While the well-established linear viscoelasticity is capable of predicting the relatively small strain response of polymeric materials, this linear range only accounts for a small fraction of the entire range of deformation. Nonlinear behavior can occur even when the deformations are small. In order to describe the behavior of polymers used in structural applications where the response likely extends well into the nonlinear regime, viscoelastic models capable of describing nonlinear nature of the material are required.

In the past forty years, there has been considerable effort to develop a general constitutive equation for nonlinear viscoelastic materials, which has simple and universal forms comparable to those that exist in the case of linear theory. Unfortunately, there does not exist such a representation of nonlinear viscoelasticity which gives an adequate description of broad classes of the polymer material behavior. Currently there are only limited and special forms of constitutive relations that have some well-delineated applicability to

particular materials or classes of materials in particular situations. These are briefly described below.

a. Scahpery model

The Schapery model is a single integral model, which was derived from thermodynamics of an irreversible process (Fung, 1965). With certain assumptions this theory was subsequently extended to nonlinear materials (Schapery, 1969a). The constitutive equation can be expressed as

$$\varepsilon(t) = D_0 g_0 \sigma(t) + g_1 \int_0^t \Delta D[\psi(t) - \psi(\tau)] \frac{d(g_2 \sigma)}{d\tau} d\tau \tag{1.3}$$

for the strain in terms of the stress history, and

$$\sigma(t) = E_0 h_0 \varepsilon(t) + h_1 \int_0^t \Delta E[\rho(t) - \rho(\tau)] \frac{d(h_2 \varepsilon)}{d\tau} d\tau \tag{1.4}$$

for the stress in terms of the strain history. The stress-reduced time ψ and the strain-reduced time ρ are defined as follows

$$\psi(t) = \int_0^t \frac{ds}{a_\sigma}, \qquad a_\sigma > 0 \tag{1.5}$$

$$\rho(t) = \int_0^t \frac{ds}{a_\varepsilon}, \qquad a_\varepsilon > 0 \tag{1.6}$$

D_0 and ΔD are instantaneous and transient components of linear creep compliance, E_0 and ΔE are instantaneous and transient components of linear relaxation modulus, respectively. The material properties g_0, g_1, g_2 and a_σ are functions of the stress and h_0, h_1, h_2 and a_ε are dependent on the strain.

It can be seen that if nonlinear functions $g_0 = g_1 = g_2 = a_\sigma = 1$ in Eq. (1.3) and $h_0 = h_1 = h_2 = h_\varepsilon = 1$ in Eq. (1.4), the Schapery model will reduce to the linear integral model for viscoelasticity, Eq. (1.2). Other models such as the modified superposition principle and the BKZ theory can be derived from the Schapery representation by similar simplifications (Schapery, 1969b).

The Schapery theory incorporates the time-temperature correspondence through the shift factor in the reduced time, a logical extension of time-temperature superposition in linear viscoelastic theory (Ferry, 1980). Other effects such as moisture and physical ageing have been recognised as changing the relaxation behavior of polymers in a manner similar to temperature and can also be dealt with by the Schapery representation (Roy and Reddy, 1988, Zhang et al., 1997).

Successful applications of the Schapery representation to some polymers as well as to fibre-reinforced composite materials have been reported in the literature (Schapery, 1969b, Peretz and Weitsman, 1982, Zhang et al., 1997). It is demonstrated by Schapery (Lou and Schapery, 1971) that the data reduction procedure for determining the material properties in the Schapery representation is fairly straight forward. The material properties in Eq.(1.3) can be evaluated using creep and recovery data, while two step relaxation data are needed to evaluate the material properties in Eq. (1.4). Standard procedure to characterize the material properties based on least square method was developed (Peretz and Weitsman, 1982, Augl and Land, 1985)

b. Free Volume Approach

This approach came from the experimental observation that the effect of temperature change on the mechanical behavior of viscoelastic materials can be simulated by changing time scale of Eq. (1.2) through time-temperature superposition principle (Findley et al., 1976), i.e.,

$$\begin{cases} \varepsilon(t) = \int_{-\infty}^{t} D(\xi - \xi') \dfrac{\partial \sigma(\tau)}{\partial \tau} d\tau \\ \sigma(t) = \int_{-\infty}^{t} E(\xi - \xi') \dfrac{\partial \varepsilon(\tau)}{\partial \tau} d\tau \end{cases} \tag{1.7}$$

where real times t and τ in Eq. (1.2) are replaced by the temperature-induced reduced times ξ and ξ', which are related to the original real times t and τ by (Morland and Lee, 1960)

$$\xi(t) = \int_0^t \frac{ds}{a_T} \quad \text{and} \quad \xi'(\tau) = \int_0^\tau \frac{ds}{a_T} \tag{1.8}$$

where a_T is a temperature shift factor, which is defined as

$$\log a_T = \frac{C_1 (T - T_{ref})}{C_2 + (T - T_{ref})} \tag{1.9}$$

Here, C_1 and C_2 are constants, and T_{ref} is a reference temperature peculiar to a particular polymer. It was found that Eq. (1.9) holds extremely well over the temperature range $T = T_{ref} \pm 50^\circ C$ for all amorphous polymers (Ward, 1983). This equation is the well known W.L.F. equation (Ferry, 1980)

Later studies found that the empirical W.L.F. equation had a more fundamental theoretical interpretation, which brought in the concept of free volume (Ward. 1983). It is believed that not all spaces inside polymers are occupied by molecules due to imperfect packing and defects such as molecular chain ends. There are still holes or voids which remain unoccupied. The unoccupied part of spaces is called free volume, which allows molecular motion to take place more easily (Lai, 1995). The temperature change influences the free volume and, therefore, changes the material time scale according to Eqs. (1.8) and (1.9).

This concept was extended because it is found that solvent concentration (Knauss and Kenner, 1980), mechanical pressure (Fillers and Tschoegl, 1977) and physical aging (Struik, 1978) also change the free volume and, therefore, influence the time scale of viscoelastic materials. If the fractional free volume due to any one of the four variables (temperature T, solvent concentration c, mechanically induced dilatation θ, and aging effect t_e) is additive, the final shift factor, $a(T,c,\theta,g)$, then becomes

$$\log a(T,c,\theta,g)=\frac{\alpha(T-T_{ref})+\gamma\cdot c+\delta\cdot\theta+\lambda\cdot t_e}{C_0+\alpha(T-T_{ref})+\gamma\cdot c+\delta\cdot\theta+\lambda\cdot t_e} \tag{1.10}$$

where α, γ, δ, and λ are, in general, functions of T, c, θ, and t_e. C_0 is a constant.

One advantage of free volume theory is that it provides some physical insight into the origins of the nonlinear viscoelasticity (Schapery, 2000). In this model, nonlinear behavior comes from only the materials time scale through a free volume-dependent reduced time (Losi and Knauss, 1992). The underlying assumption is that the free volume controls molecular mobility, directly affecting the inherent time scale of the material. Another

advantage is that it can unite the effect of temperature, stress, moisture and aging together through free volume concept. The third one is that under highly dilatant loadings, the free volume approach can result in a natural softening behavior (Knauss and Emri, 1987, Wineman and Min, 1998).

However, under conditions of shear and compressive loadings where the volume is constant or decreasing, the free volume approach fails to give a nonlinear response as the time scale remains constant or increases (McKenna, 1994, Popelar and Liechti, 1997) despite observations of Knauss and Lu (1996) and Popelar and Liechti (1997) in which distortional as well as dilatational strains were found to affect the time scale. Experimental results also suggested that sources of material nonlinearity may exist besides that affecting the time-scale (Schapery, 2000).

c. Differential representation

A differential model by Xia and Ellyin (1998) is chosen as a representative model because it is relatively simple and has been inserted into a general-purpose finite element code, thus facilitating its application. In this model, the total strain rate $\dot{\varepsilon}_t$ is assumed to be the sum of the elastic and creep strain rates, $\dot{\varepsilon}_e$ and $\dot{\varepsilon}_c$, respectively, i.e.,

$$\dot{\varepsilon}_t = \dot{\varepsilon}_e + \dot{\varepsilon}_c \tag{1.11}$$

For a number of Kelvin (Voigt) elements connected in series, creep strain rate $\dot{\varepsilon}_c$ is the sum of the strain rate of each element $\dot{\varepsilon}_{ci}$,

$$\dot{\varepsilon}_c = \sum_{i=1}^{n} \dot{\varepsilon}_{ci} = \sum_{i=1}^{n} \left(a_i \sigma^{\alpha_i} - b_i \varepsilon_{ci} \right) \tag{1.12}$$

The elastic strain rate is calculated through Hooke's law,

$$\dot{\sigma} = E\dot{\varepsilon}_e \tag{1.13}$$

where a_i, b_i $(i = 1, 2, \cdots, n)$ are materials constants, E is elastic modulus.

The problems related to this representation are that the model can simulate the viscoelastic behavior qualitatively, but the quantitative comparison is good only for the class of loading for which the model parameters were fitted.

1.3.3 Multiaxial consideration

As mentioned above, to consider complex stress and strain situations in engineering applications of polymeric structures, considerable effort has been made to develop general, yet simple multiaxial viscoelastic constitutive models. The methods used can be generally grouped into two categories. One is to extend the uniaxial constitutive models for polymers to multiaxial ones, in which an effective stress is used to describe the multiaxial stress states; another effort is to develop multiaxial constitutive models directly based on experimental observations.

a. Effective (octahedral shear) stress theories

To extend the uniaxial constitutive models for polymers to multiaxial situation, the main consideration is to account for the multiaxial stress states. To this end, the multiaxial stress states in three-dimensional constitutive models are: von Mises equivalent stress, or octahedral shear stress. They have been widely used as a parameter to represent the multiaxial stress states (Schapery, 1969b, Zhang et al., 1997). This consideration stems

from the intuitive hypothesis that creep is caused by the shearing of molecules past each other (Lai and Bakker, 1996).

In an effort similar to those made by Pao and Marin (1953), Xia and Ellyin (1998) extended their uniaxial differential nonlinear constitutive model to the three-dimensional situation, i.e., for the creep part:

$$\{\dot{\varepsilon}_c\}=\sum_{i=1}^{n}\{\dot{\varepsilon}_{ci}\}=\sum_{i=1}^{n}\left(a_i[A]^{-1}\sigma_{eq}^{a_i-1}\{\sigma\}-b_i\{\varepsilon_{ci}\}\right) \tag{1.14}$$

The elastic strain rate is still related to the elastic stress rate through the generalized Hooke's law,

$$\{\dot{\sigma}\}=E[A]\{\dot{\varepsilon}_e\} \tag{1.15}$$

In (1.14), σ_{eq} is an equivalent stress, e.g., when von Mises equivalent stress is chosen, then $\sigma_{eq}=\left(\frac{3}{2}s_{ij}s_{ij}\right)^{1/2}$, with $s_{ij}=\sigma_{ij}-\sigma_{kk}/3$, the deviatoric stress components of a stress tensor. $[A]$ is a matrix related to Poisson's ratio.

An extension of the Schapery uniaxial model to three dimensions has been given by several authors, both for isotropic materials (Schapery, 1969, Zhang et al., 1997) and for materials exhibiting anisotropy (Brouwer, 1986, Rooijackers, 1988). For a thermo-rheologically simple viscoelastic material with initial isotropy, one form of 3-D Schapery model, proposed by Zhang et al. (1997), is

$$\{\varepsilon\} = J_0 g_0 [S]\{\sigma\} + g_1 \int_0^t \Delta J(\psi - \psi') \frac{d}{d\tau} \left(g_2 [S]^c \{\sigma\}\right) d\tau \tag{1.16}$$

where [S] and $[S]^c$ are two matrices related to Poisson's ratio and the creep contraction ratio, respectively. Nonlinear functions g_0, g_1, g_2 and ψ have the same definition as those in the uniaxial model. However, for a multiaxial formulation, these functions in general depend on some measure of the multiaxial stress field and von Mises equivalent stress, σ_{eq}, was used here.

b. Hydrostatic stress effect

The equivalent stress, σ_{eq}, initially defined in the above constitutive models accounted for the distortion energy only, i.e., it was the von Mises equivalent stress. However, it has been observed that hydrostatic stress influences the mechanical behavior of polymers (Ward, 1983) and the hydrostatic stress is related to the bulk dilatation energy. One effort made by Lai and Bakker (1996) to account for the hydrostatic stress effect was to introduce the hydrostatic stress term in their modified Schapery equations. Instead of the equivalent stress or octahedral shear stress as the variable of the nonlinear functions g_0 and a_σ, g_0 and a_σ were assumed to be functions of the first stress invariant σ_{kk}, i.e.,

$$g_0 = g_0(\sigma_{kk}), \qquad a_\sigma = a_\sigma(\sigma_{kk}) \tag{1.17}$$

with $g_0(-\sigma_{kk}) = 1/g_0(\sigma_{kk})$, and $a_\sigma(-\sigma_{kk}) = 1/a_\sigma(\sigma_{kk})$, while g_1 and g_2 were still a function of the von Mises equivalent stress.

c. Buckley and McCrum's representation

In the most general case, it is expected that creep strains of a viscoelastic solid subjected to combined tension-torsion stresses are related to the applied stress states by (Buckley and McCrum, 1974)

$$\begin{cases} \varepsilon(t) = \left[\frac{J}{2}(t, I_1, I_2) + \frac{B}{9}(t, I_1, I_2)\right]\sigma \\ \gamma(t) = \frac{J}{2}(t, I_1, I_2)\tau \end{cases} \tag{1.14}$$

where J and B are shear and bulk compliances and I_1 and I_2 are the first and second invariants of a stress tensor, respectively.

Buckley and McCrum (1974) conducted the combined tension-torsion creep tests of a polypropylene well into the nonlinear viscoelastic range and found that $B(t)$ is independent of I_1 and the influence of I_2 on $B(t)$ is negligible, hence, $B(t)$ is only time dependent. Therefore, the final form of the constitutive model becomes

$$\begin{cases} \varepsilon(t) = \left[\frac{J}{2}(t, I_1, I_2) + \frac{B}{9}(t)\right]\sigma \\ \gamma(t) = \frac{J}{2}(t, I_1, I_2)\tau \end{cases} \tag{1.15}$$

Although not much simplification is attained by Eq. (1.15) compared to that of Eq. (1.14), its importance lies in the fact that Eq. (1.15) explains the origin of nonlinearity of viscoelasticity, i.e., the nonlinearity of viscoelasticity enters through the shear deformation behavior. It also shows that hydrostatic component of stress influences the shear behavior, which is confirmed by experiments on other polymers (Lu and Knauss, 1999). Another advantage of this approach is that it makes possible the prediction of deformation under a

multiaxial stress potentially with high accuracy, since there is no need for 'a priori' assumptions concerning the nature of the nonlinearity (Ward, 1983).

From the above discussion, it is seen that various constitutive models have been proposed, with each having various degrees of success under limited loading conditions. However, at present no single nonlinear viscoelastic model gives an adequate description of the mechanical behavior of polymers. Appropriate modeling of the nonlinear viscoelastic behavior usually requires a general understanding of the properties of the material involved. The currently available constitutive models need to be further verified, especially under multiaxial stress states. This, again, raises the need for experimental investigation.

1.4 Failure Behaviors

The expanding role of polymeric structures in load-bearing applications has necessitated the generation of accurate and meaningful material data over the entire range of temperatures and time scales for which the applications are intended. Concurrently, design methodologies must be adapted to the highly nonlinear and time-dependent behavior of polymeric structures. For these reasons constitutive relationships and failure criteria are essential, not only for describing the behavior of the materials, but also for evaluating, and if necessary, modifying the various design tools that had been developed for use on metals. The deformation and failure behavior of polymers is among the most important properties needed for designing with these materials.

In the previous two sections, the nonlinear and time-dependent deformation behavior of polymers was discussed and the models available for describing the observed behavior

were reviewed briefly. Failure behavior of polymers is an area of active development and only an outline is given here.

Polymers display different failure modes such as creep rupture, brittle fracture and cold-drawing, depending on their molecular structures, curing schedule, loading types and environments, etc. A typical deformation behavior till failure is shown in Fig. 1.12.

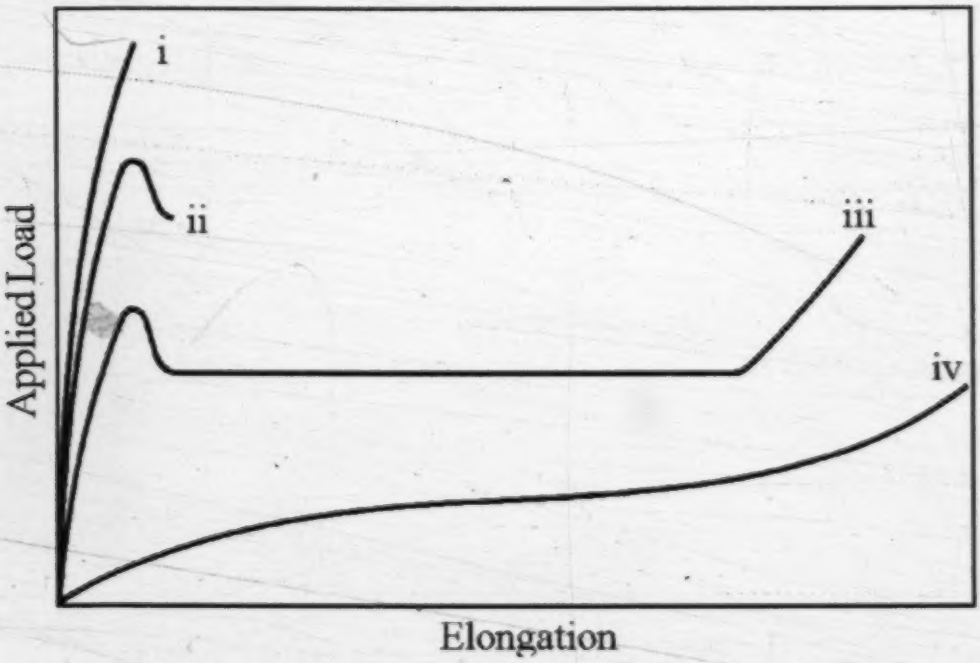

Fig. 1.12 Typical load-Elongation curve for polymers (adopted from Ward, 1983)

At temperatures well below the glass transition (curve i), polymers show brittle failure and rupture occurs at low strains. With slight increase in temperatures, a ductile failure is observed with a yield point followed by a load fall and possibly a neck (curve ii). At higher temperatures one notes change in the post-yield behavior and strain-softening, cold-

drawing, and subsequent strain-hardening are observed (curve iii). At temperatures above glass transition, the stress-strain curve shows rubber-like behavior (curve iv).

Figure 1.12 shows that the temperature has pronounced influence on the failure behavior of polymers. With the increase in temperature, the failure stresses decrease and the failure strains may change appreciably, from a few percent at low temperatures to as high as several thousand percent at high temperatures. Also the failure mode changes from a brittle to ductile one. Other factors such as strain rates, hydrostatic pressures, and molecular structures also change the failure behavior of a polymer (Ward, 1983). Polymers generally show brittle failure under high strain rate, high hydrostatic pressure, and high molecular cross-linkage; ductile failure may be observed under low strain rate, high hydrostatic tensile stress and low molecular cross-linkage.

The quantitative description of these factors can be generally divided into two groups: one from phenomenological or macroscopic experimental observation; another from molecular level, i.e., molecular viscosity (Ward, 1983).

It is widely observed that the yield stresses of polymers are influenced by hydrostatic component of stress (Pae and Bhateja, 1975, Silano, 1982). Therefore, various models have been proposed to account for this effect. Modified von Mises criterion, modified Tresca criterion, and Mohr-Coulomb criterion are three models often used for initially isotropic polymers (Asp et al., 1996, Kody and Lesser, 1997a). Mixed successes were achieved through the application of these models. More general criteria have been proposed for

polymers (Garg and Mai, 1988), with main problem being the lack of experimental data, especially in the third quadrant of principal stress space.

Studies on the dependence of yield stress on strain rate, test temperature, and/or molecular architecture by many researchers (see e.g., Duckett et al., 1978, Lesser and Kody, 1997b) showed that this dependence of yield stress may be described by Eying equation and its modifications (Ward, 1983, Lesser and Kody, 1997b).

Brittle fracture of polymers is another field of intensive study of the failure behavior of polymers (see e.g., Kinloch and Shaw, 1981, Bandyopadhyay, 1990, Garg and Mai, 1988, McKilliam et al., 1998, Vakil and Martin, 1993, Kishi et al., 1998). These studies were motivated by the increasing use of epoxy systems which show brittle behavior under most application environments. The prediction methods of fracture behavior of polymers depend upon whether the fracture is brittle or ductile. If yielding near the crack tip is negligible (i.e., the plastic zone size is small compared to the crack length), fracture is treated by linear elastic fracture mechanics. If yielding is significant, other methods (COD, R-Curve, J-integral, etc.) are more appropriate (Garg and Mai, 1988). These methods are akin to those used in metals. However, the yield behavior at the tip of a crack in polymers may be different from that in metal. For example, glassy polymers subject to tensile loading often yield by crazing, because of the triaxial tensile stress state ahead of the crack tip. Also, viscoelastic phenomenon was observed in the fracture of polymers (McKilliam et al., 1998). One of these models which did have the effect of time-dependence was proposed by Schapery (1990). However, as pointed out by Schapery himself (2000), only opening mode

crack growth had been considered and the kinds of nonlinear viscoelastic behavior dealt with were very limited.

1.5 Objectives of the Current Study

There are many polymer systems used as matrices in fiber-reinforced polymeric composites. They can be classified into two types: thermoplastic and thermoset polymers. Epoxy resins are currently dominant matrix materials used in fiber-reinforced composites because of their superior physical and mechanical properties, such as high strength, high elastic modulus, super adhesiveness and good heat and solvent resistance. Although thermoplastics exhibit good resistance to attack by chemicals and generally good thermal stability, they are very difficult to be impregnated into fine arrays of fibers because of their high viscosity in melt. Compared with other thermosets such as unsaturated polyesters or vinyl esters, epoxy resins are in general tougher, good resistance to heat distortion and less shrinkage during curing. Another significant advantage is the fact that they can be partially cured, so that pre-pregs can be supplied. In fact, epoxies are superior in most respects to the alternative thermosetting systems, which are sometimes preferred simply on grounds of lower cost.

The objective of this research is to study the multiaxial deformation behavior of epoxy polymers, and to develop appropriate viscoelastic constitutive model for the polymer materials, in detail,

1) Comprehensive experimental study of mechanical behavior of epoxy resins. Emphasis will be put on the investigation of the nonlinear viscoelastic behavior, effects of hydrostatic stress, multiaxial behavior and the loading path dependency. Suitable critical experiments will be conducted to delineate the effect of each parameter.

2) Based on the experimental investigation, the possibilities to improve both the current integral or differential forms of viscoelastic models will be explored, an appropriate multiaxial viscoelastic constitutive model for epoxy polymers will be developed. The model ought to properly predict the featured behavior of the epoxy polymers exhibited through the critical test results.

In addition, failure behavior of the epoxy polymers is also experimentally investigated by loading specimens to failure. These tests are supposed to further illustrate the deformation characteristics of epoxy polymers.

Two epoxy resin systems were chosen for this purpose, i.e., EPON 826/EPI-CURE 9551 epoxy system and ColdCure epoxy system.

EPON Resin 826/EPI-CURE Curing Agent 9551 is a bisphenol-A epoxy resin and a non-MDA (methylene dianiline) polyamine system for high performance composite parts designed for processing by filament winding or resin transfer molding. This epoxy system was chosen because it provides high strength, elongation and toughness and, therefore, is suitable as the matrix for filament winding applications currently being used in the researches in the ACME group.

ColdCure epoxy is an EPON 828 epoxy system. It is mainly used as an outdoor repairs, gap filler and other applications. This epoxy system was chosen because it exhibits fairly high strength and superior bonding capabilities. The particular advantage is that it can cure at very low temperature or while in contact with moisture or high humidity and, therefore, is widely used in field bonding.

The deformation and failure behavior of two aforementioned epoxy systems was experimentally studied and a new nonlinear viscoelastic constitutive model in differential form was proposed which accounted for the features exhibited by the two epoxy systems. During different stages of this research, progress achieved was summarized and published in the form of journal papers and conference proceedings. The experimental investigations on the deformation and failure behavior of the ColdCure epoxy resin were documented in two papers, Hu et al. (2000a), (2001). The differential formulation by Xia and Ellyin (1998) was also modified during this investigation to include the hydrostatic pressure effect. The comparison between the predictions by the modified Xia – Ellyin model and the experimental results was published by Hu et al. (2000b) and Ellyin et al. (2000).

In this thesis the emphasis is placed on the higher performance epoxy system, EPON 826/EPI-CURE 9551. Salient results of the ColdCure epoxy are also included for the sake of comparison. In Chapter 2, the EPON 826 and ColdCure epoxy resins are introduced along with the specimen fabrication and. preparation process, the experimental procedure as well as some important points to be taken care of during the specimen preparations and experiments. The mechanical behavior for EPON 826/EPI-CURE 9551 and ColdCure epoxy resins is experimentally investigated and the results are presented and discussed in Chapters 3 and 4, respectively. In Chapter 5, a new differential model is proposed and described in detail. Also included in this chapter is a brief description of a Lai-Bakker model, a modified form of Schapery's integral formulation, which is included herein for a comparative purpose. The new differential model is then utilized to predict the responses of EPON 826/EPI-CURE 9551 under various loading conditions in Chapter 6 and the predictions are compared with the experimental data. The predictive capability of the new

differential formulation is further evaluated in Chapter 7 using the experimental data of ColdCure epoxy resin. Also included in Chapters 6 and 7 are the predictions by the Lai and Bakker model. Finally in Chapter 8, the entire works of this research is summarized and appropriate conclusions are drawn.

Bibliography

1. Anderson, T.L., 1991, Fracture Mechanics: Fundamentals and Applications, CRC Press.
2. Asp, L.E., Berglund, L.A. and Talreja, R., 1996, A Criterion for Crack Initialization in Glassy Polymers Subjected to a Composite-like Stress State, Composites Science and Technology, 56, 1291-1301.
3. Augl, J.M. and Land, D.J., 1985, A Numerical Approach for Obtaining Nonlinear Viscoelasticity Parameters of Polymeric Materials and Composites, Journal of Applied Polymer Science, 30, 4203-4233.
4. Bandyopadhyay, S., 1990, Review of the Microscopic and Macroscopic Aspects of Fracture of Unmodified and Modified Epoxy Resins, Materials Science and Engineering, A124, 157-184.
5. Benham, P.P. and McCammond, D., 1971, Studies of creep and contraction ratio in thermoplastics, Plastic & Polymers, 39, 130-136.
6. Bordonaro, C.M. and Krempl, E., 1992, The Effect of Strain Rate on the Deformation and Relaxation behavior of 6/6 Nylon at Room Temperature, Polymer Engineering and Science, 32, 1066-1072.
7. Brouwer, H.R., 1986, Nonlinear Viscoelastic Characterization of Transversely Isotropic Fibrous Composites under Biaxial Loading, Ph.D., Dissertation, Free University of Brussels, Belgium.
8. Bowden, P.B., 1973, The Yield Behaviour of Glassy Polymers, Chapter 5 of The Physics of Glassy Polymers, Ed. Haward, R.N., Applied Science.
9. Buckley, C.P., 1987, Multiaxial Nonlinear Viscoelasticity of Solid Polymers, Polymer Engineering and Science, 27, 155-164.

10. Buckley, C.P. and Green, A.E., 1976, Small Deformation of a Nonlinear Viscoelastic Tube: Theory and Application to Polypropylene, Philosophical Transactions, Royal Society of London, Series A, Mathematical and Physical Science, 281, 543-566.

11. Buckley, C.P. and McCrum, N.G., 1974, The relation between linear and non-linear viscoelasticity of polypropylene, Journal of Materials Science, 9, 2064-2066.

12. Chen, W. and Zhou, B., 1998, Constitutive Behavior of Epon 828/T-403 at Various Strain Rates, Mechanics of Time-Dependent Materials, 2, 103-111.

13. Chen, Y., Xia, Z. and Ellyin, F., 2001, Evolution of residual stresses induced during curing processing using a viscoelastic micromechanical model, Journal of Composite Materials, 35, 522-542.

14. Christensen, R.M., 1982, Theory of Viscoelasticity, 2nd ed., Academic.

15. Duckett, R.A., Goswami, B.C., Smith, L.S.A., Ward, I.M., and Zihlif, A.M., 1978, The Yielding and Crazing Behaviour of Polycarbonate in Torsion Under Superposed Hydrostatic Pressure, British Polymer Journal, 10, 11-16.

16. Duran, R.S. and McKenna, G.B., 1990, A Torsional Dilatometer for Volume Change Measurements on Deformed Glasses: Instrument Description and Measurements on Equilibrated glasses, Journal of Rheology, 34, 813-839.

17. Ellyin, F., Hu, Y. and Xia, Z., 2000, Multiaxial Behavior and Viscoelastic Constitutive Modeling of Epoxy Polymers, Recent Trends in Constitutive Modeling of Advanced Materials, ASME-AMD-Vol. 239, 13-21.

18. Engineering Materials Handbook, v. 1: Composites, 1987, ASM International.

19. Ewing, P.D., Turner, S. and Williams, J.G., 1972, Combined Tension-Torsion Studies on Polymers: Apparatus and Preliminary Results for Polyethylene, Journal of Strain Analysis, 7, 9-21.

20. Ewing, P.D. , Turner, S. and Williams, J.G., 1973, Combined Tension-Torsion Creep of Polyethylene with Abrupt Changes of Stress, Journal of Strain Analysis, 8, 83-89.

21. Ferry, J.D., 1980, Viscoelastic Properties of Polymers, Wiley, New York.

22. Findley, W.N., Lai, J.S. and Onaran, K., 1976, Creep and Relaxation of Nonlinear Viscoelastic Materials, with an Introduction to Linear Viscoelasticity, North-Holland, Amsterdam.

23. Fotheringham, D.G. and Cherry, B.W., 1978, The Role of Recovery Forces in the Deformation of Linear Polyethylene, Journal of Materials Science, 13, 951-964.

24. Fried, J.R., 1995, Polymer Science and Technology, Prentice-Hall, New Jersey.

25. Fung, Y.C., 1965, Foundations of Solid Mechanics, Prentice-Hall, New Jersey.

26. Garg, A.C. and Mai, Y.-W., 1988, Failure Prediction in Toughened Epoxy Resins, Composites Science and Technology, 31, 225-242.

27. Hasan, O.A. and Boyce, M.C., 1995, A Constitutive Model for the Nonlinear Viscoelastic Viscoplastic Behavior of Glassy Polymers, Polymer Engineering and Science, 35, 331-344.

28. Hu, Y., Xia, Z. and Ellyin, F., 2000a, Mechanical Behavior of an Epoxy Resin Under Multiaxial Loading, Part I, Experimental Study, 8, 11-18.

29. Hu, Y., Xia, Z. and Ellyin, F., 2000b, Mechanical Behavior of an Epoxy Resin under Multiaxial Loading, Part II: Comparison of Viscoelastic Constitutive Model Predictions, Polymers & Polymer Composites, 8, 157-166.

30. Hu, Y., Ellyin, F. and Xia, Z., 2001, An Experimental Investigation of Normal and Shear Stress Interaction of an Epoxy Resin, Polymer Engineering and Science, 41, 2047-2060.

31. Kinloch, A.J. and Shaw, S.J., 1981, The Fracture Resistance of a Toughened Epoxy Adhesive, Journal of Adhesion, 12, 59-77.

32. Kishi, H., Shi, Y.-B., Huang, J. and Yee, A.F., 1998, Ductility and Toughenability Study of Epoxy Resins Under Multiaxial Stress States, Journal of Materials Science, 33, 3479-3488.

33. Kitagawa, M. and Takagi, H., 1990, Polyethylene Under Combined Tension and Torsion, Journal of Polymer Science: Part B: Polymer Physics, 28, 1943-1953.

34. Knauss, W.G. and Emri, I.J., 1981, Non-linear Viscoelasticity Based on Free Volume Consideration, Computers & Structures, 13, 123-128.

35. Knauss, W.G. and Emri, I.J., 1987, Volume Change and the Nonlinearly Thermo-Viscoelastic Constitution of Polymers, Polymer Science and Engineering, 27(1), 86-100.

36. Knauss, W.G. and Kenner, V.H., 1980, On the Hygrothermomechanical Characterization of Polyvinyl Acetate, Journal of Applied Physics, 51, 5131-5136.

37. Kody, R.S. and Lesser, A.J., 1997, Deformation and Yield of Epoxy Networks in Constrained States of Stress, Jurnal of Materials Science, 32, 5637-5643.

38. Kontou, E. and Farasoglou, P., 1998, Determination of the True Stress-Strain Behaviour of Polypropylene, Journal of Materials Science, 33, 147-153.

39. Krempl, E. and Bordonaro, C.M., 1998, Non-proportional Loading of Nylon 66 at Room Temperature, International Journal of Plasticity, 14, 245-258.

40. Lai, J., 1995, Nonlinear Time-dependent Deformation Behavior of High Density Polyethylene, Ph.D. Dissertation, Delft University of Technology, The Netherlands.

41. Lai, J. and Bakker, A., 1995, Analysis of the Non-linear Creep of High-density Polyethylene, Polymer, 36(1), 93-99.

42. Lai, J. and Bakker, A., 1996, 3-D Schapery Representation for Non-linear Viscoelasticity and Finite Element Implementation, Computational Mechanics, 18, 182-191.

43. Lesser, A.J. and Kody, R.S., 1997a, Effect of Molecular Structure on the Yield and Fracture of Epoxy Networks in Multi-axial Stress States, Proceedings of the 1997 55th ANTEC, Toronto, Canada, 3332-3336.

44. Lesser, A.J. and Kody, R.S., A 1997b, Generalized Model for the Yield Behavior of Epoxy Networks in Multiaxial Stress States, Journal of Polymer Science, Part B: Polymer Physics, 35(10), 1611-1619.

45. Lou, Y.C. and Schapery, R.A., 1971, Viscoelastic Characterization of a Nonlinear Fiber-reinforced Plastic, Journal of Composite Materials, 5, 208-234.

46. Lu, H. and W.G. Knauss, W.G., 1999, The Role of Dilatation in the Nonlinearly Viscoelastic Behavior of PMMA under Multiaxial Stress States, Mechanics of Time-Dependent Materials, 2, 307-334.

47. McKenna, G.B. and Zapas, L.J., 1979, Nonlinear Viscoelastic Behavior of Poly(methyl Methacrylate) in Torsion, Journal of Rheology, 23(2),151-166.

48. McKilliam, G., Moltschaniwskyj, G. and Horrigan, D.P.W., 1998, Viscoelastic Phenomena in the Fracture of Thermosetting Resins, Journal of Materials Science, 33, 103-108.

49. Mindel, M.J. and Brown, N., 1973, Creep and Recovery of Polycarbonate, Journal of Materials Science, 8, 863-870.

50. Morland, L.W. and Lee, E.H., 1960, Stress Analysis for Linear Viscoelastic Materials with Temperature Variation, Transactions of the Society of Rheology, 4, 233-263.

51. O'Connor, D.G. and Findley, W.N., 1962, Influence of normal stress on creep in tension and compression of polyethylene and rigid poly(vinyl chloride) copolymer, Journal of Engineering for Industry, 84, 237.

52. Pae, K.D., 1975, The Effects of Hydrostatic Pressure on the Mechanical Behavior of Polymers, Journal of Macromolecular Science, Reviews in Macromolecular Chemistry, C13(1), 1-75.

53. Pao, Y.H. and Marin, J., 1953, An analytical Theory of the Creep Deformation of Materials, Journal Applied Mechanics, 20, 245-252.

54. Peretz, D. and Weitsman, Y., 1982, Nonlinear Viscoelastic Characterization of FM-73 Adhesives, Journal of Rheology, 26(3), 245-261.

55. Popelar, C.F. and Liechti, K.M., 1997, Multiaxial Nonlinear Viscoelastic Characterization and Modeling of a Structural Adhesive, Journal of Engineering Materials and Technology, 119, 205-210.

56. Rooijackers, H.F.L., 1988, A Numerical Implementation of the Schapery Model for Nonlinear Viscoelasticity, Ph.D. Dissertation, Eindhoven University of Technology, The Netherlands.

57. Roy, S. and Reddy, J.N., 1988, A Finite Element Analysis of Adhesively Bonded Composite Joints with Moisture Diffusion and Delayed Failure, Computers and Structres, 29(6), 1011-1031.

58. Schapery, R.A., 1969a, Further Development of a Thermodynamic Constitutive Theory: Stress Formulation. AA&ES Report No. 69-2, Purdue University.

59. Schapery, R.A., 1969b, On the Characterization of Nonlinear Viscoelastic Materials, Polymer Engineering and Science, 9, 295-310.

60. Schapery, R.A., 1997, Nonlinear Viscoelastic and viscoplastic constitutive equations based on thermodynamics, Mechanics of Time Dependent Materials, 1, 209-240.

61. Schapery, R.A., 2000, Nonlinear Viscoelastic Solids, International Journal of Solids and Structures, 37, 359-366.

62. Silano, A.A., 1982, Pressure-Dependent Shear-Deformation Behavior of Polymers, Reviews on the Deformation Behavior of Materials, 4, 49-97.

63. Smart, J. and Williams, J.G., 1972, A Comparison of Single-Integral Non-linear Viscoelasticity Theories, Journal of the Mechanics and Physics of Solids, 20, 313-324.

64. Stassi-D'Alia, F., 1967, Flow and Fracture of Materials According to a New Limiting Condition of Yielding, Meccanica, 3, 178-195.

65. Stassi-D'Alia, F., 1969, Limiting Conditions of Yielding for Anisotropic Materials, Meccanica, 4, 349-364.

66. Struik, L.C.E., 1978, Physical Aging in Amorphous Polymers and Other Materials, Elsevier, Amsterdam.

67. Turner, S., 1966, The Strain Response of Plastics to Complex Stress Histories, Polymer Engineering and Science, 6, 306-316.

68. Turner, S., 1973a, Creep in Glassy Polymers, Chapter 4 of The Physics of Glassy Polymers, ed. Haward, R.N., Applied Science.

69. Turner, S., 1973b, Mechanical Testing of Plastics, Longman, New York.

70. Vakil, U.M. and Martin, G.C., 1993, Yield and Fracture Behaviour of Cross-linked Epoxies, Journal of Materials Science, 28, 4442-4450.

71. Ward, I.M., 1983, Mechanical Properties of Solid Polymers, Wiley, New York.

72. Wineman, A. and Min, J.-H., 1998, Biaxial Yield for Nonlinearly Viscoelastic Materials with a Strain Clock, Mechanics of Time-Dependent Materials, 2, 37-58.

73. Xia Z., and Ellyin F., 1998, Time-dependent Behaviour and Viscoelastic Constitutive Modelling of an Epoxy Polymer, Polymers and Polymer Composites, 6, 75-83.

74. Yi, S. and Hilton, H.H., 1997, Free Edge Stresses in Elastic and Viscoelastic Composites Under Uniaxial Extension, Bending, and Twisting Loadings, Transactions of the ASME, Journal of Engineering Materials and Technology, 119, 266-272.

75. Zhang, C. and Moore, I.D., 1997, Finite Element Modelling of Inelastic Deformation of Ductile Polymers, Geosynthetics International, 4, 137-163.

76. Zienkiewicz, O.C., Watson, M. and King, I.P., 1968, A Numerical Methods of Visco-elastic Stress Analysis, International Journal of Mechanical Sciences, 10, 807-827.

Chapter 2

Test Methodology

Mechanical tests play an important role in materials science and technology. As has been demonstrated in Chapter 1, appropriate modeling of the mechanical behavior of polymers requires a thorough understanding of the properties of the materials involved, and these properties are mostly found through experiments. Therefore, it is very important to design a good test methodology which can provide an insight into the typical characteristics of this type of materials and hence provide a starting point for the further investigation of the mechanical behavior of such materials.

A series of experiments were performed at room temperature to study the deformation and failure behavior of two epoxy resin systems under multiaxial loadings. The experiments were designed to characterize different aspects of the deformation and failure behavior at different stress states; to determine the material properties in the constitutive models and to provide a data source for the development or verification of the currently available and/or newly developed viscoelastic constitutive models. Details of the tested materials and the experimental schemes are given in the following sections.

2.1 Tested Materials

Two different types of epoxy resin systems were tested, i.e., EPON826 and ColdCure from two different companies. The former epoxy system is a product of Resolution

Performance®, and the latter is from Industrial Formulators®. Their compositions are as follow:

EPON826

EPON Resin 826/EPI-CURE Curing Agent 9551 is a bisphenol-A epoxy resin and a non-MDA (methylene dianiline) polyamine system. This system provides a unique combination of high elongation and thermal resistance. It is especially useful in filament winding applications, such as pressure vessels, when high fatigue and microcracking resistance is required. This system has high elongation and toughness, even at low temperature, along with low moisture sensitivity and good resistance to chemical erosion.

ColdCure

ColdCure is an epoxy system from the reaction product of epichlorohydrin and bisphenol A. The hardener is a methylenebiscyclohexylamine. The product cures at a temperature as low as 2 °C. Therefore, it is commercially called ColdCure epoxy. The main advantage of this epoxy is that it exhibits fairly good strength and superior bonding capabilities in temperatures down to 2 °C, or while in moist and humid conditions, therefore, it is very suitable for field bonding.

2.2 Specimen Fabrication

The fabrication of the two epoxy systems was mainly based on the specifications of the companies which provided these two products.

EPON826

EPON 826 epoxy and hardener were mixed with 2.3:1 (volume) or 100/36 (weight), stirred thoroughly and poured into a tubular mould with an outer steel tube and an inner plastic tube (Acrylic or Polycarbonate). The sample was then cured for 2 hours at 50 °C with subsequent post cure for 2.5 hours at 120 °C and cooled to room temperature in the oven prior to machining.

ColdCure

ColdCure epoxy resin and hardener were mixed with 2:1 (volume), stirred thoroughly and poured into a tubular acrylic mould. The sample was then cured for 1 hour at 65 °C and cooled to room temperature and held for 7 days to reach 100% polymerization prior to machining.

Specimens were manufactured from the cast samples on a computer numerical controlled (CNC) lathe that provides for precise machining of any transition profile geometry. The machined geometry is shown in Fig. 2.1. The specimen has a uniform gauge length of 20 mm. The outside and inside diameters in the gauge length are 35.56 mm and 32.56 mm, respectively. The ratio of radius over wall thickness is about 11.4 and, therefore, the specimen can be treated as a thin-walled tubular specimen. This simplifies the calculation of hoop stress within the tubular wall. The outside diameter at the two specimen ends is 40 mm. There is a smooth transition from the ends of the gauge length to the specimen extremities to reduce the stress concentration near the gauge length.

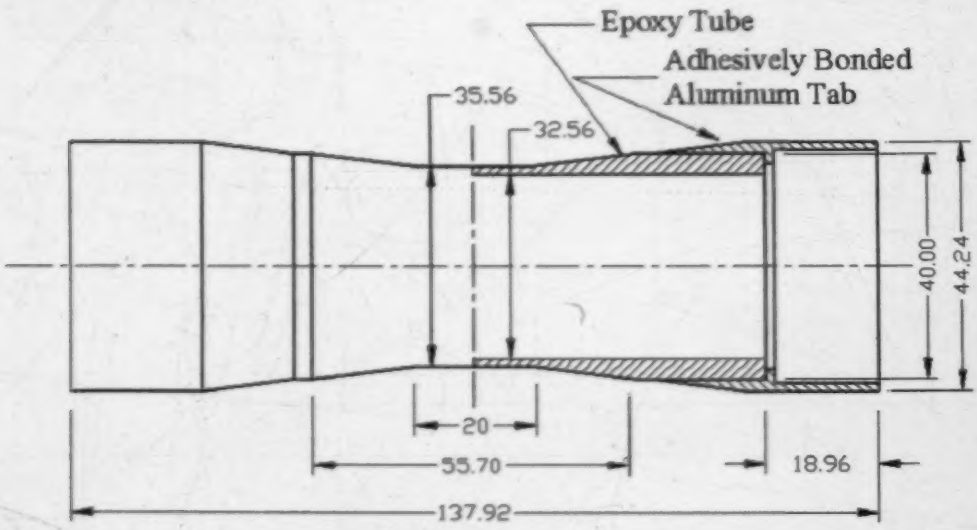

Fig. 2.1 Thin-walled tubular specimen geometry

Aluminum end caps are glued to the tube ends with the 3-M Type DP-460 Epoxy Adhesive so that the specimen can be inserted into the gripping system of the test machine. In this way one avoids damaging the specimen during gripping process. The aluminum end caps were also needed because the contact force between the gripping system and tube specimen will relax with time, if the epoxy tube ends are gripped directly. This will then cause the specimen to slip-out of the gripping system during tensile or fatigue tests, and for the oil to leak during differential pressurization (biaxial tests).

2.3 Testing Facilities

a. Multiaxial testing system

Most experiments were performed in a servo-hydraulic, computer-controlled, multiaxial testing system as shown in Fig.2.2 (see Ellyin and Wolodko, 1997 for detailed description). The main elements of the testing system are: a) the structural components, b) the servo-

hydraulic system, c) the feedback and control system, and d) computer data acquisition and control.

(a)

(b), (c), (d)

Fig.2.2 View of the multiaxial testing system

The structural components shown in Fig.2.2 (a) consists of the gripping system of testing specimen, the load cell, the rotary and linear hydraulic actuators which provide axial force and torque to the specimen while maintaining transverse constraint, the internal and external pressure lines which passes through the center of the load cell and connects to the vessel service manifold, as well as their support structure (Fig. 2.3).

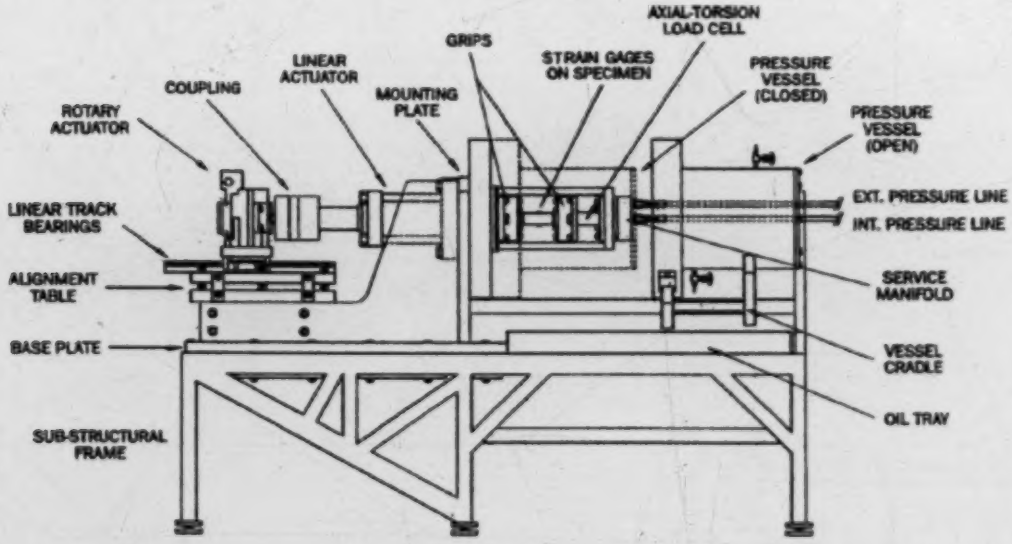

Fig.2.3 Description of the multiaxial testing machine components

(Courtesy of Ellyin and Wolodko, 1997)

The servo-hydraulic system provides loads to the specimen through four independent hydraulic components (Fig. 2.4): a) linear actuator (axial force), b) rotary actuator (torsion), c) internal pressure intensifier and d) external pressure intensifier.

A block diagram of the feedback and control system is shown in Fig.2.5. Control of the hydraulic systems is provided by seven P.I.D. analog controller modules and their associated hardware. The control modules are responsible for providing stable response based on the given feedback signal (transducer measurement) and required command

signal (function generator or computer). Two control modes (stress and strain control) are available for each of the axial, torsion and internal pressure systems.

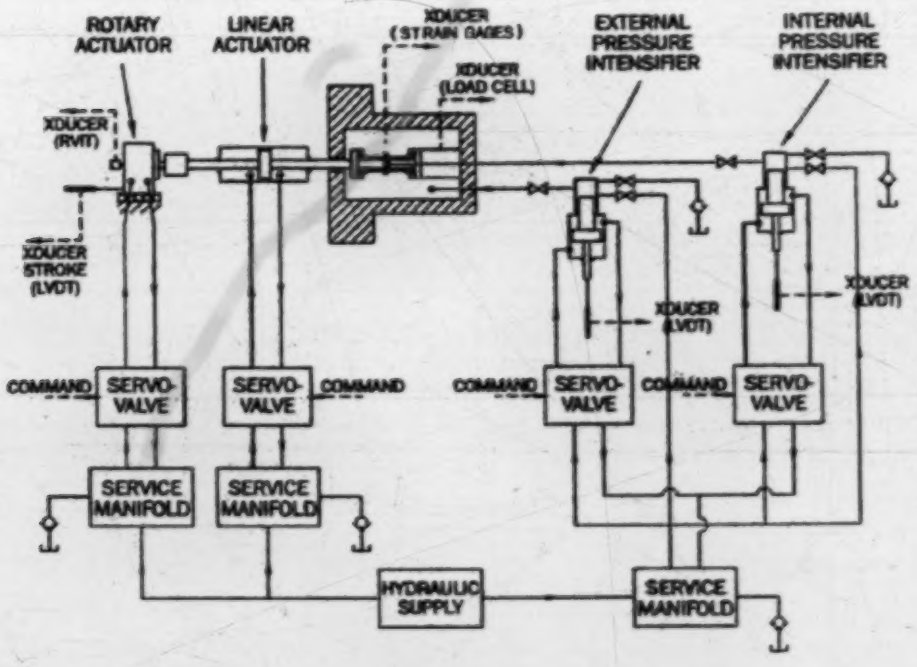

Fig.2.4 Block diagram of the servo-hydraulic system

(Courtesy of Ellyin and Wolodko, 1997)

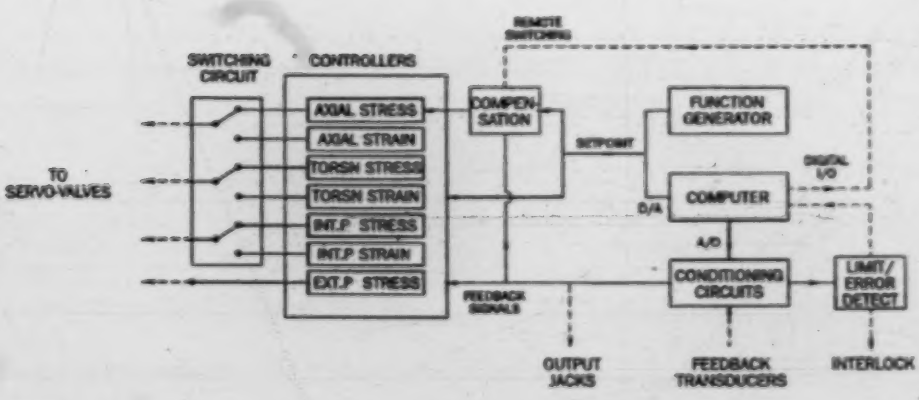

Fig.2.5 Block diagram of the feedback and control system

(Courtesy of Ellyin and Wolodko, 1997)

The computer hardware consists of an 80486/33 PC with two peripheral cards for analog-to-digital (A/D) data acquisition (16 channels), and digital-to-analog (D/A) command signal generation (4 channels). The A/D and D/A cards are interfaced to the transducer conditioning circuits and analog controllers, as shown in Fig.2.5. In order to efficiently sample all transducer channels, an A/D card with burst mode acquisition and Direct Memory Access (DMA) capabilities was utilized. This provides for high speed acquisition rates of up to 100 kHz.

From the above description of the multiaxial testing system, it can be seen that this test facility can apply a combination of axial load, differential pressure (inside and outside pressures) and torsion, and is capable of generating principal stress and strain ratios in all stress/strain quadrants, as well as change in the direction of the applied principal stresses and strains. The maximum capacity of axial load cell is 267 kN with a chosen axial load cell of 22.2 kN for this kind of tests. The maximum capacity of torsional load cell is 1,125 Nm. The internal and external pressure transducers are 68.9 MPa and 34.5 MPa, respectively. Stress/strain controlled, monotonic/cyclic, and in-phase/out-of-phase (non-proportional) tests under ambient temperature conditions, can be performed with this system. The associated computer controlled hardware and software allows for a number of complex user-defined loading and data acquisition schemes.

CEA-13-062UW-350 strain gauges from Micro-Measurements, Co., were used for measuring the strains. These gauges were attached to the tubular specimens with the M Bond, AE-10/15 adhesive system. The strain ranges for the axial and shear strain gauges were all calibrated to ±5% strain with a resolution of 0.0005%.

A pair of strain gauges, one in the axial direction and the other in the circumferential direction, served as an axial and hoop strain transducers (Fig. 2.6). Two additional pairs of strain gauges were used for shear strain measurement. One pair mounted at ±45° to the axial direction served as a shear strain transducer. Another pair, mounted on the opposite surface of the tube specimen, was used to record strains in the ±45° directions. The recorded data from the latter strain gauges served two main purposes. The first was to record the tensile and compressive strain responses under a pure shear stress. Polymers have been shown to be sensitive to hydrostatic stress (Ward, 1971). These results, therefore, can be used as a base data to compare the effect of a superimposed hydrostatic stress. The second purpose was to confirm that the specimen was aligned coaxially with the grip system.

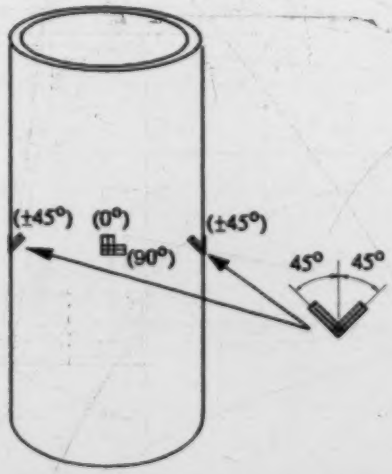

Fig. 2.6 Strain gauge layout for tubular specimens

b. Modified MTS system

Some experiments were conducted in a servo-controlled electro-hydraulic system, a modified MTS system (Ellyin, 1997). A schematic of the biaxial test apparatus is shown in Fig.2.7. A combined of axial load and pressure differential between internal pressure and

external pressure can be applied to the specimen by the system. Because the radial stress is much smaller than the axial and hoop stresses, the state of stress is approximately biaxial with principal stresses in axial and hoop directions.

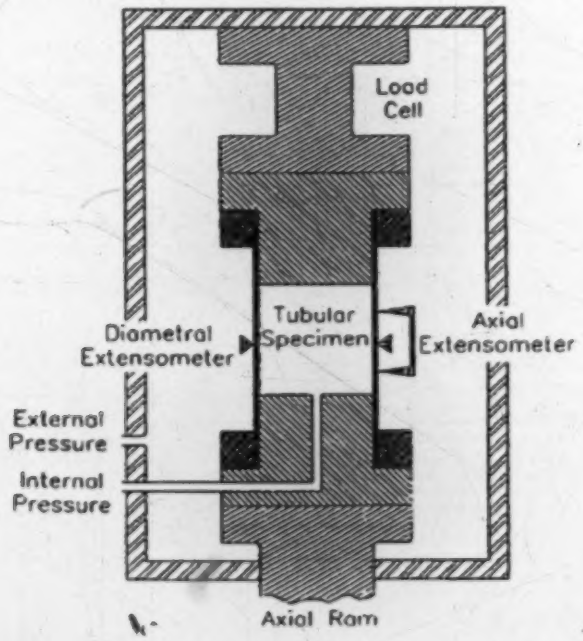

Fig. 2.7 A schematic of the biaxial test apparatus (Courtesy of Xia and Ellyin, 1998)

Since the modified MTS system does not have a hydraulic system to produce a torque to the specimen, it cannot produce a shear stress directly. Except that, the modified MTS system has all other functions of the multiaxial testing system. The controlled mechanisms of the two systems are also similar, therefore, no further introduction is presented for the modified MTS system (see Ellyin, 1997, for more detailed information for the system).

The axial strain was measured by an MTS Model 632.26C-22 extensometer with an output sensitivity of 1.5 mV/V ±2% and a full scale measurement range of ±1.2 mm. The gauge length of the extensometer is 8 mm. The transverse strain was measured by an in-house

manufactured extensometer suitable for a specimen length or diameter within the range of 15 mm to 50 mm, with a full scale range of ±15 mm. The two extensometers were clipped to the specimen by springs or elastics as shown in Fig. 2.7.

All tests were performed at ambient environments (~25 °C and 50% humidity).

2.4 Loading Scheme and Stress State

The loading scheme and stress state for tubular specimens are shown in Fig. 2.8(a). Axial load, pressure differential between internal and external pressures, and torsion can be applied to the specimen simultaneously or in stages, or individually. This then induces axial, hoop and shear stresses within the tube wall, Fig. 2.8(b). The radial stress component, σ_r, is smaller by an order of magnitude and can, therefore, be neglected in comparison to the other two principal stress components. The axial, hoop, and shear stresses imposed on a thin-walled tube, subject to a combined axial load, F, internal pressure P_i, external pressure P_e, and torque T, can be calculated by:

$$\sigma_a = \frac{F}{\pi D t} + \frac{(P_i - P_e)D}{4t} \tag{2.1}$$

$$\sigma_h = \frac{(P_i - P_e)D}{2t} \tag{2.2}$$

$$\tau = \frac{2T}{Dt} \tag{2.3}$$

where D is the mean diameter and t is the thickness of the tube, σ_a, σ_h and τ are the axial, hoop and shear stresses, respectively.

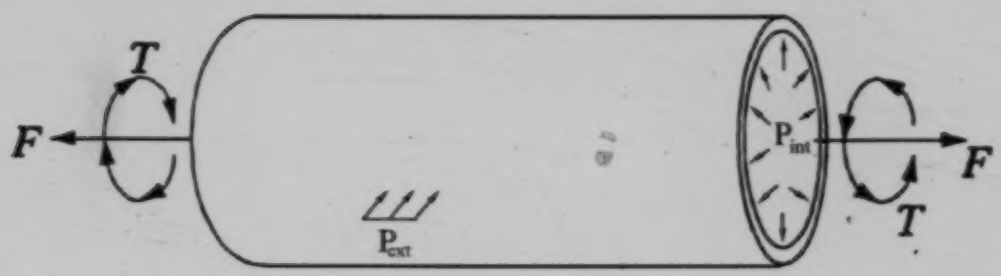

(a)

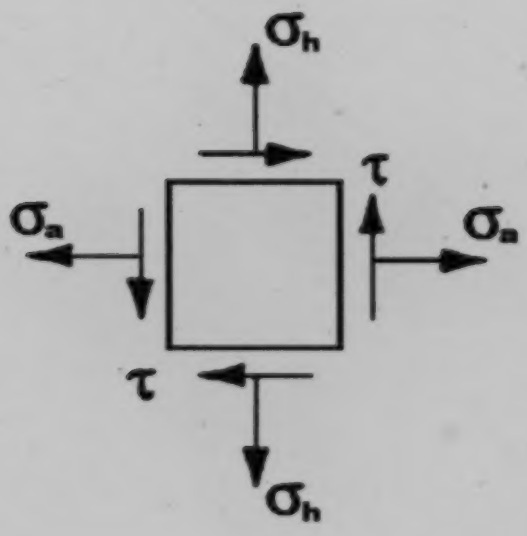

(b)

Fig. 2.8 Loading Scheme (a) and Stress State (b)

In order to compare the mechanical behavior of epoxy resins under different stress states, an equivalent stress is often used. Here the octahedral shear stress, τ_{oct}, is chosen which is defined as:

$$\tau_{oct} = \frac{\sqrt{2}}{3}\sqrt{\sigma_a^2 - \sigma_a\sigma_h + \sigma_h^2 + 3\tau^2} \qquad (2.4)$$

Another important parameter for polymers is the hydrostatic stress, σ_m, which is given by:

$$\sigma_m = \frac{1}{3}(\sigma_a + \sigma_h + \sigma_r) \approx \frac{1}{3}(\sigma_a + \sigma_h) \tag{2.5}$$

with no superimposed hydrostatic pressure p or

$$\sigma_m = \frac{1}{3}(\sigma_a + \sigma_h) - p \tag{2.6}$$

with superimposed hydrostatic pressure p.

2.5 Test Procedures

2.5.1 Creep and recovery tests

Creep tests, including recovery following a creep deformation, are widely used to investigate the viscoelastic behavior of time-dependent materials. During creep tests, a step stress is applied and then held constant for a certain period of time so that a measurable creep strain can develop. Subsequently the stress is removed and the creep strain recovers gradually. If sufficient time is given and the applied stress level is not too high, then the creep strain recovers completely. The time required for a full recovery depends on the tested material and applied stress level. For most viscoelastic materials, the higher the stress level, the longer is the required recovery time. Therefore, one specimen can be used to obtain the creep responses at different stress levels. One of the procedures, using a single specimen, is the so-called "isochronous experiment" (Turner, 1983). In this experiment, the applied stress and the strain response are of the general form depicted in Fig. 2.9. The applied stress magnitude is increased progressively. The periods at zero stress have to be long enough to ensure that recovery is complete before the next cycle begins. The isochronous experiment is clearly advantageous because the time spent on specimen preparation, mounting and measurement is reduced to a minimum, and the inconsistencies that can arise from inter-specimen variability are eliminated. Most importantly, it provides

an immediate measure of the degree of viscoelastic nonlinearity exhibited by most polymers.

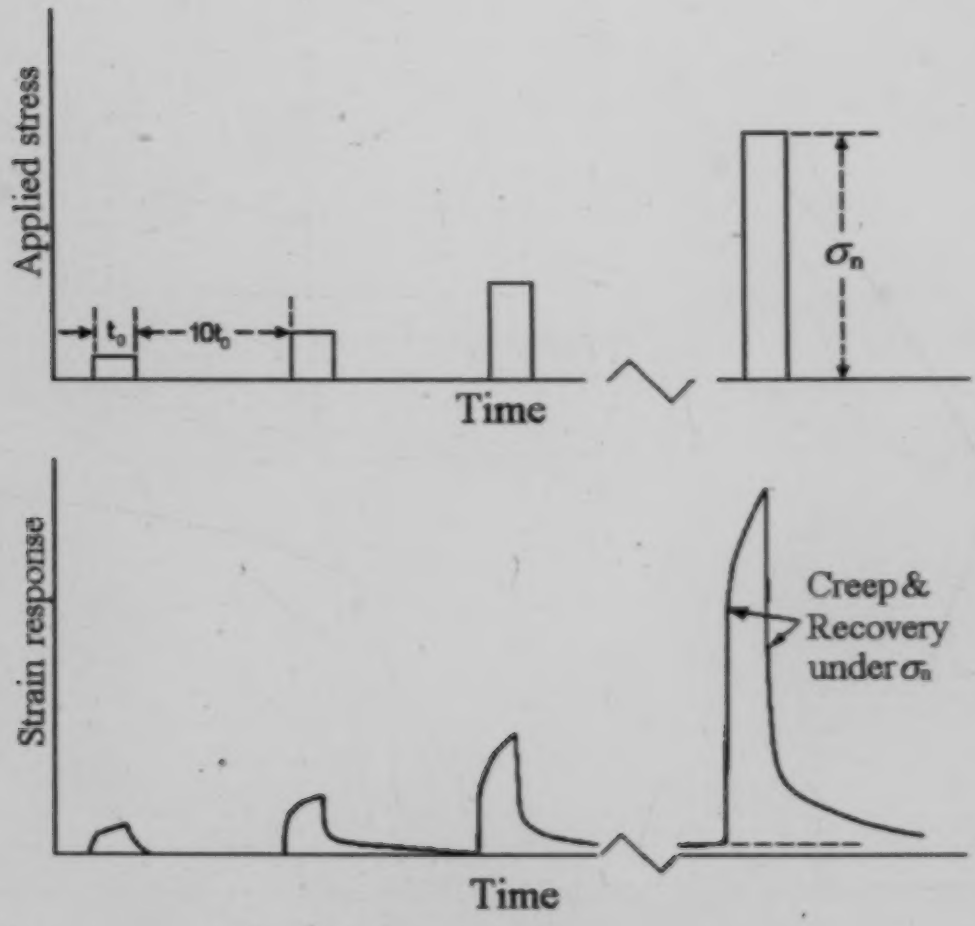

Fig. 2.9 Creep isochronous experiment (adopted from Turner, 1983)

An isochronous experiment was performed for each epoxy system to study their nonlinear viscoelastic behavior. An ideal step stress is impossible to apply because the load application always needs some time to reach the given stress level. Therefore, for the current creep tests, the stresses were applied within 5 seconds. The applied stresses were then kept constant for 1 hour. Following that, the stresses were removed in 5 seconds and

10 hours were allowed for the specimens to recover to their initial state. The resulting creep curves were analyzed for periods beyond 25 seconds, to allow transient loading effects to diminish. The reason for the data being analyzed after 25 seconds will be given later on in this chapter. Also, some stress levels were repeated and the reported creep responses were confirmed.

2.5.2 Hydrostatic stress effect

It is widely noted that hydrostatic stress influences the failure behavior of polymers (Ward, 1971, Silano, 1982). Not only the stress and strain to failure, but also the failure modes may be changed with the increase in hydrostatic stress. There are a few reported experiments to investigate the effect of hydrostatic stress on the deformation behavior of polymers prior to failure. However, a thorough understanding of the pressure-dependent deformation behavior is important, especially for multiaxial constitutive modeling. Therefore, a set of tests was designed to investigate the hydrostatic stress effect on the mechanical behavior of the two epoxy systems.

An ideal test to study the hydrostatic stress effects is a simple shear test with or without a superimposed hydrostatic pressure. The particular advantage of this test scheme is that a shear stress has no hydrostatic stress component; hence, the hydrostatic stress acting on the material is due to the atmospheric environment. For linear viscoelastic materials, shear stress is related only to the distortion deformation while the hydrostatic pressure is related to the volume change, and there is no interaction between these two stress states. Therefore, if the shear deformation behavior under a superimposed hydrostatic pressure is

different from that without the hydrostatic pressure, it can only be attributed to the effect of superimposed hydrostatic pressure.

In this study, the effect of hydrostatic pressure on shear creep deformation was investigated by simple shear tests with or without a superimposed hydrostatic pressure. The stress state for a pure shear stress with a superimposed hydrostatic pressure is demonstrated in Fig. 2.10. A hydrostatic pressure was achieved by applying equal internal and external pressures on the inside and outside walls of tubular specimens.

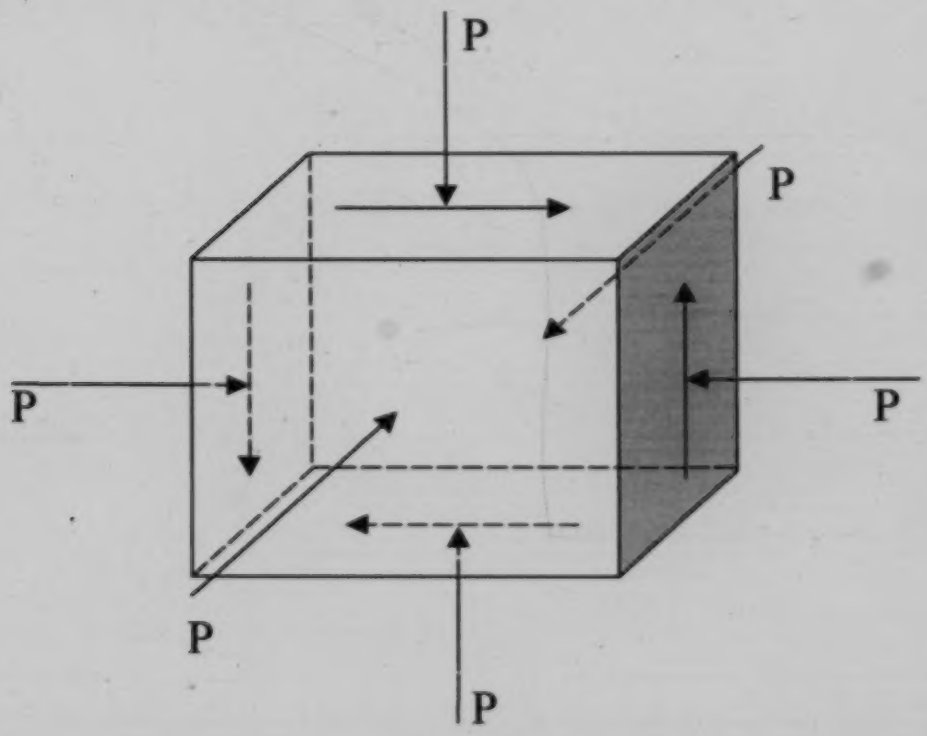

Fig. 2.10 Stress state of simple shear with superimposed hydrostatic pressure

For the tests with a superimposed hydrostatic pressure, the hydrostatic pressure was increased gradually to the specified value of 17.24 MPa (this is the limit of pressure that

the current testing system can attain). The pressure was held constant during the subsequent shear test.

2.5.3 Multiaxial loading

In this investigation, the multiaxial behavior of the two epoxy systems was studied by a loading scheme as illustrated in Fig. 2.11.

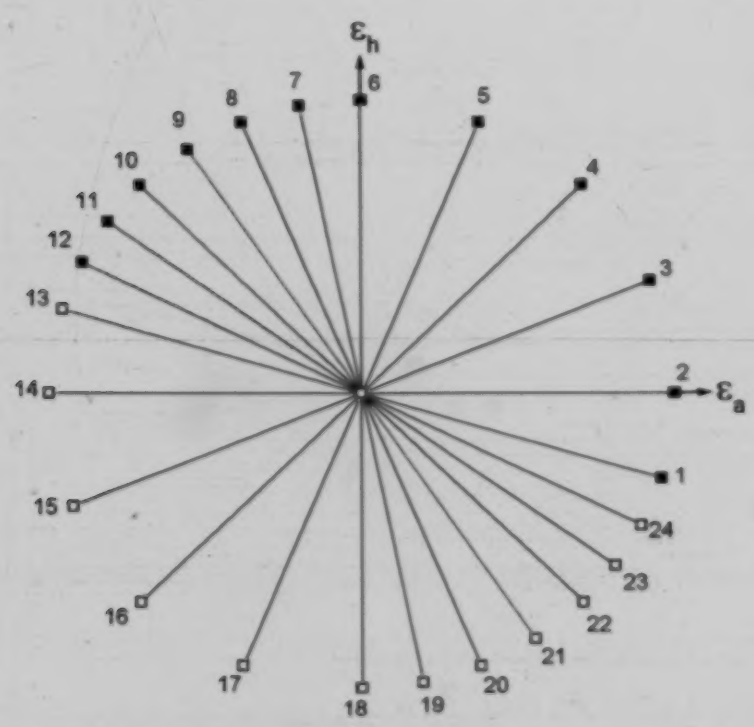

Fig. 2.11 Loading paths in principal strain space

To construct an envelope in the principal strain space, $\varepsilon_a - \varepsilon_h$, one has to choose a criterion so that all points on the envelope represent a defined strain measure for all the strain ratios

shown in Fig. 2.11. There are different definitions of effective strain, e.g. see Ellyin (1997). However, the octahedral shear strain, ε_{oct}, is chosen here, which is given by:

$$\varepsilon_{oct} = \frac{\sqrt{2}}{3}\sqrt{\varepsilon_a^2 - \varepsilon_a\varepsilon_h + \varepsilon_h^2 + \frac{\upsilon}{(1-\upsilon)^2}(\varepsilon_a + \varepsilon_h)^2} \tag{2.7}$$

where ε_a and ε_h can be measured directly by strain gauges or extensometers mounted on the specimens (Figs.2.5 and 2.6).

Since the mechanical behavior of polymers is rate dependent, a constant octahedral shear strain rate, $\dot{\varepsilon}_{oct}$, was imposed along all loading paths of Fig. 2.11. The octahedral shear strain rate, $\dot{\varepsilon}_{oct}$, is defined as:

$$\dot{\varepsilon}_{oct} = \frac{\sqrt{2}}{3}\sqrt{\dot{\varepsilon}_a^2 - \dot{\varepsilon}_a\dot{\varepsilon}_h + \dot{\varepsilon}_h^2 + \frac{\upsilon}{(1-\upsilon)^2}(\dot{\varepsilon}_a + \dot{\varepsilon}_h)^2} \tag{2.8}$$

where $\dot{\varepsilon}_a$ and $\dot{\varepsilon}_h$ are the axial and hoop strain rates, respectively and υ is Poisson's ratio.

Based on a specified combination of ε_{oct} and $\dot{\varepsilon}_{oct}$ values, one then constructs a stress envelope in the biaxial stress space. By changing the combination of ε_{oct} and $\dot{\varepsilon}_{oct}$ values, the effect of strain amplitude and strain rate on the stress envelope can be investigated. All tests were conducted under strain-controlled mode.

In general it may be possible to construct an entire envelope by using a single specimen; thus, avoiding the data scatter through usage of multiple specimens. It was found that as long as ε_{oct} was not too large, upon unloading from the given ε_{oct} and with a certain passage of time, the specimen did return to its original stress/strain state. This is due to the

stress relaxation characteristic of polymers. However, if ε_{oct} was too large or the test was loaded to failure, one specimen had to be used for each loading path. This may bring in the problems of inter-specimen variation. In order to confirm that the specimens for the same stress envelope had the same mechanical properties, uniaxial mechanical responses were compared prior to further testing. The reproducibility of the test results will be explored later on in this chapter.

2.5.4 Loading path effect

During their service, polymeric structures will experience various types of loading histories. Whether the previous loading histories influence the current mechanical behavior of a polymer is of interest to both material scientists and application engineers. Among various possible loading histories, non-proportional loading path is the most severe one and, therefore, often used to study the loading path effect (Krempl and Bordonaro, 1998).

In this investigation, a set of proportional and non-proportional strain-controlled loading scheme as shown in Fig. 2.12, was used to study the path effect. Three different loading paths in the principal strain space were chosen, i.e., $\overline{OAC}$, $\overline{OBC}$ and $\overline{OC}$. Among them, the path $\overline{OC}$ is proportional while paths $\overline{OAC}$ and $\overline{OBC}$ are non-proportional. All three strain paths were loaded at constant strain rate given by

$$\dot{\varepsilon}_{oct} = \frac{\sqrt{2}}{3}\sqrt{(1+\upsilon)^2\dot{\varepsilon}_a^2 + \frac{3}{4}\dot{\gamma}^2} \tag{2.9}$$

where $\dot{\gamma}$ is the shear strain rate.

The two loading paths, $\overline{OAC}$ and $\overline{OBC}$, reach the same point C through applying combined axial and shear strains in strain space in different sequences. The testing procedure consisted of loading to a certain axial (shear) strain value which was then held constant. Subsequently, the shear (axial) strain was increased to the coordinate of point C. This is the so called *corner* test which, as pointed out by Krempl and Bordonaro (1998), is the test often used to test the interaction between different stress/strain components and to distinguish plastic deformation behavior. The loading paths are non-proportional in that the principal stress/strain directions were rotated during the loading process.

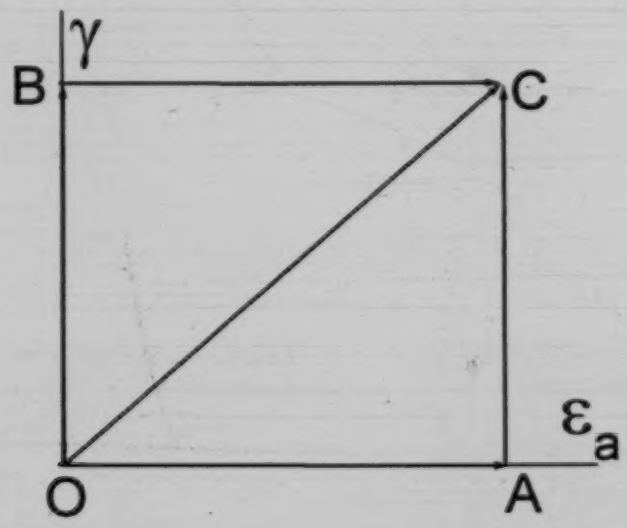

Fig. 2.12 Proportional and non-proportinal strain paths in strain space

The effect of non-proportional loading paths on the mechanical behavior can only be demonstrated by comparing with the proportional one, i.e., path $\overline{OC}$, with similar loading conditions. For polymers, it means that both the proportional and non-proportional loading paths reach point C at the same time and with the same strain rate. However, it is

impossible to reach point C along both the proportional path $\overline{OC}$ and non-proportional path $\overline{OAC}$ or $\overline{OBC}$ at the same time and with the same strain rate, therefore, the stress response from path $\overline{OBC}$ or $\overline{OAC}$ is compared with those from path $\overline{OC}$ with two loading cases. In the first loading case, the loading strain rate for path $\overline{OC}$ is the same as that of path $\overline{OAC}$ or $\overline{OBC}$, therefore, they reach point C at different times. In the second type of tests, point C is reached at the same time by both the porportional and non-proportional loading paths, however, their loading strain rates are different. If there is any difference in the stress responses, it can only be attributed to the different loading paths.

2.5.5 Failure tests

The failure behavior of polymeric materials under combined states of stress is important for the design of modern engineering structures and components. For metals and alloys (elasto-plastic materials), the Tresca and von Mises criteria have been found most applicable in the yield process. Note that both of these criteria emphasize the importance of the shear component of the stress, and neglect any effect of hydrostatic stress component. However, it has been well recognized that a criterion for many polymers must at the very least include pressure dependency effects on failure behavior and, in many cases, the difference in tensile and compressive failure strengths must also be accommodated (Ward, 1971). In the present study, an attempt is made to determine the multiaxial failure behavior of the two epoxy systems and the relative importance of deviatoric and hydrostatic stresses in the failure behavior of the epoxy.

Most of the tests for the failure behavior of the two epoxy resins were conducted under strain control and loaded to failure at a constant octahedral shear strain rate, using tubular

specimens. Because of the buckling problem, some uniaxial compressive tests were performed using solid bars under both stress and strain control modes. Rate effect is also studied by varying the octahedral shear strain rates.

2.6 Specimen Preparation and Testing Considerations

2.6.1 Defect problems

When casting neat (unreinforced) polymers for use as mechanical test specimens, it is critical that voids, inclusions, and similar defects be minimized, both in size and number. Most thermoset polymers used as matrices, even those considered to be toughened, tend to be relatively brittle, and thus their ultimate strengths are strongly dictated by critical flaw sizes.

Inclusions can be present in impure resin as obtained from the supplier, or introduced during the fabrication process (e.g., inadequately cleaned molds, airborne dirt particles, inadequate mixing of components, etc.). In the current specimen preparations, acetone was used to clean the molds. Although mixing nozzle was helpful in mixing the epoxy and the hardener, it was found that the mixture was not even enough and hand stirring was still needed.

Defects can also be in the form of surface scratches, edge chips, and mold marks. After samples were fabricated, they were machined at our Machine Shop. The purpose was to machine the samples to their final shape and, at the same time, obtain a smooth surface.

Two typical sources of voids were found: one from trapped air when pouring the mixture into the mold; the other was attributed to volatiles produced during the stirring. A vacuum may be applied to drain the air and volatiles out during the initial stage of the cure cycle, either while the polymer is still in the mixing container or already in the mold. If the polymer is vacuumed in the mixing container, caution must be exercised to avoid too long a time. This is because the mixture's internal temperature may become very high due to the internal heat generated. At this high temperature, the mixture is gelled and, thus, it becomes very difficult to pour the mixture into the mold.

It was also found that preheating the epoxy is very useful in reducing the voids. Because epoxy is very viscous at room temperature, this introduces two problems: the first is that it is difficult or may take a long time to stir evenly; the other problem is that the escape of trapped air or produced volatiles becomes difficult.

2.6.2 Curing procedure

The final mechanical properties of the epoxy resins are closely related to the curing procedure used. Different curing procedures may be chosen even for the same polymer depending on the specific conditions such as sample size. The manufacturer's suggested curing temperature for EPON 826/EPI-CURE 9551 was 80 °C for 2 hours followed by 120°C for 2.5 hours. However, the specimens for this research were very thick (see Fig. 2.1), with an inside diameter of 25.4 mm and an outside diameter of 50.8 mm for the molds, the internal heat generated during pre-heating is not easy to dissipate. Therefore, the accumulated heat raised the temperature as high as 200 °C, see Fig. 2.13. At this temperature, hyper-polarization may occur at the molecular level, where the curing agent

will reopen bonds that have already formed in the epoxy, because there is so much excess heat energy in the sample. By reopening these molecular bonds, the mixture is releasing more energy and will effectively burn itself out. Besides the epoxy is already above the boiling point before the mixture has gelled/solidified, thus promoting bubble formation in a sample that has almost gelled, and then these bubbles and other volatiles become trapped in the mixture upon solidification. Therefore, a lower pre-cure temperature was used to allow the epoxy to expel all the undesirable volatiles and water moisture into the air while gelling, and then continue the process by solidifying completely.

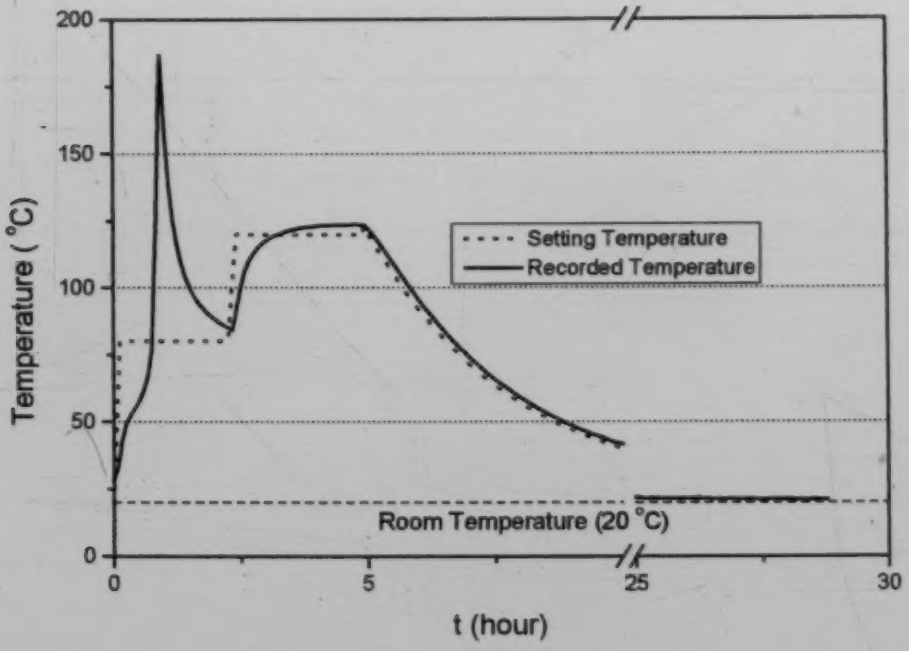

Fig. 2.13 Recorded temperature at the suggested curing procedure

However, the pre-cure temperature can not be too low, otherwise air bubble and volatiles will be trapped inside because the high viscosity of epoxy at low temperature prevents them from escaping.

After a number of trials, it was found that a 50 °C pre-cure for 2 hours followed by a 120 °C post-cure for 2.5 hours gave a reasonable compromise between the low viscosity required for trapped air bubble and volatiles to escape and the low temperature required for the bulk sample curing. The corresponding curing temperature is shown in Fig. 2.14.

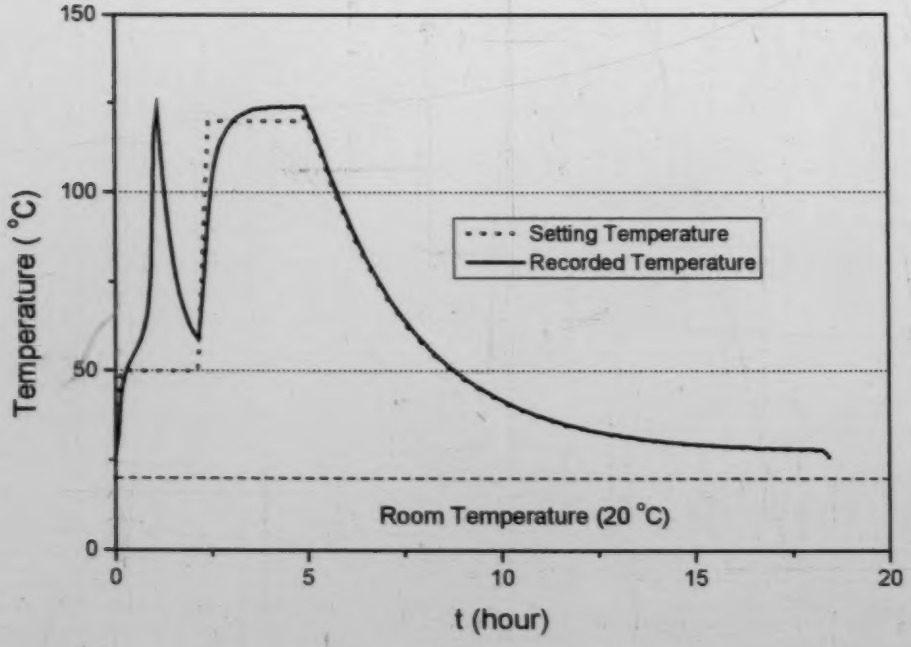

Fig. 2.14 Recorded temperature for a curing schedule of 50°C for 2 hours and 120°C for 2.5 hours

2.6.3 Creep tests

A series of creep and recovery experiments (i.e. the isochronous experiments) were carried out in order to characterize the nonlinear viscoelasticity and determine the properties of the materials.

An idealized creep test may be depicted by a step function, as shown in Fig. 2.15a. In practice, however, it is impossible to apply a stress instantaneously. Instead, a certain period t_0 is needed to ramp the stress from zero to the specified level at which the stress is afterwards held constant (see Fig. 2.15b). The duration of ramping t_0 governs the amount by which the initial creep deformation measured deviates from the real creep response. The discrepancy between the two responses has been studied by Turner (1983).

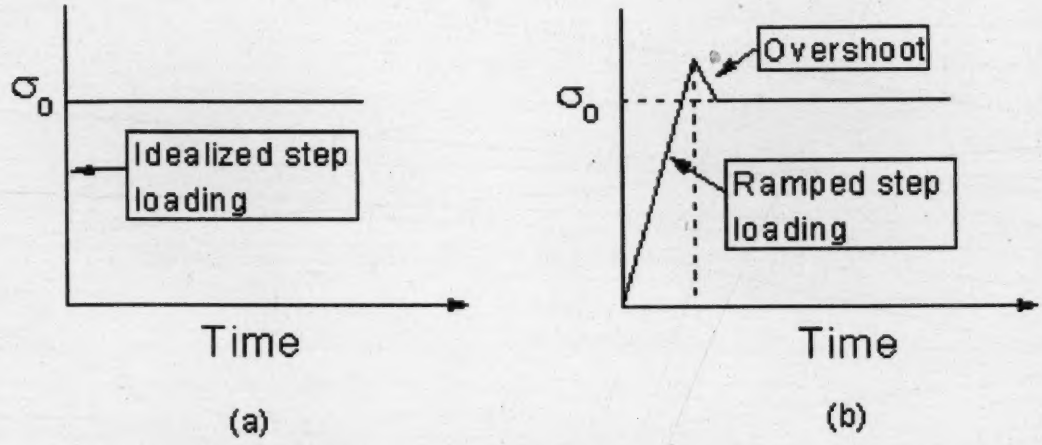

Fig. 2.15 Idealized step loading (a) and ramped step loading used in practice (b) (adopted from Lai, 1995)

It is seen from Fig. 2.16 that when the creep time t is less than $5t_0$, there is a considerable discrepancy between the response to an 'ideal' creep in which the stress is applied instantaneously and the response to a ramped creep test. When t is longer than $10t_0$, this discrepancy becomes negligible. For this reason it is desirable to ramp the load as quickly as possible. However, the quick ramp for loading, causes considerable overshooting (Fig.2.15b). In our tests the ramp time was set to be 5 seconds and no overshoot was observed.

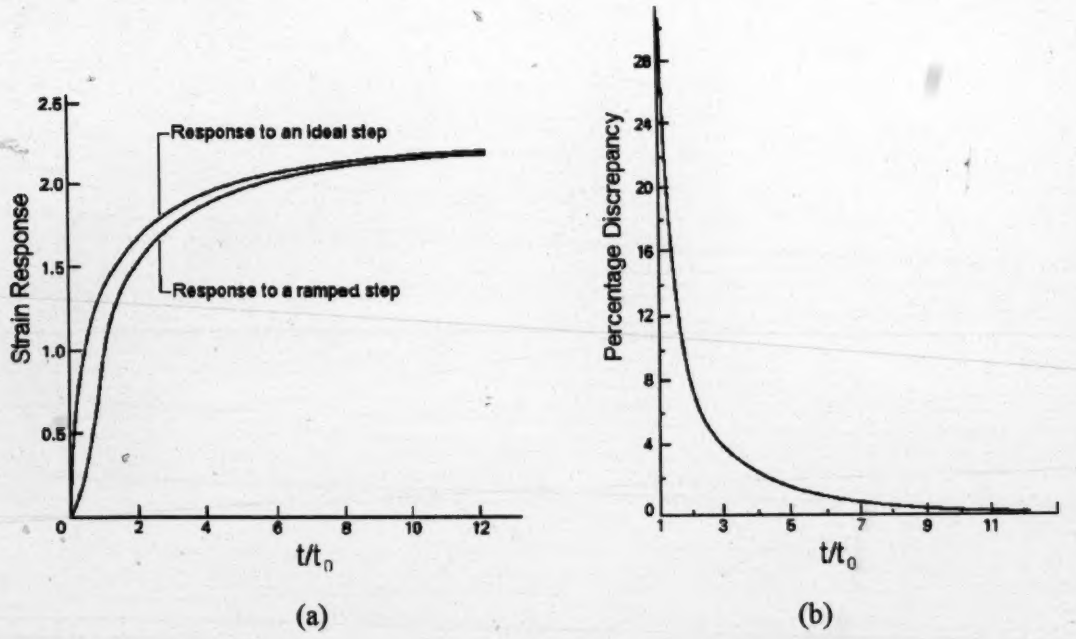

(a) (b)

Fig. 2.16 (a) The strain response to a true step excitation of stress, compared with that a ramped step; (b) Discrepancy between the two responses (adopted from Turner, 1983)

2.6.4 Reproducibility of experimental data

There are a number of factors which influence the mechanical properties of polymers. These factors includes manufacturing process, curing schedule, store environments, store time, etc. Data scatter is always a problem in experimental study of polymers (Ewing, et al., 1972, 1973, and Lai, 1995). In order to obtain reliable data, repeated tests should be performed and data scatter should be analyzed.

In this investigation, the stress-strain curves at the same strain rate were measured before the main experiments were started, because the variation in the results of these tests was deemed to be a measure of the experimental accuracy and the inter-specimen variability,

though the two factors cannot be separated in such a simple experiment. Figure 2.17 shows a comparison between two ColdCure epoxy specimens.

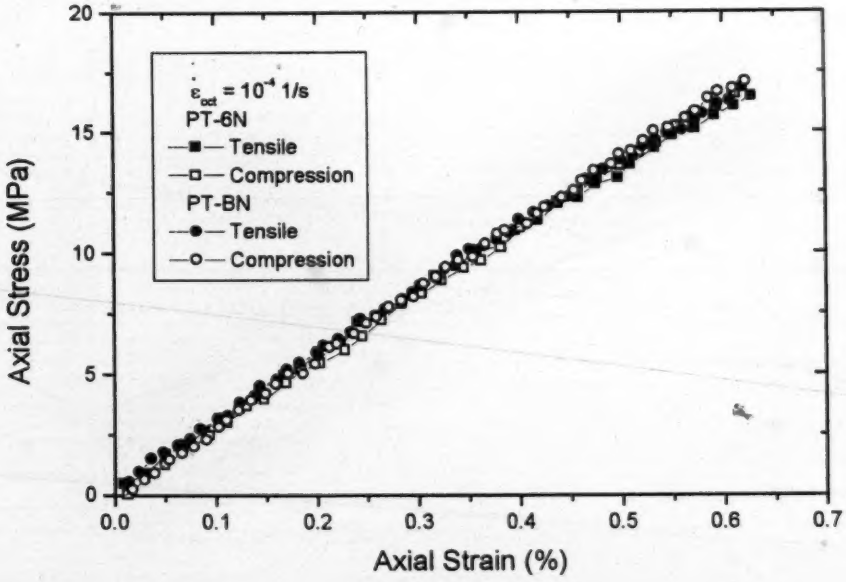

Fig. 2.17 Comparison of tensile and compressive mechanical responses of two specimens at a constant $\dot{\varepsilon}_{oct}=10^{-4}s^{-1}$ for ColdCure epoxy. (Note that in this figure, the sign of compressive stresses is changed to a positive one)

As polymers show both elastic and viscous behavior, the above method could only check the elastic part of the mechanical behavior of polymers because the strain rate is relatively high, therefore, there is not enough time for the viscous behavior to develop. It was found that although the elastic part is comparable in some cases, the viscous part may show discernible difference. Thus, two or more specimens were used for the same kind of tests and the average data were used to represent the test results.

It was found the ColdCure epoxy has a much bigger degree of scatter than that of EPON 826. A number of factors may be involved. One of these is attributed to different batches of

the original materials. The specimens for the ColdCure experiments were manufactured from three different batches. Because the mechanical properties of polymers are strongly dependent on their fabrication processes, it is expected that different batches may produce different properties. Another factor is that the amount of the trapped air could vary among the specimens. Although the superior curing ability at low temperature is an advantage for ColdCure epoxy in its applications, it also make it difficult for trapped air to escape before it is cured. Therefore, most of the volatiles produced during the stirring remain inside the samples and these cause change in density and lead to pre-mature failure.

2.6.5 Physical aging effect

Physical aging affects the elastic as well as the creep compliance of polymers, especially in long-term tests. Therefore, physical aging effect has to be considered if the same epoxy specimens are used for many tests, which may last long time.

For the tests in this research, all the tests except the creep-recovery tests were completed within one day while the creep-recovery tests lasted a few days, therefore, the physical aging effect might not be significant. Also efforts were made to ensure that all specimens had the same shelf-life before being tested.

Bibliography

1. Ellyin, F., Fatigue Damage, Crack Growth and Life Prediction, Chapman & Hall, London, 1997.
2. Ellyin, F. and Wolodko, J.D., 1997, Testing Facilities for Multiaxial Loading of Tubular Specimens, ASTM STP 1280, 7-24.
3. Ewing, P.D., Turner, S., and Williams, J.G., 1972, Combined Tension-Torsion Studies on Polymers: Apparatus and Preliminary Results for Polyethylene, Journal of Strain Analysis, 7, 9-22.
4. Ewing, P.D., Turner, S., and Williams, J.G., 1973, Combined Tension-Torsion Creep of Polyethylene with Abrupt Changes of Stress, Journal of Strain Analysis, 8, 83-89.
5. Krempl, E. and Bordonaro, C.M., 1998, Non-proportional Loading of Nylon 66 at Room Temperature, International Journal of Plasticity, 14, 245-258.
6. Lai, J., 1995, Nonlinear Time-Dependent Deformation Behavior of High Density Polyethylene, Ph.D. Dissertation, Delft University of Technology, The Netherlands.
7. Silano, A.A., 1982, Pressure-Dependent Shear-Deformation Behavior of Polymers, Reviews on the Deformation Behavior of Materials, 4, 49-97.
8. Turner, S., 1983, Mechanical Testing of Plastics, Longman, New York.
9. Xia Z., and Ellyin F., 1998, Time-dependent Behaviour and Viscoelastic Constitutive Modelling of an Epoxy Polymer, Polymers and Polymer Composites, 6, 75-83.
10. Ward, I.M., 1971, Review: The Yield Behaviour of Polymers, Journal of Materials Science, 6, 1397-1417.

Chapter 3

Mechanical Behavior of EPON 826/EPI-CURE 9551

The mechanical behavior of EPON 826 epoxy was studied by a series of tests and the results will be presented in this chapter. The tests can be generally divided into two groups which deal with different aspects of the mechanical behavior of the epoxy resin. One group is related to the deformation behavior such as viscoelastic behavior, hydrostatic stress effect, multiaxial behavior, and loading path effect. The second group deals with the failure behavior including failure modes and failure stress envelopes. These results provide resource of data for the development and verification of constitutive models for polymers. The general test methods have already been introduced in Chapter 2, and some special methods used for this epoxy will be presented where needed.

3.1 Viscoelastic Behavior

3.1.1 Creep and recovery tests

The stresses for creep tests of EPON 826 were applied in 5 seconds and then kept constant for one hour. Fourteen different stress levels, ranging from 11.29MPa to 63.54MPa, were applied and the corresponding strain responses are shown in Fig. 3.1. It is seen that the creep strains at low stress levels ($\sigma_0 \leq 22.76MPa$ where σ_0 is the applied step stress) are relatively small, but they increase appreciably at higher stress levels. Creep strains increase continuously with a decreasing rate at all stress levels, although the trend is less significant at low stress levels and more pronounced at high stress levels.

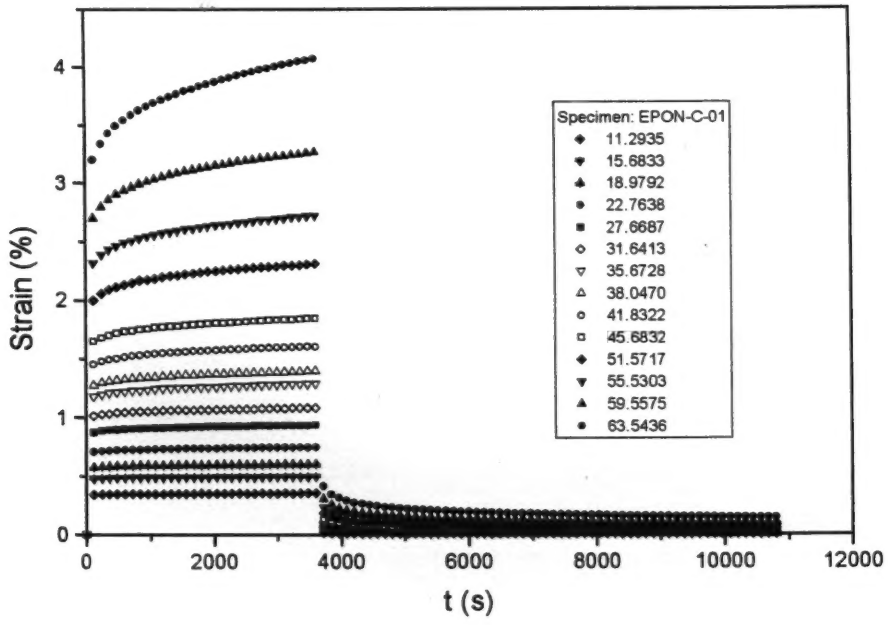

Fig.3.1 Creep and recovery curves at different stress levels

Upon the removal of the applied stress, the strain data were recorded up to two hours during the recovery process as shown in the figure. Since the strains at the recovery stage are too small to be distinguished clearly, especially at lower stress levels, an enlarged figure only, for the recovery part, is presented in Fig.3.2. This figure indicates that following the stress removal, the creep strains recover at a continuously decreasing rate. Both figures show that mechanical behavior of the tested epoxy is time-dependent.

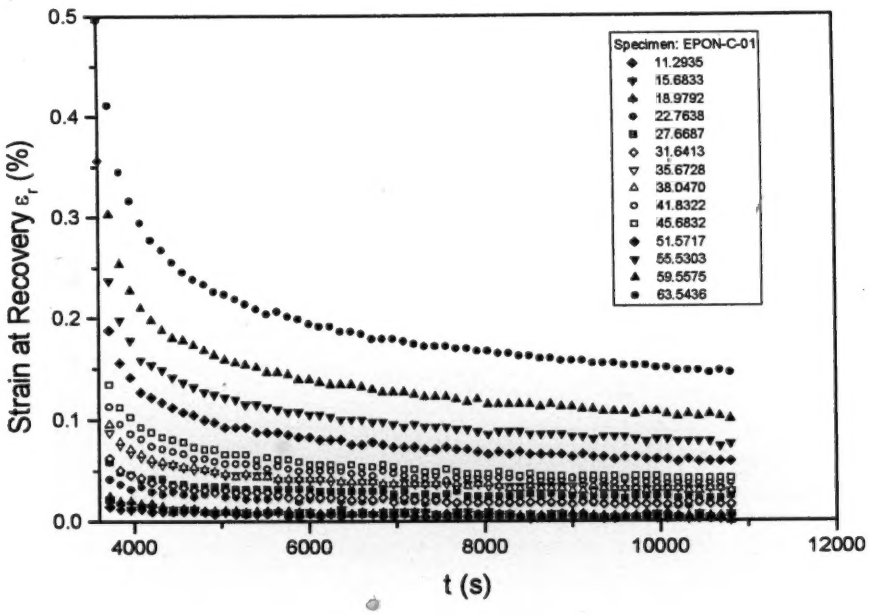

Fig.3.2 Recovery curves at different stress levels

Since a single specimen was used for all the creep tests, 10 hours were allowed between any two tests for the strain to recover. It was found that after 10 hours, there were no residual strains at low stress levels and a small amount at high stress levels. For test at the highest stress level of 63.54 MPa, the residue strain after 10 hours was 0.062%, which is very small compared to the maximum creep strain of 4.07% at this stress level. This then confirms a truly viscoelastic behavior of this epoxy resin.

Creep-recovery curves can be used to show not only the time effect, but also nonlinear behavior of the epoxy resin. Figure 3.3 depicts the creep compliances at different stress levels for the same set of creep-recovery tests. The creep compliance, $D(\sigma_0, t)$, is defined as

$$D(\sigma_0,t)=\frac{\varepsilon_a(t)}{\sigma_0} \tag{3.1}$$

where σ_0 is the applied constant stress and $\varepsilon_a(t)$ is the corresponding creep strain. For linear viscoelastic materials, $D(\sigma_0,t)$ should be independent of σ_0 and only a function of time following the load application (Krishnaswamy et al., 1992).

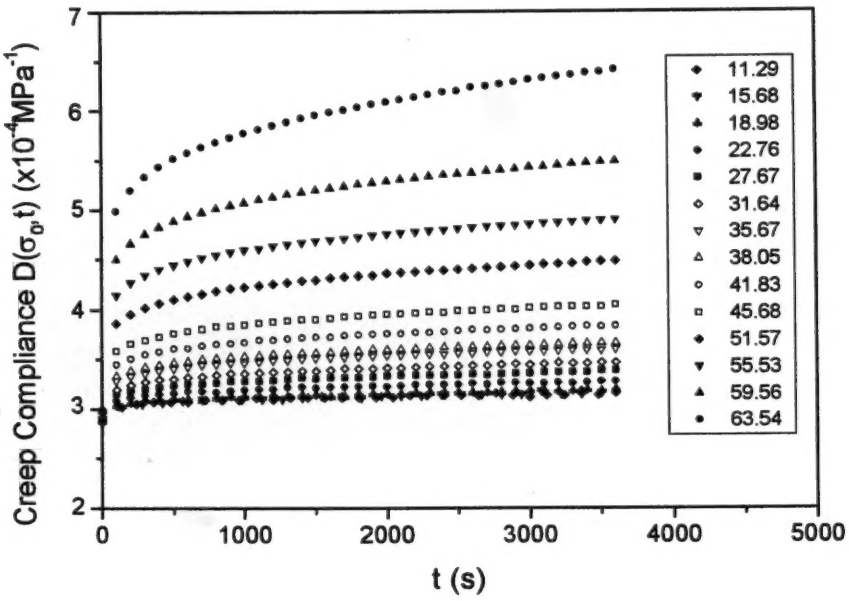

Fig.3.3 Creep compliance curves at different stress levels

From Fig.3.3 it is seen that up to 18.98 MPa, the creep compliance curves collapse on to one; and thus, the epoxy manifests a linear behavior. For the stress levels higher than 22.76 MPa, the creep compliance curves are separated from each other and they are dependent on the current applied stress level, therefore, the epoxy behavior becomes nonlinear.

Another useful property drawn from the creep-recovery tests is Poisson's ratio, υ, which is obtained by measuring the hoop strain, $\varepsilon_h(t)$, while creep-recovery tests were underway. Poisson's ratios $(-\varepsilon_h(t)/\varepsilon_a(t))$, was calculated for all stress levels and an approximately constant value was obtained. Figure 3.4 shows the value for Poisson's ratio at the stress level of 45.68MPa. It is seen that at the creep stage, Poisson's ratio is independent of time and has a value of about 0.42. The ratio appears to vary significantly during the recovery stage. Note that the ratio $\left(-\varepsilon_h(t)/\varepsilon_a(t)\right)$ during recovery is not considered to represent the actual Poisson's ratio of the epoxy, because the rate may be significantly influenced by measurement error of the testing system due to the small axial and hoop strain values at the recovery stage.

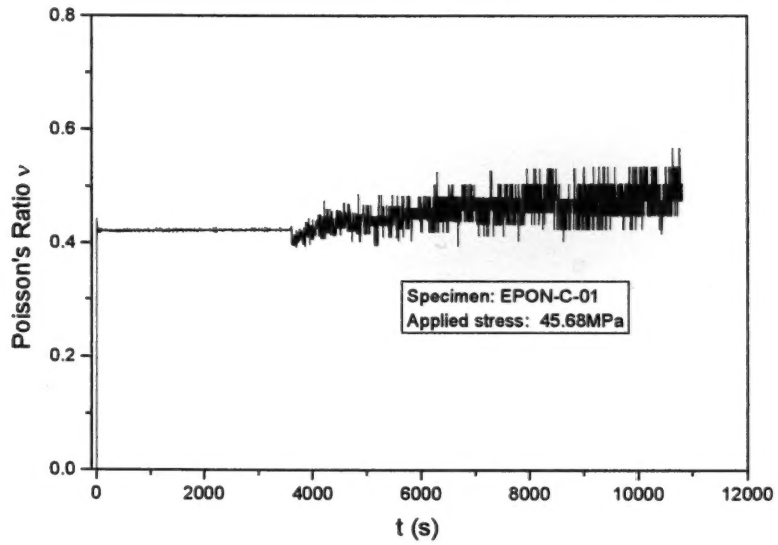

Fig.3.4 Poisson's ratio at the applied stress level of 45.68MPa

Creep-recovery curves may also be used to characterize the material parameters and/or functions for some viscoelastic constitutive models, see e.g. Lou and Schapery (1971).

These curves will be used later in Chapters 5 and 6 to characterize the constitutive model parameters and/or functions.

3.2. Hydrostatic Stress Effect

Figure 3.5 shows two shear stress-strain curves: one with a superposed hydrostatic pressure of 17.24 MPa, the other without superimposed hydrostatic pressure. Both tests were performed under shear strain control with the same octahedral shear strain rate of $10^{-4}\ s^{-1}$. It can be seen that the stress response for the test with a superimposed hydrostatic pressure is slightly higher than that under atmospheric environment. However, the difference is not significant at the tested hydrostatic pressure level.

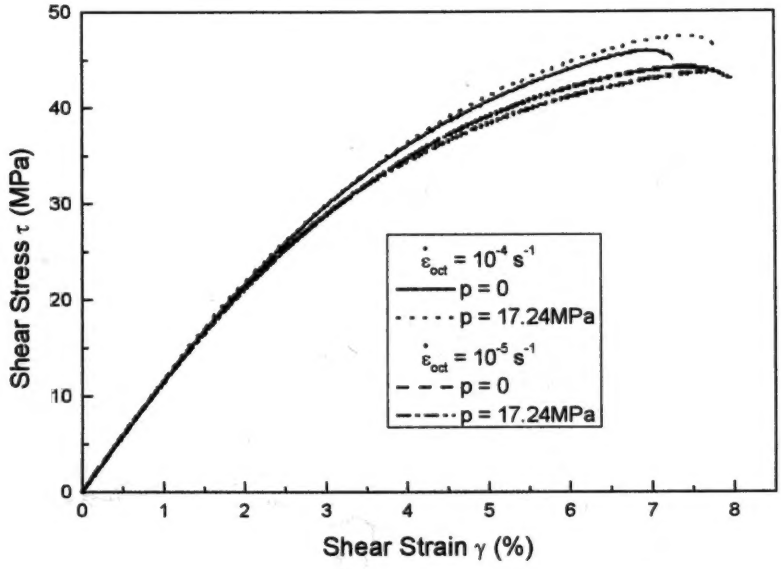

Fig.3.5 Shear stress-strain curves for $\dot{\varepsilon}_{oct} = 10^{-4}\ s^{-1}$ and $\dot{\varepsilon}_{oct} = 10^{-5}\ s^{-1}$ with or without a superposed hydrostatic pressure of 17.24 MPa

As time plays an important role in polymeric materials, another set of tests was performed to further check the effect of hydrostatic pressure. The only difference between this set of tests and the previous one, is that the octahedral shear strain rate for this set is an order of magnitude lower than the previous ones, i.e., $10^{-5}\ s^{-1}$. It can be seen from Fig.3.5 that similar trend with respect to the hydrostatic pressure effect is observed for this set of tests despite the time scale being increased by a factor of 10. Note that a lower strain rate results in a lower stress, c.f., Fig. 3.5. Although the influence of hydrostatic pressure at the tested pressure level is not significant, a hydrostatic component of stress does have an effect on the deformation behavior of this epoxy resin as it can be seen from the multiaxial tests at higher hydrostatic stress levels in the next section.

3.3. Multiaxial Behavior

From preliminary experimental observations of this epoxy, it was found that only at a relatively high stress/strain ranges, the octahedral shear-strain curves for different loading paths were different from each other. Therefore, the tested stresses or strains were 80 to 90 percent of the corresponding failure stresses or failure strains for each loading path. One specimen was utilized for each loading path. It was found that the repeatability for this epoxy is very good. Four typical paths were tested which correspond to uniaxial tensile and compressive ($\varepsilon_h / \varepsilon_a = -\upsilon$), equibiaxial tensile and pure shear (2nd quadrant). Due to material isotropy, the stress values for the tensile and compressive in the hoop direction, and pure shear (4th quadrant) are assumed to be the same (material symmetry). There is no data point in the third quadrant because of the occurrence of buckling in the range of applied strains.

3.3.1 Stress envelope for octahedral shear rates

The stress envelopes for a fixed octahedral shear strain of 2.5% at three different octahedral shear strain rates of $10^{-3}\ s^{-1}$, $10^{-4}\ s^{-1}$, and $10^{-5}\ s^{-1}$ are depicted in Fig.3.6. It is seen that the stress envelopes expand with the increase in strain rate. The test points for the octahedral shear strain rate of $\dot{\varepsilon}_{oct}=10^{-4}\ s^{-1}$ are compared with a von Mises envelope as shown in Fig.3.6 with dotted line. Here, von Mises equation is defined as

$$\sigma_a^2-\sigma_a\sigma_h+\sigma_h^2=\sigma_0^2 \tag{3.2}$$

where σ_0 is the uniaxial tensile stress corresponding to $\varepsilon_{oct}=2.5\%$ and $\dot{\varepsilon}_{oct}=10^{-4}\ s^{-1}$.

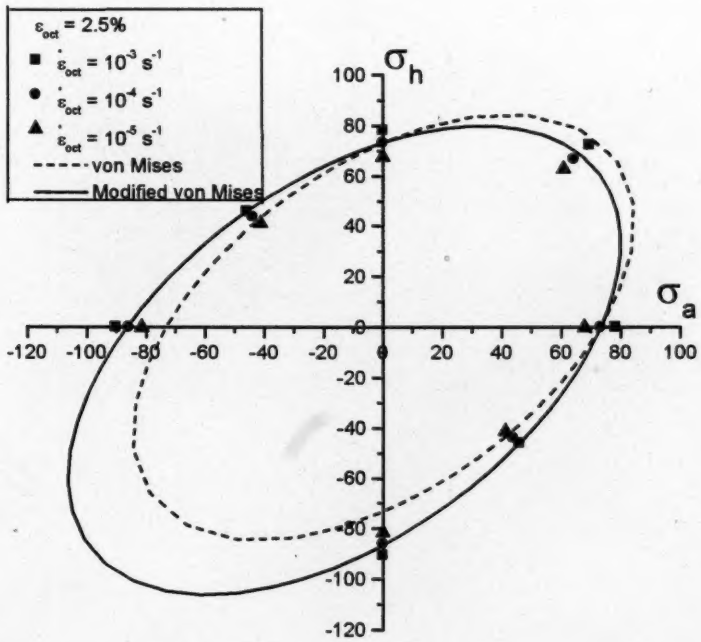

Fig.3.6 Stress envelopes at three octahedral shear strain rates

It is noted that the von Mises ellipse does not fit all test points, particularly in the compressive stress dominated regions. Since the tested epoxy showed a difference between

uniaxial tension and compression, the same set of test points was also compared with an equation developed by Stassi (1969), a modified von Mises equation, for isotropic materials with different tensile and compressive behaviors. The Stassi equation is given by:

$$\frac{1}{2}\left[(\sigma_1-\sigma_2)^2+(\sigma_2-\sigma_3)^2+(\sigma_3-\sigma_1)^2\right]+(R-1)\sigma_0(\sigma_1+\sigma_2+\sigma_3)=R\sigma_0^2 \qquad (3.3)$$

In the above, the first part represents the von Mises stress while the second part accounts for the difference between tensile and compressive behavior and hydrostatic stress effect; σ_1, σ_2 and σ_3 are the three principal stresses of a stress state; σ_0 is the uniaxial tensile 'yield' stress and R is the ratio of compressive-to-tensile 'yield' stress, a possitive value. When R=1, i.e., the uniaxial tensile 'yield' stress is equal to that in compression, no difference between the tensile and compressive behaivor is included, and Eq. (3.3) reduces to the von Mises criterion. For the biaxial stress state, the equation can be simplified as (Hu et al., 2000):

$$\sigma_a^2-\sigma_a\sigma_h+\sigma_h^2+(R-1)\sigma_0(\sigma_a+\sigma_h)=R\sigma_0^2 \qquad (3.4)$$

where σ_0 is the uniaxial tensile stress corresponding to ε_{oct}=2.5% and $\dot{\varepsilon}_{oct}=10^{-4}\ s^{-1}$ and R is the ratio of uniaxial compressive-to-tensile stress for ε_{oct}=2.5% and $\dot{\varepsilon}_{oct}=10^{-4}\ s^{-1}$.

It is noted that the envelope predicted by the Stassi Eq. (3.4) (solid line in Fig. 3.6) has a better fit to the test data than that of the von Mises ellipse. Since the only difference between the Stassi and the von Mises equations is a hydrostatic stress term introduced through the R ratio, hydrostatic stress effect is confirmed.

3.3.2 Stress envelope for octahedral shear strain amplitude

The influence of increasing strain magnitude on the stress envelopes was also studied by performing tests at three octahedral shear strain values with the same octahedral shear strain rate of $10^{-4}\ s^{-1}$ (Fig.3.7). The figure shows that the stress envelopes also expand with the increase in octahedral shear strains. These stress envelopes are also compared with the von Mises and Stassi ellipses and a better agreement between Stassi ellipses and test points is observed.

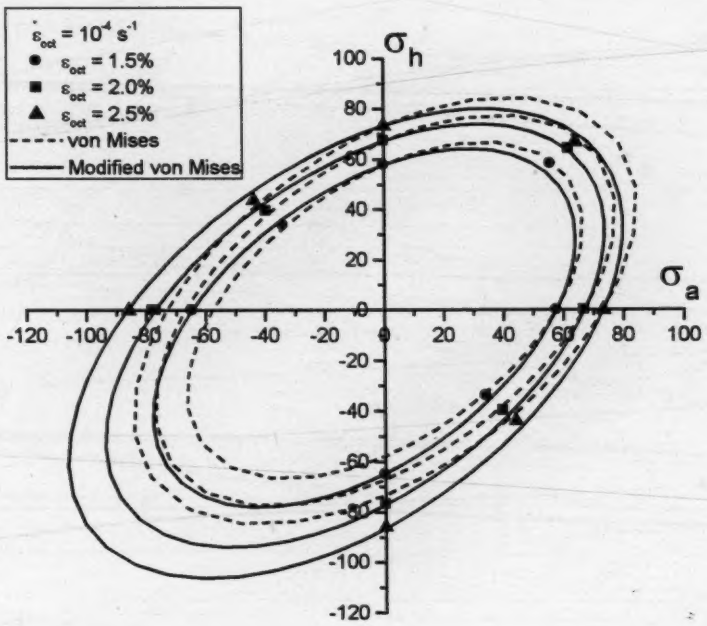

Fig.3.7 Stress envelopes at three different octahedral shear strain values

From the above experimental investigation of biaxial loading, it is seen that the biaxial behavior of the tested epoxy can be described fairly well by the Stassi equation (3.4).

3.4 Loading Path Effect

The axial stress responses for the two loading paths $\overline{OAC}$ and $\overline{OBC}$ (Fig.2.12) at the octahedral shear strain rate of $10^{-5}s^{-1}$ are shown in Fig.3.8. For both strain paths, the axial stress increases with the increase of strain until a strain value of 3.16% is reached. Note that the axial stress versus the axial strain response for the strain path $\overline{OBC}$ is below that of path $\overline{OAC}$. The offset of the path $\overline{OBC}$ stress-strain diagram reflects a cross effect due to the prior torsional loading, see Krempl and Bordonaro (1998). This difference can only be attributed to the presence of a prior shear stress for the path $\overline{OBC}$. Therefore, this figure indicates that the presence of a prior shear stress causes a reduction in the stiffness of the axial stress-strain behavior.

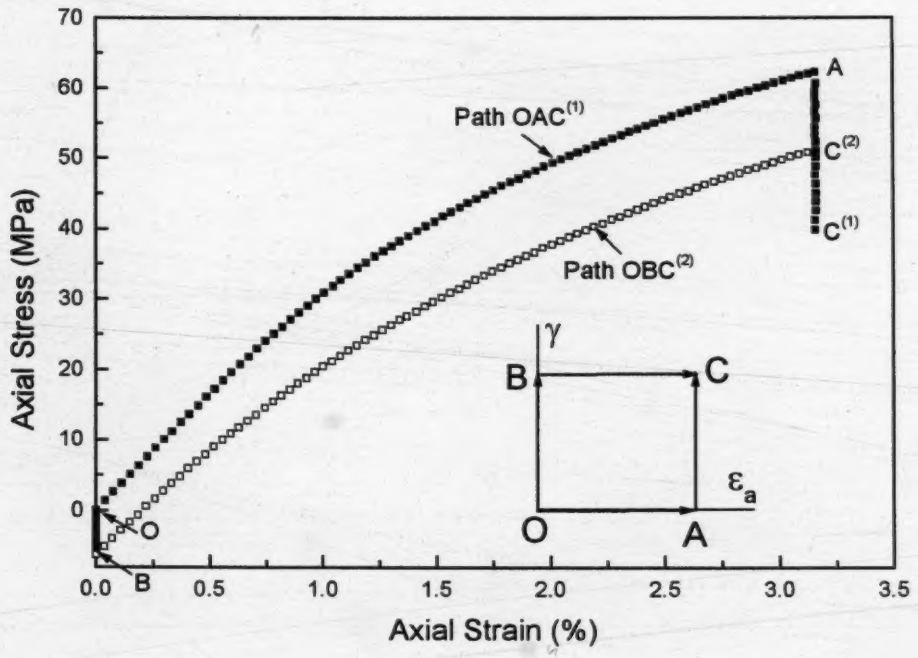

Fig.3.8 Experimental axial stress-strain curves for two different loading paths with an octahedral shear strain rate of $10^{-5}s^{-1}$

The shear stress versus shear strain response for the same strain paths is depicted in Fig.3.9. Again two distinct curves are observed, but the trend is reversed, i.e., the shear stress-strain curve for the path $\overline{OBC}$ is slight higher than that of $\overline{OAC}$ due to the presence of a prior axial stress in the latter path. Therefore, the existence of a prior axial stress also causes a reduction in the stiffness of the shear stress-strain curve.

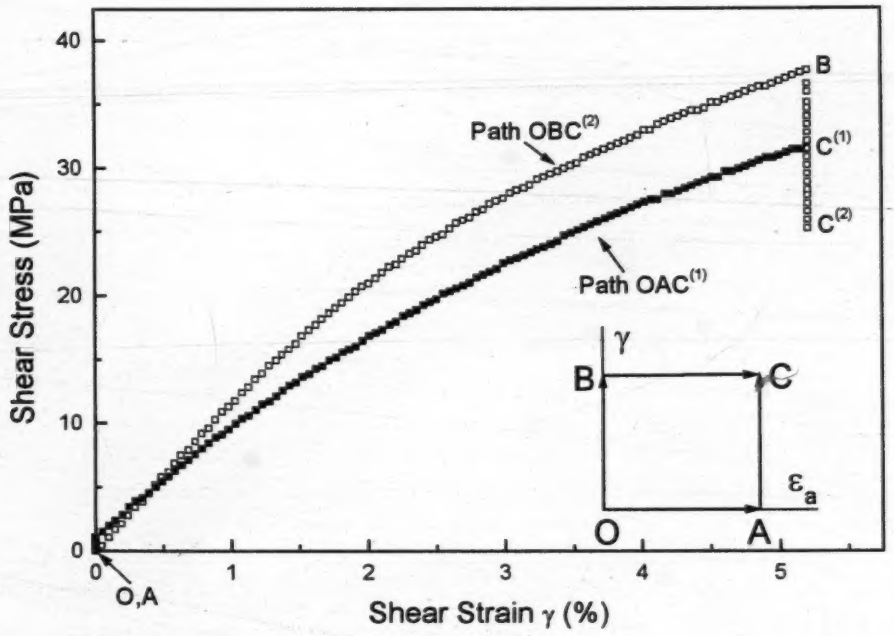

Fig.3.9 Experimental shear stress-strain curves for two different loading paths with an octahedral shear strain rate of $10^{-5}s^{-1}$

With reference to Fig.3.8 and path $\overline{OAC}$, the axial stress drops from point A to the lowest point C by about 22.76 MPa when the shear stress, path AC, is applied. The corresponding drop in the shear stress from point B to lowest point C in Fig.3.9 is about 12.61 MPa. In Figs 3.8 and 3.9 there are two points labeled C. They refer to the axial (shear) stresses

reached by the different strain paths. The axial and shear stress drops observed in Figs 3.8 and 3.9 are partly due to the stress relaxation while the axial or shear strains are kept constant and partly due to the interaction of the increase in shear or axial stresses as shown by Krempl and Bordonaro (1998).

From the above loading schemes, it is seen that the only difference between the loading paths $\overline{OAC}$ and $\overline{OBC}$ is that of the loading sequences. In order to study the non-proportional loading behavior, the stress response from loading path $\overline{OAC}$ or $\overline{OBC}$ has to be compared with that of a proportional one, i.e., path $\overline{OC}$. However, it is impossible to reach point C along both the proportional path $\overline{OC}$ and non-proportional path $\overline{OAC}$ or $\overline{OBC}$ at the same time and with the same strain rate, therefore, the stress response from path $\overline{OBC}$ is compared with that of path $\overline{OC}$ with two strain rates as shown in Fig.3.10.

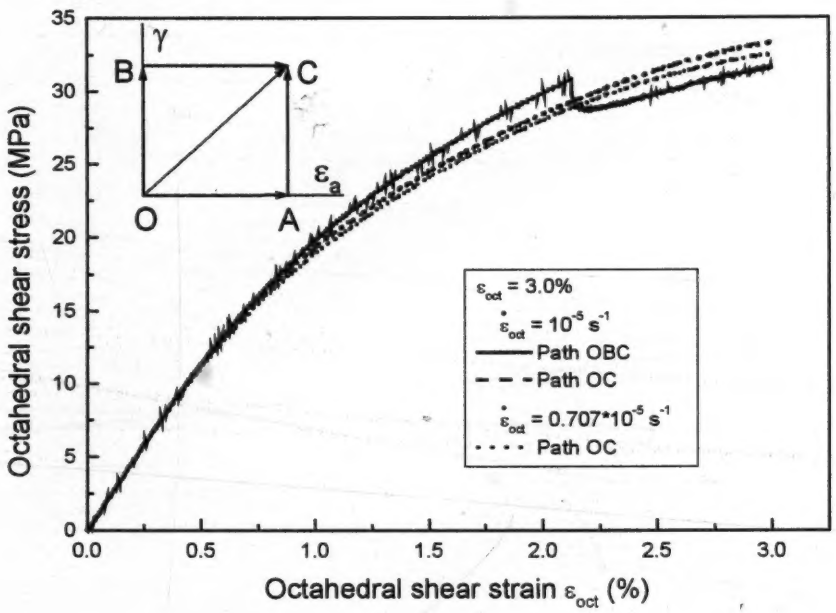

Fig.3.10 Octahedral shear stress – strain curves for three different loading cases

In Fig.3.10, two strain rates for path $\overline{OC}$ were chosen. In one test, the octahedral shear strain rate was $10^{-5}s^{-1}$, the same rate as that of path $\overline{OBC}$. The second test had an octahedral shear strain rate of $0.707\times10^{-5}s^{-1}$, smaller than that of path $\overline{OBC}$, but reaching point C at the same time in two loading paths. It is noted from Fig.3.10 that the final stress states at point C of the three curves are different from each other, showing both rate and path-dependent mechanical behavior.

3.5 Failure Behavior

In the present study, an attempt was made to determine the multiaxial failure behavior of the EPON 826 epoxy and the relative importance of deviatoric and hydrostatic stresses in the failure behavior of the epoxy. Rate effect on the failure behavior was also studied by loading specimens to failure at different octahedral shear strain rates.

Figure 3.11 shows the tensile stress-strain curves up to failure at three different octahedral shear strain rates of $10^{-3}\ s^{-1}$, $10^{-4}\ s^{-1}$ and $10^{-5}\ s^{-1}$. All these three stress-strain curves show similar patterns to failure with a highly nonlinear response prior to failure. The failure mode is a brittle fracture. An increase in the strain rate results in an increase of the failure stress from 72.3MPa to 81.0MPa. However, the failure strains decrease (c.f. Fig.3.11).

Compared to the aforementioned tensile failure, the failure behavior for uniaxial compressive tests was more complex. In Fig.3.12, curve (a) represents a uniaxial compressive test with a stress rate of 0.5MPa/s (Note that in this figure, the sign of compressive stress and strain is changed to a positive one). This test was conducted using a

solid cylinder as shown in the inset of the figure. The diameter and height of the solid cylinders were 12.7mm and 25.4mm, respectively (in conformity with ASTM D 695-96).

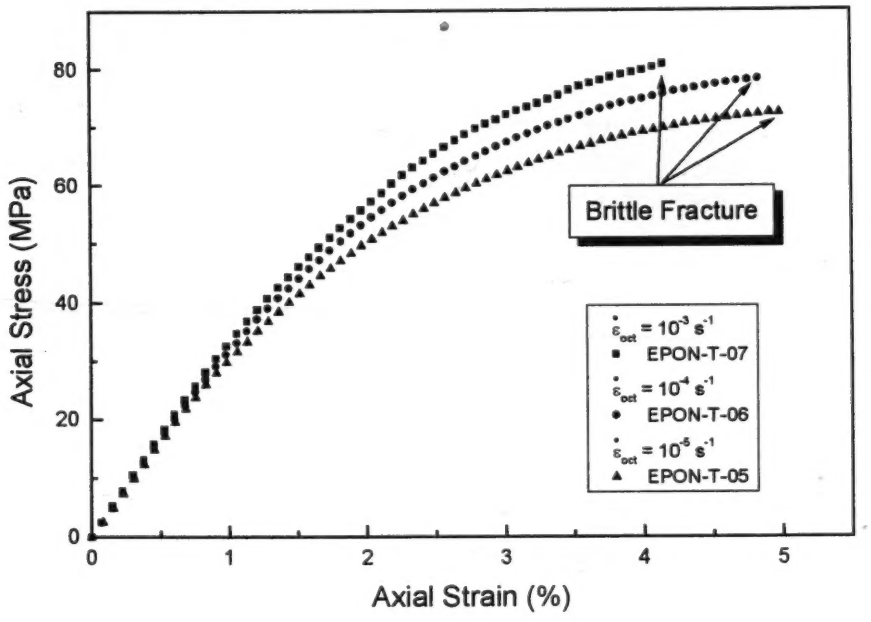

Fig.3.11 Tensile stress-strain curves to failure at three different octahedral shear strain rates $10^{-3}\ s^{-1}$, $10^{-4}\ s^{-1}$ and $10^{-5}\ s^{-1}$

The compressive stress-strain curve begins with a steep linear behavior and then gradually changes to nonlinear one with the modulus decreasing continuously up to about 30% strain whereupon the stiffness increases again. Since the final strain is as high as 40%, it is more appropriate to use the true stress - true strain representation rather than the engineering ones. Here, the true strain, e, is defined as $e = \ln(l/l_0)$, where l is the actual length at any time and l_0 is the initial length of the tested specimen. The relation between the true strain, e, and the engineering strain, ε_a, is as follow:

$$e = \ln \frac{l}{l_0} = \ln \frac{l_0 + \Delta l}{l_0} = \ln(1 + \varepsilon_a) \tag{3.5}$$

where Δl is the change in total length. The true stress, σ, is obtained by dividing the load L by the actual cross-section area A at any time, in constrast to the original cross-section A_0 used in the calculation of the engineering strain σ_a. If constant volume during deformation is assumed, then the true stress σ can be related to the engineering stress σ_a and engineering strain ε_a by the following relationship,

$$\sigma = \frac{L}{A} = \frac{L}{A_0}\frac{l}{l_0} = \frac{L}{A_0}\frac{l_0 + \Delta l}{l_0} = \sigma_a(1 + \varepsilon_a) \tag{3.6}$$

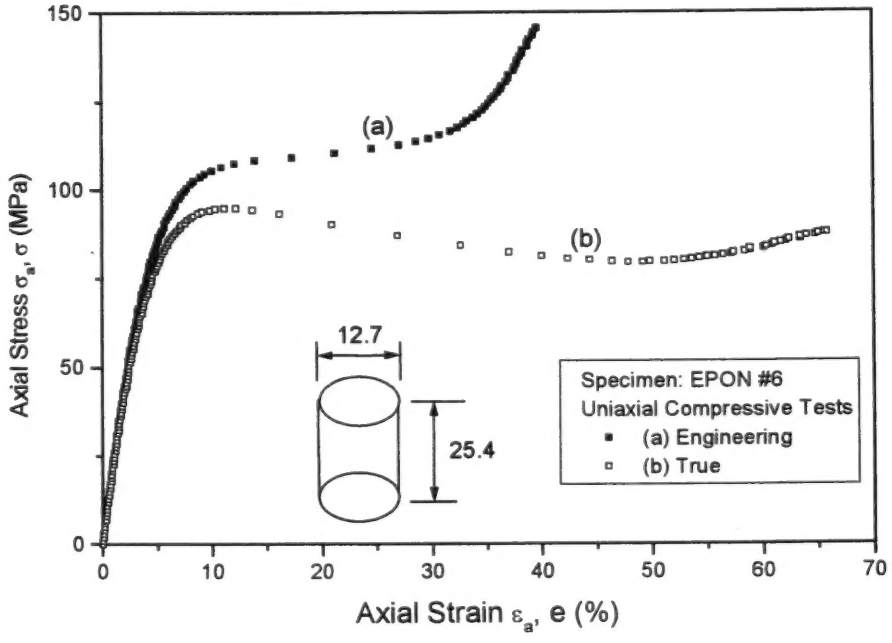

Fig.3.12 Compressive stress-strain curves to failure at stress rate of 0.5MPa/s: (a) Engineering representation; (b) true representation

The corresponding true stress - true strain curve is shown in Fig.3.12(b). As to be expected the two stress - strain curves are similar up to 5% strain. Following this the true stress - true strain curve is below that of the engineering one and a strain softening is observed. Finally at large strains, a slight strain-hardening occurs.

Note that the maximum stress difference between the two sets of curves in Fig. 3.12 at 5% strain is 7.6%. Therefore, in tests with the maximum strains less than 5%, engineering stresses and strains are used in the representation of the mechanical properties of the epoxy resin.

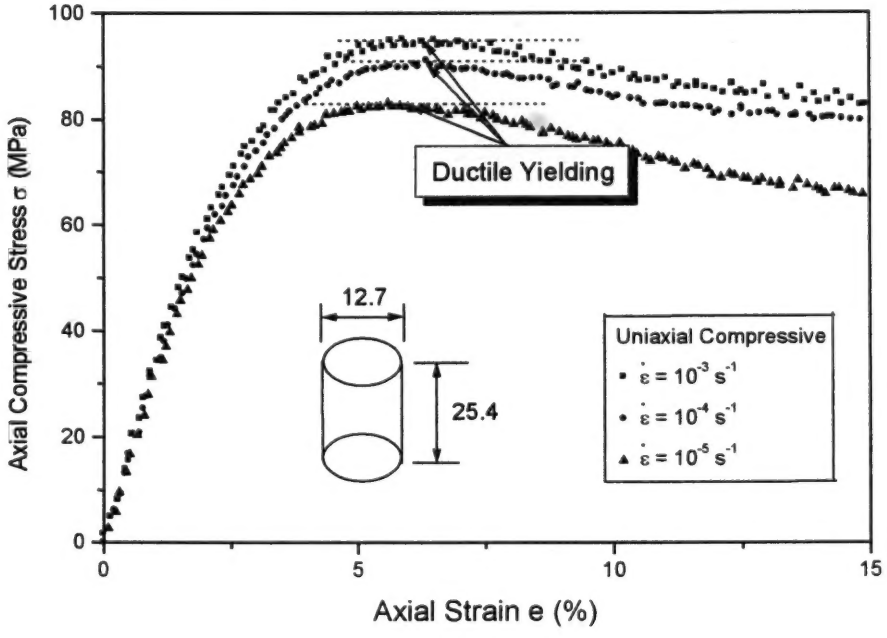

Fig.3.13 Compressive stress-strain curves to failure at three different octahedral shear strain rates $10^{-3}\ s^{-1}$, $10^{-4}\ s^{-1}$ and $10^{-5}\ s^{-1}$

Figure 3.13 depicts the uniaxial compressive stress-strain behavior at three different strain rates. These tests were conducted at constant displacement rate control. Compared with the tensile failure curves as shown in Fig.3.11, the compressive tests demonstrated higher failure stresses and higher failure strains. Another difference is the failure mode: for compressive tests, the specimens show ductile failure behavior with a peak stress at a strain around 8%.

The pure shear stress-strain curves to failure at three different octahedral shear strain rates are shown in Fig.3.14. These curves reach a maximum stress prior to decreasing to a lower failure stress and show a ductile yield behavior. The failure stress increases with the increase of the applied strain rate.

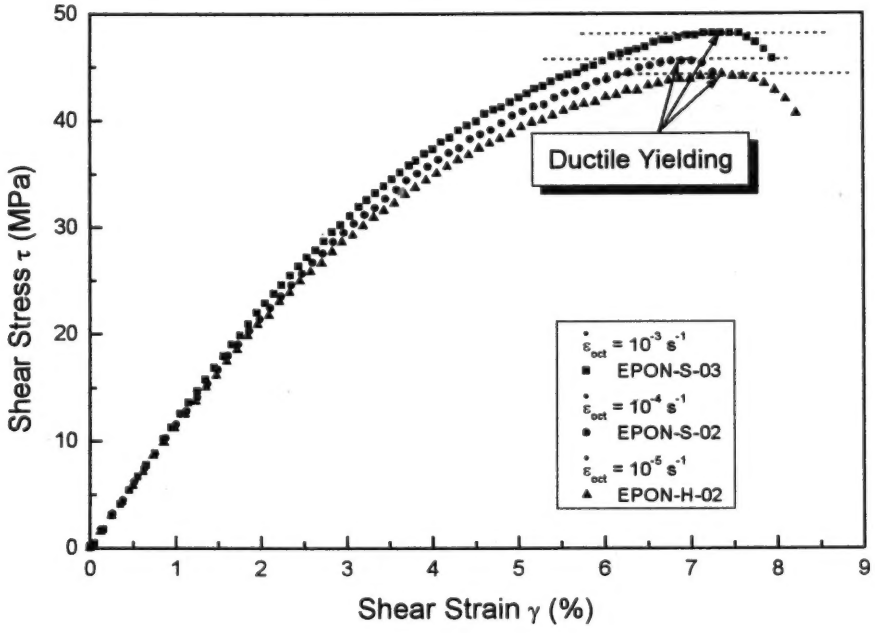

Fig.3.14 Shear stress-strain curves to failure at three different octahedral shear strain rates $10^{-3}\ s^{-1}$, $10^{-4}\ s^{-1}$ and $10^{-5}\ s^{-1}$

The equibiaxial stress – strain curves to failure at an octahedral shear strain rate of $10^{-3}\ s^{-1}$ are shown in Fig.3.15. It is obvious that these typical biaxial stress-strain curves have some common features as the uniaxial curves shown in Fig.3.11. For example, linear behavior can be distinguished at low stress levels in both axial and hoop stress-strain curves. With the increased strain, the rate of increase in stress decreases in both loading directions. The axial and hoop stress – strain curves are slightly different. The equibiaxial tests also failed in a brittle mode.

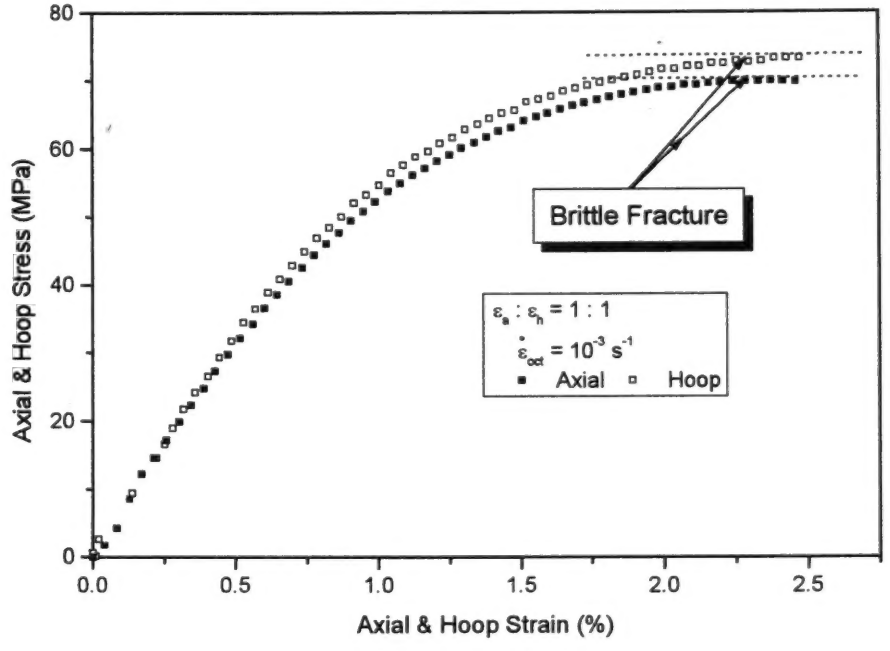

Fig.3.15 Equibiaxial stress-strain curves to failure at an octahedral shear strain rate of $10^{-3}\ s^{-1}$

A comparison of Figs 3.11-15 indicates that the failure modes are different: the failure mode for uniaxial tensile and equibiaxial tensile tests is brittle fracture while for that of

pure shear and uniaxial compressive tests it is ductile yielding. Two different failure behaviors were also observed in other polymers and they are explained in terms of the hydrostatic stress effect (Kody and Lesser, 1997). A schematic of the influence of hydrostatic stress on the failure modes of this epoxy is shown in Fig.3.16. There is a ductile-to-brittle transition between the uniaxial tensile and pure shear stress states.

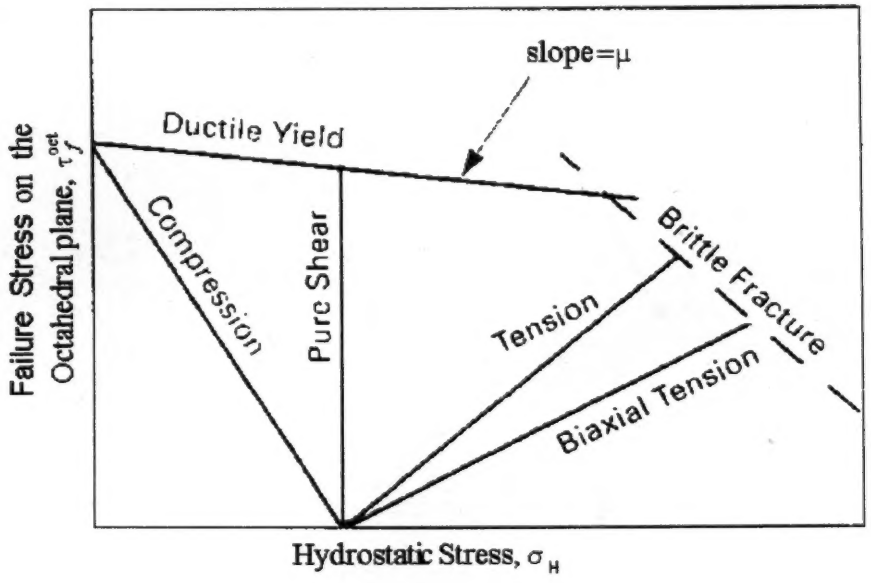

Fig.3.16 A schematic of hydrostatic stress effect on failure modes

(Modified from Kody and Lesser, 1997)

If the material follows a modified von Mises or modified Tresca type behavior, then the shear failure stress, τ_f^{oct}, will plot on a straight line. It can be seen from the following modified von Mises or Tresca equation (Kody and Lesser, 1997, Asp et al., 1996):

$$\tau_y^{oct} = \tau_{y0}^{oct} - \mu\sigma_m \tag{3.7}$$

where τ_{y0}^{oct} is the shear failure stress in the absence of any overall hydrostatic stress and μ is commonly referred to as the coefficient of internal friction, representing the slope of the

line as shown in Fig.3.16. If σ_m has no effect on τ_f^{oct}, then μ is equal to zero and the straight line is horizontal, the failure is then said to follow a typical von Mises or Tresca behavior.

The quantitative relationship between the failure stress and the hydrostatic stress is shown in Fig.3.17. In this figure, the experimental failure data are compared with the modified Tresca criterion (Eq. (3.7)) (only the Tresca failure envelope for $10^{-4}\ s^{-1}$ is shown in this figure).

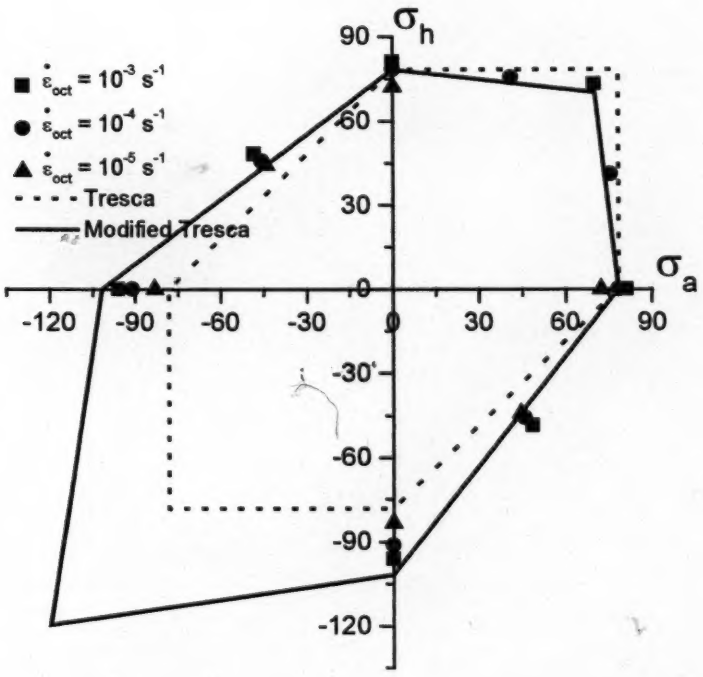

Fig.3.17 Comparison of experimental data with modified Tresca criterion

Since no data could be obtained for compressive 'yield' stress due to buckling of the tubular specimens, internal friction coefficient μ is obtained by the best fit of the

experimental failure data. The value of μ for the modified Tresca is 0.3. It is observed that the modified Tresca criterion fits the experimental data fairly well. Since no experimental data was available in the third quadrant to confirm the criterion, this is considered to be a tentative conclusion.

3.6 Concluding Remarks

From the results presented in this experimental investigation, the following conclusions are drawn for the EPON 826 epoxy:

- EPON 826 shows a strong nonlinear viscoelastic behavior. Its deformation behavior is influenced by loading rates. It has high modulus, high stress to failure, and large strain to failure, demonstrating excellent strengths and toughness.
- Hydrostatic pressure does not have significant effect on the deformation behavior of this epoxy resin at pressure levels up to 17.24 MPa. However, the influence of hydrostatic component of stress was observed in multiaxial tests at higher hydrostatic stress levels. The effect can be described by a Stassi equation.
- Path-dependent behavior is observed for this epoxy manifested in axial-shear stress interaction, and lower stiffness in non-proportional loading paths compared to that of proportional ones.
- This epoxy failed in two different modes: brittle fracture or ductile yielding. The difference in failure modes can be explained by hydrostatic stress effect. The failure stress envelope can be represented by a modified Tresca criterion.

Bibliography

1. Hu, Y., Xia, Z. and Ellyin, F., 2000, "Mechanical Behaviour of an Epoxy Resin under Multiaxial Loadings, Part II: Comparison of Viscoelastic Constitutive Model Predictions", Polymers and Polymer Composites, 8, 157-166.
2. Krempl, E. and Bordonaro, C.M., 1998, Non-proportional Loading of Nylon 66 at Room Temperature, International Journal of Plasticity, 14, 245-258.
3. Krishnaswamy, P., Tuttle, M.E. and Emery, A.F., 1992, Finite Element Modeling of the Time-Dependent Behavior of Nonlinear Ductile Polymers, Polymer Engineering and Science, 32, 1086-1096.
4. Stassi-D'Alia, F., 1969, Limiting Conditions of Yielding for Anisotropic Materials, Meccanica, 4, 349-364.

Chapter 4

Mechanical Behavior of ColdCure Epoxy

The mechanical behavior of ColdCure epoxy was studied by similar tests to those for EPON 826, and the test results will be presented in this chapter. These tests can also be divided into two groups: one group was used to investigate the deformation behavior before failure. They include experiments on viscoelastic behavior, hydrostatic stress effect, multiaxial behavior and loading path effect. The experiments on the failure behavior of the epoxy were included in the second group which provide such information as failure strengths and failure modes. One can get an insight into the mechanical behavior of different epoxy systems through the comparison of the experimental results with the same experimental procedure but different epoxy systems. The experimental results for this epoxy can also be used for the development of constitutive models of polymers or further verification of the constitutive models from other polymeric systems.

4.1 Viscoelastic Behavior

4.1.1 Uniaxial tensile creep

For the uniaxial creep tests of ColdCure epoxy, thirteen different stress levels ranging from 2.8 MPa to 23.4 MPa were tested and the corresponding strain responses are shown in Fig. 4.1. It is seen that the applied stress levels for this epoxy are much lower than that of the EPON 826 epoxy. Although the applied stress values and the resulted creep strain values are much different, the two epoxies have the similar creep deformation behavior, e.g., the creep strains at low stress levels are relatively small but increase appreciably at higher

stress levels. Creep strains increase continuously with a decreasing rate at stress levels up to 20.4 MPa. For this epoxy, the creep strains experience all three stages of decreasing rate, nearly constant rate and increasing rate at 23.4 MPa, indicating certain damage has been developed in the specimen.

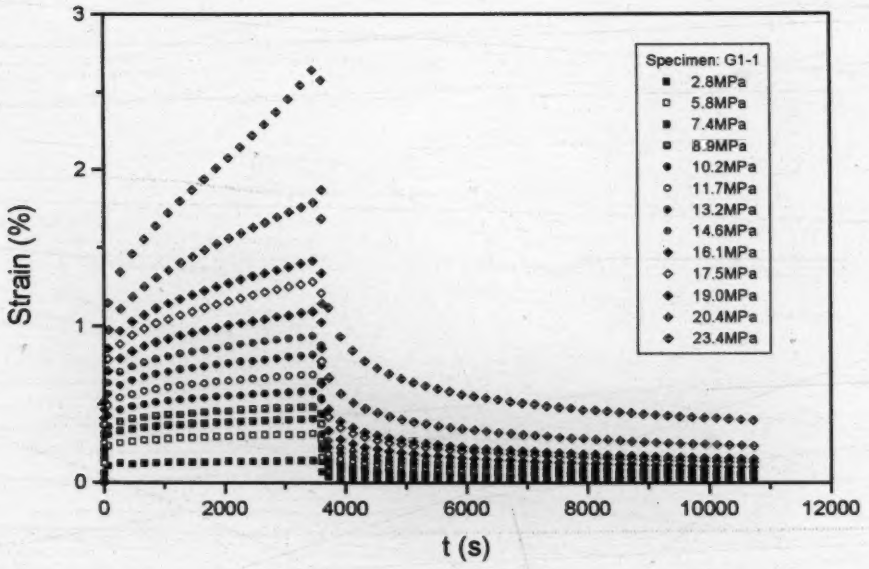

Fig. 4.1 Creep and recovery curves at different stress levels

Upon the removal of the applied stress after one-hour creep, the strain curves up to two hours were also recorded during the recovery process as shown in Figs. 4.1 and 4.2. It can be seen that following the stress removal, the creep strains recover also at a continuously decreasing rate. Both Figs. 4.1 and 4.2 show that the mechanical behavior of the tested epoxy is also time-dependent.

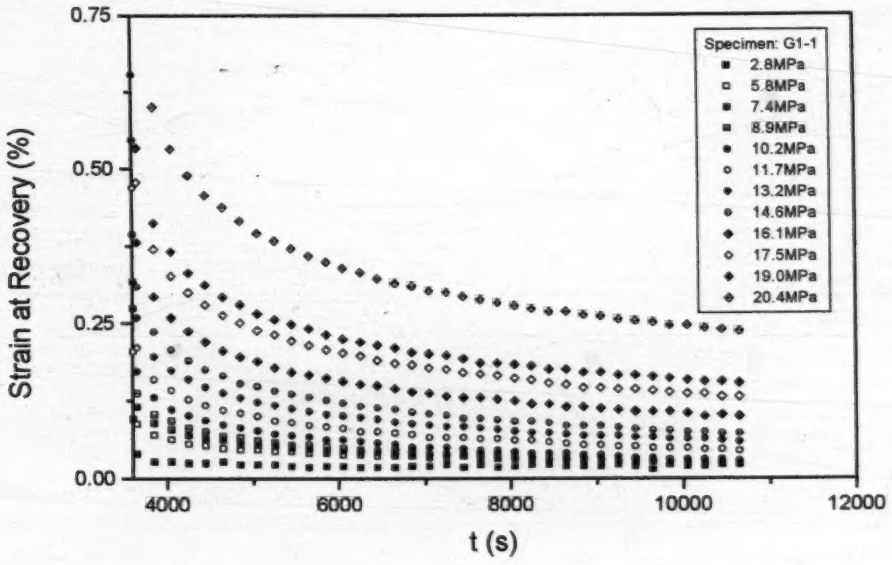

Fig. 4.2 Strain curves at recovery at different stress levels

Similar strain recovery behavior was observed for the ColdCure epoxy with that of the EPON 826, e.g., there were no residual strains at low stress levels and small ones at high stress levels after 10–hour recovery. For tests at the stress level of 20.4 MPa, the residual strain after 10 hours is 0.0733% which is small compared to the maximum creep strain of 1.81% at this stress level. Therefore, a viscoelastic characteristic is confirmed for the ColdCure epoxy. The curve for the highest stress level of 23.4MPa is not shown from here on because the creep part of the creep-recovery curve indicates that the specimen had already been damaged before recovery started.

Although the creep strains for this epoxy are much smaller than that of the EPON 826 epoxy, the residual strains at recovery stage are much bigger. For example, the residual

strain after two hours of recovery following the creep test at the stress level of 20.4 MPa is 0.235%, compared with 0.148% at 63.54MPa for the EPON 826 epoxy.

From Fig.4.3 it can be seen that no two creep compliance curves collapse on to one for the shown applied stress values (the creep compliance curve for the applied stress level of 2.8 MPa is not shown in the above figure because the creep compliance for this stress value fluctuates too much due to the small strain values). At least for the stress levels higher than 5.8 MPa, the creep compliance curves separate from each other and they are dependent on the current applied stress level, therefore, the epoxy behavior becomes nonlinear from the very beginning, which is different from that of the EPON 826 epoxy. A comparison also shows that the epoxy has a higher creep compliance than that of the EPON 826 epoxy.

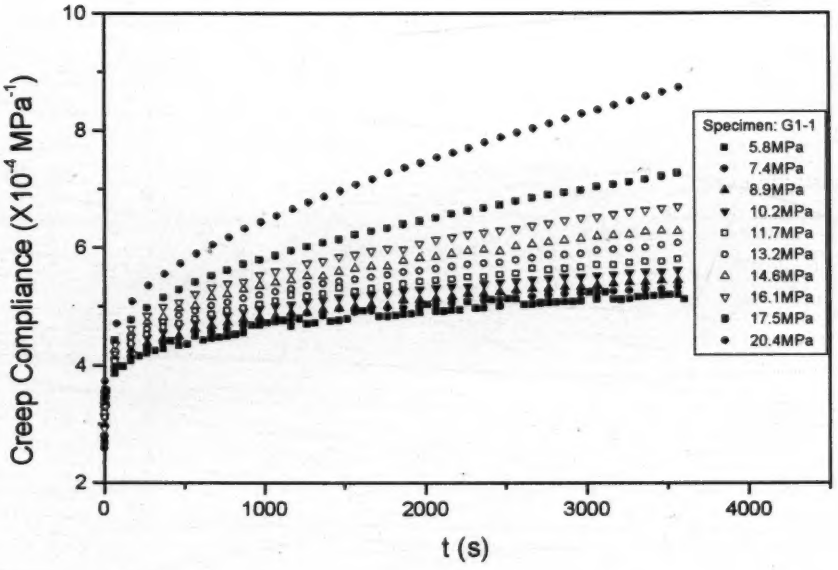

Fig.4.3 Compliance curves at different stress levels for ColdCure epoxy

The series of creep-recovery tests show that ColdCure epoxy has a strong nonlinear viscoelastic behavior, smaller creep strains and higher creep compliances than those of the EPON 826 epoxy. It also exhibits a slower strain recovery behavior. This set of creep and recovery curves will be used to calibrate the material constants and functions for the constitutive models in Chapter 5.

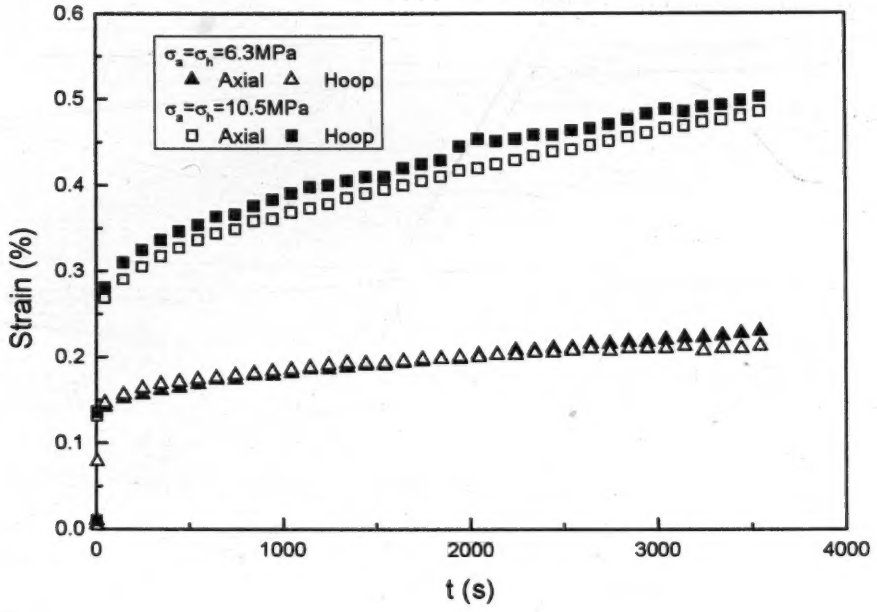

Fig. 4.4 Equibiaxial creep response for two stress levels

4.1.2 Biaxial creep

Figure 4.4 shows the equibiaxial creep behavior at two stress levels of 6.3MPa and 10.5MPa, indicating a similar characteristic to that of the uniaxial tests. It can be seen that the creep strain curves in the axial and hoop directions are close to each other, especially at the low stress levels. This indicates that the epoxy has an isotropic property with respect to the principal directions. For the higher stress level of 10.5MPa, the axial and hoop strain

deformations are a little bit different because the applied axial and hoop stresses were not exactly the same.

4.2 Hydrostatic Stress Effect

Two sets of tests were performed to study the hydrostatic stress effect on the deformation behavior of this epoxy resin. In the first set, the shear strain was loaded and unloaded monotonically at constant shear strain rates of $2\times10^{-4}\ s^{-1}$ and $2\times10^{-5}\ s^{-1}$. In the second set, a step shear stress of 15 MPa was applied and then held constant for 1 hour. For each loading set, two tests, one with a superimposed hydrostatic pressure of 17.24 MPa, and the other without superimposed hydrostatic pressure, were done and their stress responses were compared.

4.2.1 Shear stress-strain behavior under hydrostatic pressure

Figure 4.5 shows two shear loading and unloading stress-strain curves, one under a superimposed hydrostatic pressure of 17.24 MPa, the other without a superimposed hydrostatic pressure. Both tests were performed under shear strain control with the same shear strain rate of $2\times10^{-4}\ s^{-1}$. It can be seen that the test under a superimposed hydrostatic pressure has a higher shear stress response.

The hydrostatic pressure effect was further checked by another set of tests. The only difference between this set of tests and the previous one, is that the shear strain rate for this set of tests is an order of magnitude lower than the previous ones, i.e., $2\times10^{-5}\ s^{-1}$. It can be seen from Fig. 4.6 that two different curves are obtained and the difference between these two curves are more significant than that at a shear strain rate of $2\times10^{-4}\ s^{-1}$.

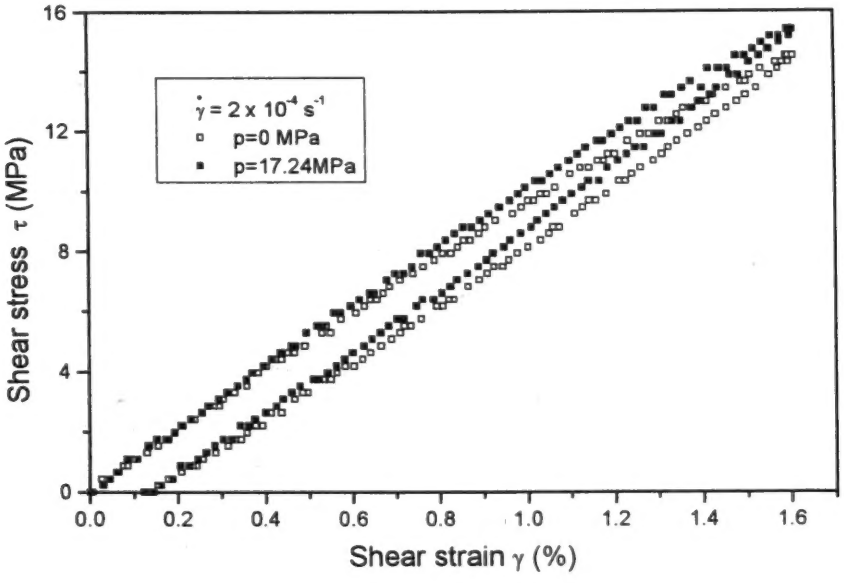

Fig.4.5 Shear loading and unloading stress-strain curves for $\dot{\gamma} = 2 \times 10^{-4}\ s^{-1}$ with or without a superimposed hydrostatic pressure of 17.24MPa

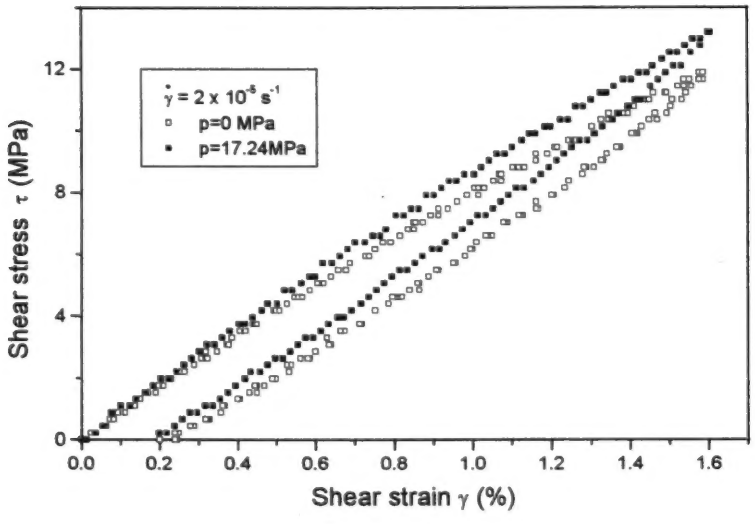

Fig. 4.6 Shear loading and unloading stress-strain curves for $\dot{\gamma} = 2 \times 10^{-5}\ s^{-1}$ with or without a superposed hydrostatic pressure of 17.24MPa

4.2.2 Shear creep under hydrostatic pressure

Alternative tests to study the hydrostatic stress effect are creep deformations under constant shear stresses with or without a superimposed hydrostatic pressure. A shear stress of 15 MPa was applied and then kept constant for 1 hour (Fig.4.7). The applied shear stress is about 64% failure stress of the ColdCure epoxy. At this stress level, it is considered that no damage was brought in during the 1 hour creep period and two creep tests could be done on the same specimen.

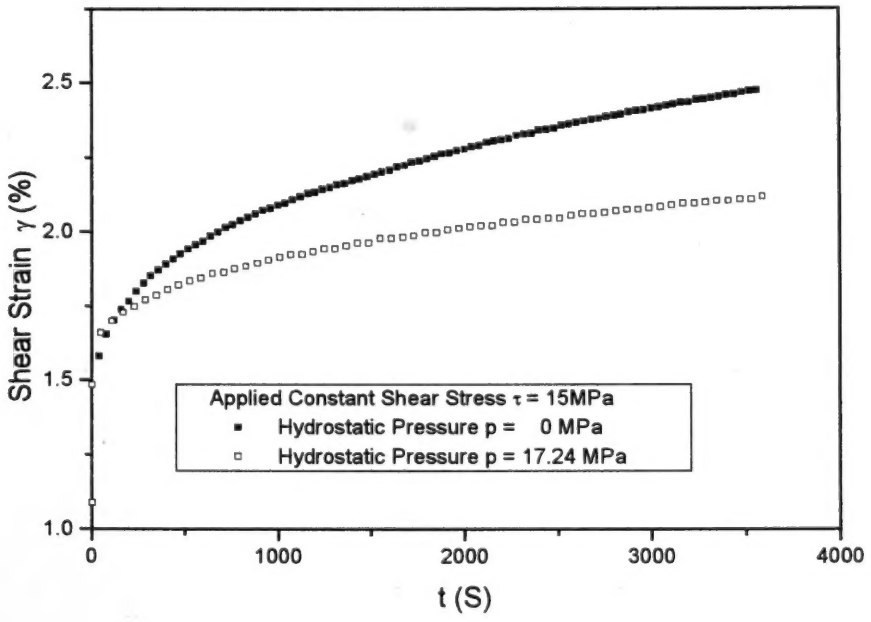

Fig.4.7 Shear creep deformations with or without a superimposed hydrostatic pressure of 17.24MPa

As it is seen from Fig.4.7, the difference between the two creep curves is quite noticeable. The creep curve with a superimposed hydrostatic pressure has a lower shear deformation, i.e., a shear stress with a superimposed hydrostatic pressure retards the creep deformation.

Figures 4.5 – 4.7 show that hydrostatic stress significantly influences the deformation behavior of the ColdCure epoxy, contrast with that of EPON 826 epoxy.

4.3 Axial–Shear Interaction

In plasticity, axial–torsional tests are often used to study the interaction between normal and shear stress (strain) components. These tests are employed to discriminate among different constitutive models of plastic deformation (Krempl and Bordonaro, 1998). Here the axial–shear interaction effect of the ColdCure epoxy was investigated by two series of tests (see Table 4.1). One set is for the axial stress effect on shear creep (Series I, Table 4.1) and another one is for the shear stress effect on axial creep (Series II, Table 4.1).

Table 4.1 The applied stress states for creep tests

Series No.	Case No.	Shear Stress (MPa)	Axial Stress (MPa)
I	1	10	14
	2	10	-14
II	1	10	14
	2	0	14

4.3.1 Axial stress effect on shear creep

Shear creep responses at 2 different combinations of axial and shear stresses (see Table 4.1, series I) are shown in Fig. 4.8. This figure illustrates the influence of the axial (tensile or compressive) stress on the shear creep behavior of the epoxy resin. It is clear that superimposed axial tension and compression have a readily discernible and different effect on the creep behavior in shear. A shear stress with a superimposed axial tensile stress, case 1, exhibits higher creep deformation than that with the same shear stress but a

superimposed axial compressive stress, case 2. It should be pointed out that two specimens were tested for this purpose. The second specimen showed the same trend, therefore, only the curves from the first one are shown here.

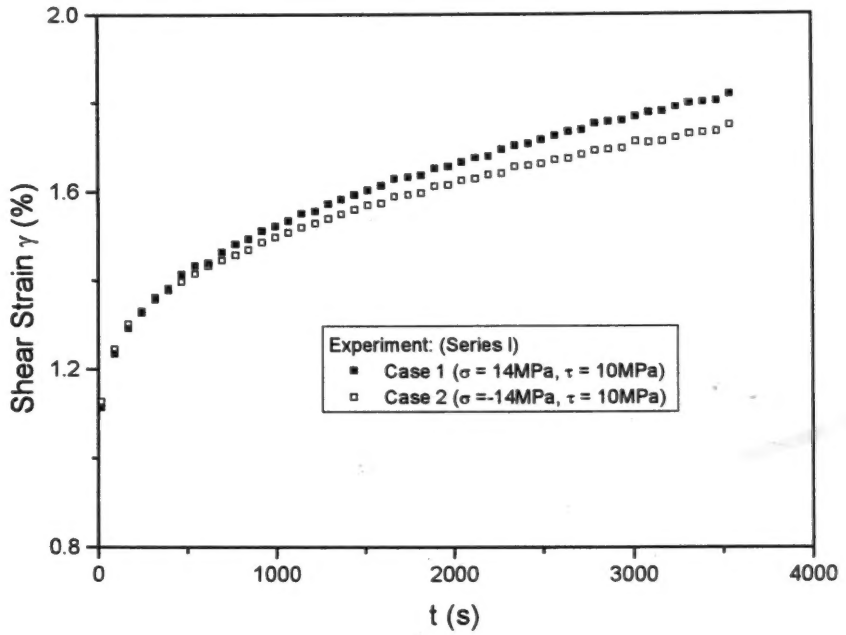

Fig.4.8 Effect of axial stress on the shear creep for two cases:

Case 1: $\tau = 10\,\text{MPa}$, $\sigma_a = 14\,\text{MPa}$; Case 2: $\tau = 10\,\text{MPa}$, $\sigma_a = -14\,\text{MPa}$

The above results can also be explained in terms of the hydrostatic stress states. In the case of a shear stress with a superimposed axial tensile stress, the hydrostatic stress is positive. When the axial stress is compressive, the hydrostatic stress is negative. Therefore, this test further confirms that a superimposed positive hydrostatic stress accelerates the shear creep deformation whereas a superimposed negative hydrostatic stress retards the shear creep deformation.

4.3.2 shear stress effect on axial creep

Figure 4.9 depicts the influence of a superimposed shear stress on the axial tensile creep behavior. It can be seen that a superimposed shear stress has a significant effect on the axial creep response. A superimposed shear stress accelerates the creep deformation. This can also be attributed to the increase in the second stress invariant. A superimposed shear stress increases the equivalent (or octahedral shear) stress, and the creep deformation accelerates under a higher equivalent (or octahedral shear) stress.

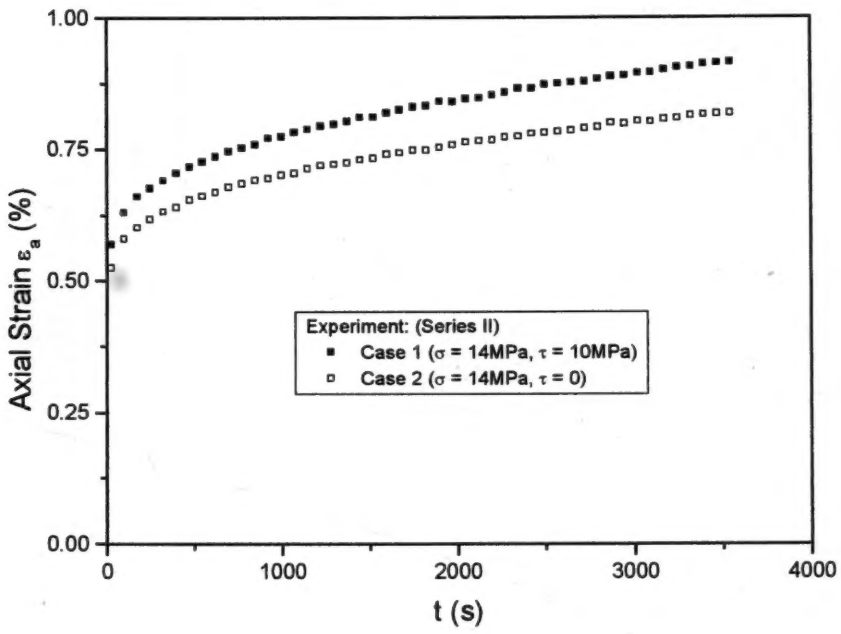

Fig.4.9 Effect of shear stress on the axial creep for two cases:

Case 1: $\tau = 10\,\text{MPa}$, $\sigma_a = 14\,\text{MPa}$; Case 2: $\tau = 0$, $\sigma_a = 14\,\text{MPa}$

4.4 Multiaxial Behavior

For ColdCure epoxy, two specimens were used to obtain the entire stress envelope for a specified combination of ε_{oct} and $\dot{\varepsilon}_{oct}$. The paths from 1 to 12 have tensile hoop stresses

and are under internal pressure control, i.e., the tensile hoop stresses are produced by increasing internal pressure while keeping external pressure constant. The remaining paths 13 to 24 have compressive hoop stresses and are under external pressure control. Two specimens were employed, one for the paths 1 to 12 and the other for the remaining paths. After each half circle, the first path (starting path) is repeated to ensure that the test procedure did not induce damage to the specimen.

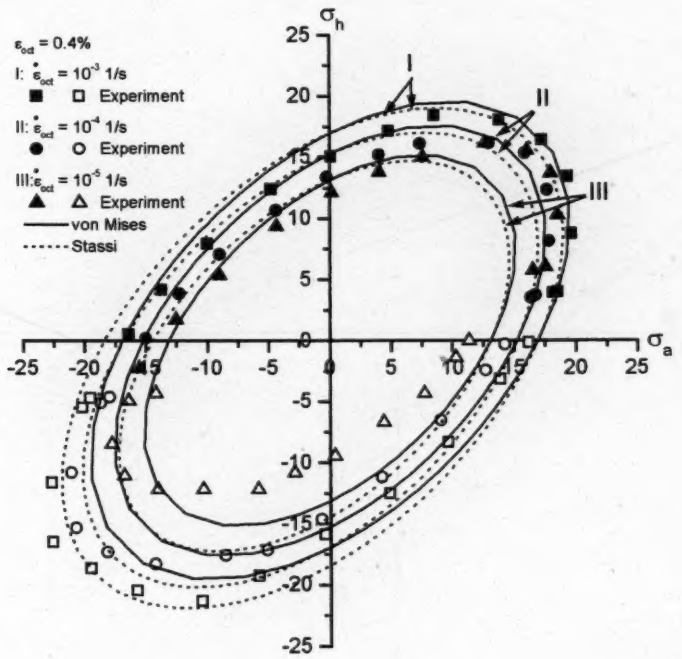

Fig.4.10 Stress envelopes at different octahedral shear strain rates

4.4.1 Stress envelope for the same octahedral shear strain

The stress envelopes for a fixed octahedral shear strain of ε_{oct}=0.4% at three different strain rates of $10^{-3}\ s^{-1}$, $10^{-4}\ s^{-1}$, and $10^{-5}\ s^{-1}$ are depicted in Fig.4.10. Different octahedral shear strain rates were used to study the rate effect. From this figure, it can be

seen that the stress envelopes expand with the increasing octahedral strain rates. The biaxial tensile stresses are different from those of the compressive stresses. The stress envelopes tend to enlarge at the third quadrant.

The stress envelope for ε_{oct}=0.8% at an octahedral shear strain rate of $10^{-4}\ s^{-1}$ is shown in Fig.4.11. Also included in the figure, for the sake of comparison, is the stress envelope for ε_{oct}=0.4% for the same octahedral shear strain rate. An increase in the octahedral shear strain from 0.4% to 0.8% results in not only the stress envelope expanding, but also in changing its shape. It would appear that the stress envelope for ε_{oct}=0.8% rotates around the origin, in comparison to that of ε_{oct}=0.4%.

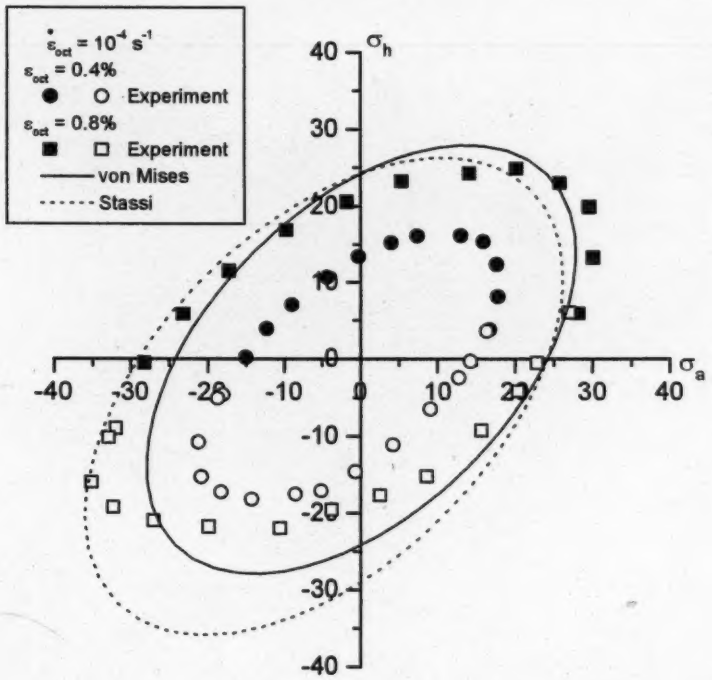

Fig.4.11 Stress envelope for ε_{oct}=0.8% at an octahedral shear strain rate of $10^{-4}\ s^{-1}$

Figures 4.10 and 4.11 show that the epoxy appears to have a higher stiffness in the third (compressive) quadrant. As σ_a, $\sigma_h < 0$, and hence $\sigma_m < 0$ in this quadrant, a compressive hydrostatic stress, σ_m, seems to increase the stiffness of the polymer. Such a phenomenon was also reported for other polymers, e.g., see Whitney and Andrews (1967) among others.

4.4.2 von Mises equation

Stress envelopes for octahedral shear strains of 0.4% and 0.8% are also compared with the von Mises equation, Eq.(3.2), as shown in Figs. 4.10 and 4.11. Because of the bigger scatter of the experimental data for the ColdCure epoxy, instead of replacing σ_0 with the uniaxial tensile stresses corresponding to ε_{oct}=0.4% and 0.8%, respectively, σ_0 is determined by least square fitting of the Eq. (3.2) with all the experimental data corresponding to ε_{oct}=0.4% and 0.8%, respectively.

In Fig.4.10 the von Mises stress envelopes (solid line) of Eq. (3.2) for the octahedral shear strain of 0.4% at three different octahedral shear strain rates are compared with the experimental data. It is seen that the von Mises equation predicts the experimental points fairly well in the first, second and fourth quadrants. In the third quadrant a significant deviation is observed.

The predicted results for the octahedral shear strain of 0.8% are depicted in Fig.4.11. Again, it is seen that von Mises equation agrees fairly well with the experimental data in most stress states except for data points in the third quadrant.

In the first quadrant, σ_a, $\sigma_h > 0$, consequently $\sigma_m > 0$, while in the third quadrant σ_a, $\sigma_h < 0$ and hence $\sigma_m < 0$; in the second and forth quadrants, one of the stress components σ_a or σ_h is negative, therefore,

$$|\sigma_m|_{1st,3rd} >> |\sigma_m|_{2nd,4th} \tag{4.1}$$

and one would expect a von Mises representation to be in better agreement in the second and forth quadrants than in the other two as shown in Figs. 4.10 and 4.11. This is because von Mises criterion is independent of the hydrostatic stress value. Most biaxial tests use a combination of torsion and axial forces which produces stress states in the second and fourth quadrants of Fig.2.7 (see Fig.4.12, Ellyin, 1997). Note that in the case of pure shear, $\sigma_m = 0$, and thus these types of tests do not contain sufficient hydrostatic stress component to evaluate its effect.

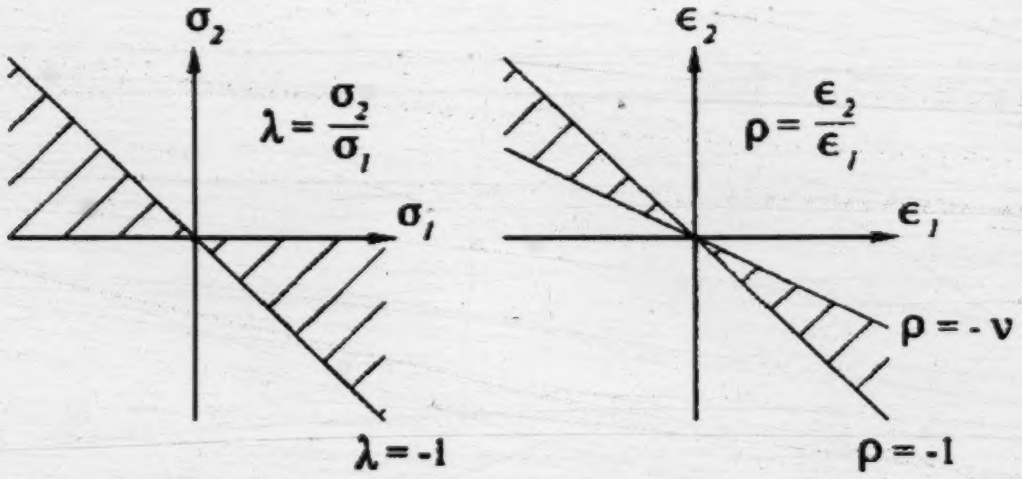

(a) stress-controlled; (b) strain-controlled

Fig.4.12 In-plane biaxiality regimes in terms of the principal stress and strain for axial-torsion, where υ is the Poisson ratio (Courtesy of Wolodko, 1999)

From the above comparison it is also evident that the correlation with von Mises equation would not be satisfactory at regions where the hydrostatic stress is high. Therefore, a number of equations have been proposed to account for the hydrostatic stress effect, see e.g. a review by Ward (1971).

4.4.3 Stassi equation

As discussed in previous section that the hydrostatic stress influences the mechanical behavior of this epoxy resin and this is manifested in the shifting and shape change of the stress envelopes. The von Mises equation does not include the hydrostatic stress effect and, therefore, cannot predict the mechanical behavior where hydrostatic stress is high, e.g., in the first and third quadrants, hence modifications to the von Mises equation have been proposed to account for the hydrostatic stress effect, see e.g. a review by Ward (1983). Because a hydrostatic term is included in Stassi equation, (Eq. (3.3), Stassi, 1967), as introduced in the previous chapter, it is expected to be able to predict the hydrostatic stress effect as well.

Stress envelopes for the octahedral shear strains of 0.4% and 0.8% are compared with equation (3.4) in Figs. 4.10 and 4.11. Fig. 4.10 shows the prediction by the Stassi equation for $\varepsilon_{oct} = 0.4\%$ at three different strain rates. It can be seen that the Stassi equation has a better correlation with the test data, especially in the third quadrant. The Stassi equation is in fair agreement with the test data in most part of the principal stress space for the octahedral shear strain of 0.8% as shown in Fig.4.11. However, neither equation can predict the rotation of the stress envelope about the origin as observed experimentally. This

behavior would require further experimental investigation. The prediction at the third quadrant deviates from the experimental data significantly.

From Figs. 4.10 and 4.11, it can be concluded that the Stassi equation correlates fairly well with the stress envelopes, which were obtained based on a fixed octahedral shear strain value and a specified octahedral shear strain rate.

4.5 Loading Path Effect

In this research, only tests along two non-proportional loading paths $\overline{OAC}$ and $\overline{OBC}$ (Fig.2.12) were conducted to study the loading path effect for this epoxy resin. Strain control mode was utilized for this purpose.

4.5.1 Strain-controlled tests

The loading scheme for non-proportional strain-controlled tests is shown in Fig.2.12. The axial and shear strain values for points A and B used in these tests are 0.742% and 1.6%, respectively, which corresponds to an octahedral shear strain values of 0.49% and 0.653%. The octahedral shear strain value for point C is 0.817%. An octahedral shear strain rate of $10^{-4}s^{-1}$ was chosen which converts to an axial strain rate of $1.52\times10^{-4}s^{-1}$ and a shear strain rate of $1.22\times10^{-4}s^{-1}$. In the calculation of the corresponding axial and shear strains and the strain rates, a value of 0.4 for the Poisson's ratio was used.

The axial stress responses for the two loading paths $\overline{OAC}$ and $\overline{OBC}$ at the octahedral shear strain rate of $10^{-4}s^{-1}$ are shown in Fig.4.13. The solid square symbols represent the stress response for the loading path $\overline{OAC}$ and the hollow ones for the loading path $\overline{OBC}$.

For both strain paths, axial stress increases with the increase of strain until a strain value of 0.742% is reached. Prior to reaching the aforementioned axial strain, the axial stress response for path $\overline{OBC}$ is slightly below that of path $\overline{OAC}$. This difference can only be attributed to the presence of a prior shear stress for the path $\overline{OBC}$. Therefore, this figure shows that the presence of a prior shear stress causes a reduction in the stiffness of the axial stress-strain behavior.

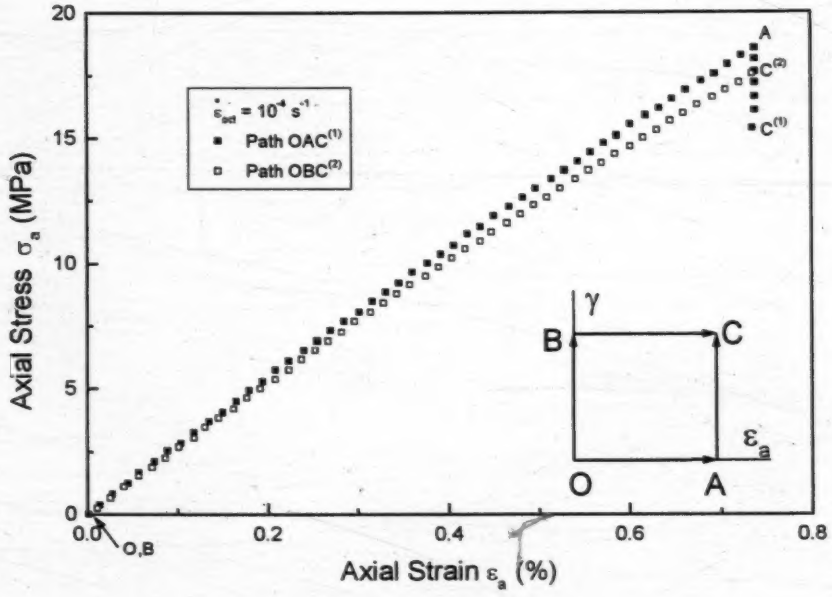

Fig.4.13 Experimental axial stress-strain curves for two different loading paths with an octahedral shear strain rate of $10^{-4}s^{-1}$

The shear stress response for the same strain paths is depicted in Fig. 4.14. Again two distinct curves are observed, but the trend is reversed, i.e., the shear stress-strain curve for the path $\overline{OBC}$ is slightly higher than that of $\overline{OAC}$ due to the presence of a prior axial

stress in the latter path. Therefore, the existence of a prior axial stress also causes a reduction in the stiffness of the shear stress-strain curve.

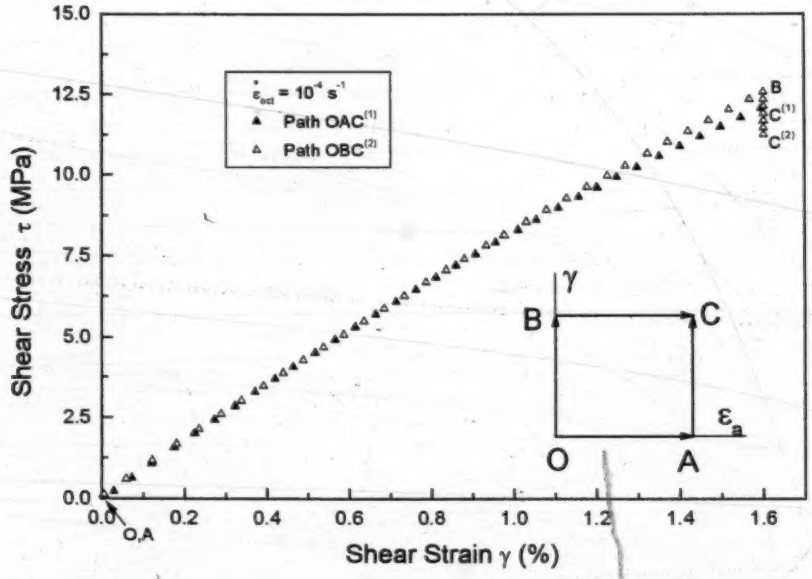

Fig.4.14 Experimental shear stress-strain curves for two different loading paths with an octahedral shear strain rate of $10^{-4}\,s^{-1}$

With reference to Fig. 4.13 and path $\overline{OAC}$, the axial stress drops from point A to the lowest point C by about 3.06 MPa when the shear stress, path AC, is applied. The corresponding drop in the shear stress from point B to lowest point C in Fig.4.14 is about 1.32 MPa. In Figs. 4.13 and 4.14 there are two points labeled C. They are referred to the axial (shear) stresses reached by the different strain paths. The axial and shear stress drops observed in Figs. 4.13 and 4.14 are due to the stress relaxation while the axial or shear strains are kept constant. There may also be due to the interaction of the increase in shear

or axial stresses as shown in Chapter 3 for the EPON 826 epoxy or by Krempl and Bordonaro (1998).

From the above two tests, it is seen that a normal (shear) stress influences the shear (normal) stress-strain behavior of the ColdCure, similar to those observed in the EPON 826 epoxy. The phenomenon that the presence of a normal (shear) stress reduces the shear (normal) stress that can be sustained, or the stiffness decreases due to the presence of a second stress component is observed for the two epoxy systems.

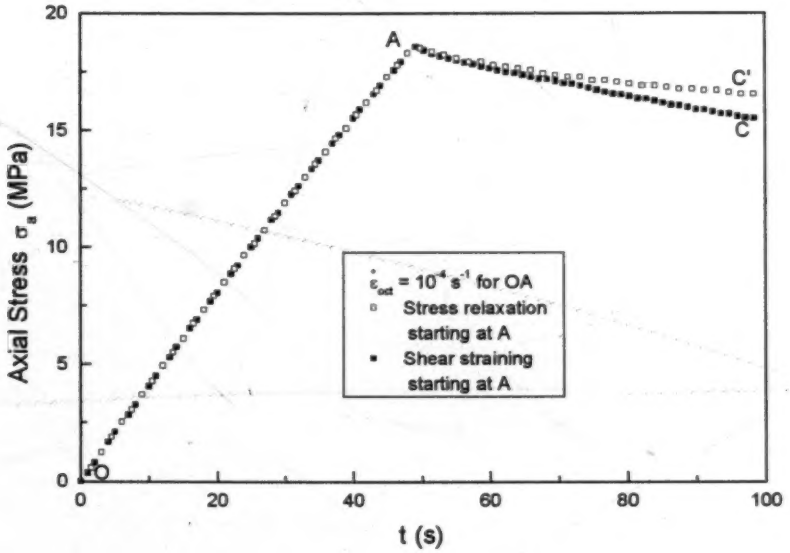

Fig.4.15 Comparison of the axial stress-strain curves for two different loading paths to determine the shear stress (strain) interaction effect

In order to determine the contribution to the total stress drop by each of the above factors, another test was performed in which the axial strain was first applied at a constant octahedral shear strain rate of $10^{-4} s^{-1}$. After it reached point A, the strain was kept

constant instead of applying a shear strain as in path $\overline{OAC}$ of Fig.2.12. The corresponding stress response ($\overline{OAC'}$) is shown in Fig.4.15, in conjunction with that of path $\overline{OAC}$. Note that the stress drop from A to C' is due to stress relaxation only, while the stress drop from A to C is a result of both the stress relaxation and shear stress interaction. It is seen from the figure that about 1/3 of the total stress drop can be attributed to the shear stress interaction effect.

4.5.2 Strain-rate effect

The effect of strain rate was studied by performing the above tests at a different octahedral shear strain rate of $10^{-5}s^{-1}$. The corresponding axial and shear strain rates were $1.52\times10^{-5}s^{-1}$ and $1.22\times10^{-5}s^{-1}$, respectively, for the corner path tests.

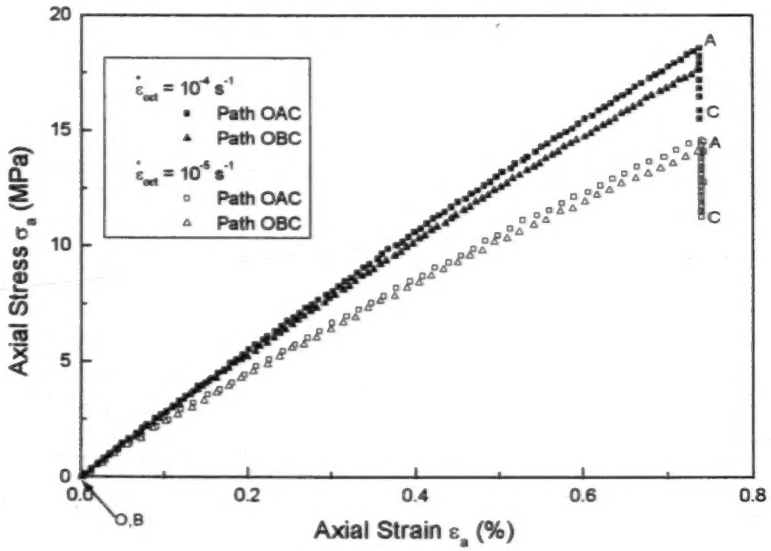

Fig.4.16 Experimental axial stress-strain curves for two different loading paths at two octahedral shear strain rates of $10^{-4}s^{-1}$ and $10^{-5}s^{-1}$

Figures 4.16 and 4.17 show the axial stress versus axial strain and the shear stress versus shear strain for two octahedral shear strain rates of $10^{-4}s^{-1}$ and $10^{-5}s^{-1}$. It is noted that there is no significant *relative* difference between the stress responses due to the path effect as a result of change in the strain rate of one order of magnitude. However, the change in the strain rate has a noticeable influence on the stiffness of the stress-strain response.

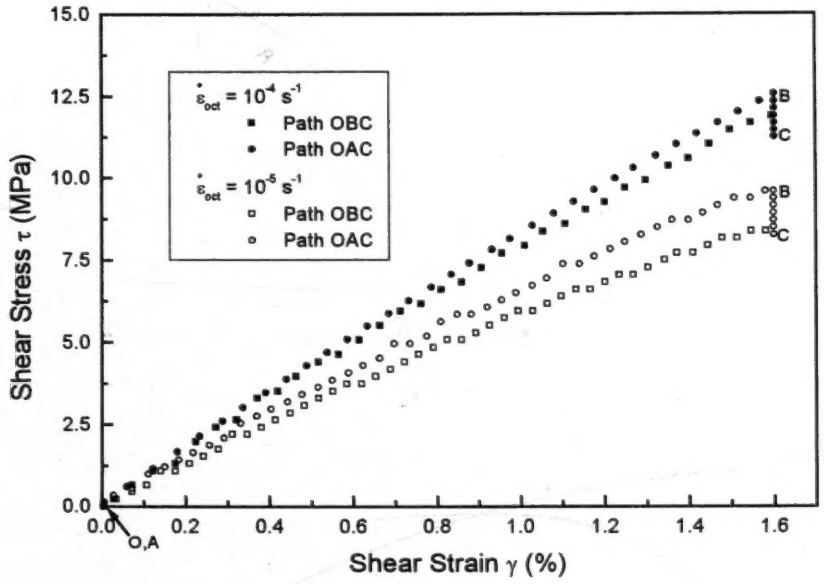

Fig.4.17 Experimental shear stress-strain curves for two different loading paths at two octahedral shear strain rates of $10^{-4}s^{-1}$ and $10^{-5}s^{-1}$

4.6 Failure Behavior

The failure behavior of ColdCure epoxy was investigated by a series of strain-controlled tests loading till failure of the tested specimen. Loading paths with different strain ratios were used to study the multiaxial behavior of the ColdCure epoxy, including failure modes and failure stress envelopes. However, only certain typical stress-strain curves till failure

are shown here as a demonstration of the effect of different stress states on the failure behavior. These curves include uniaxial tensile, equibiaxial tensile and pure shear. Their corresponding stress-strain curves are shown as follow.

Figure 4.18 shows the tensile curves to failure at an octahedral shear strain rate of $10^{-4}\ s^{-1}$. The stress-strain curve shows high nonlinearity before failure. The failure mode is brittle fracture. The failure stress value at this strain rate is 40.8MPa and the failure axial strain is 2.7%. Compared with the uniaxial tensile failure of EPON 826 epoxy at the same octahedral shear strain rate of $10^{-4}\ s^{-1}$, the failure stress and the failure strain for this epoxy are only half of the EPON 826, showing a considerable lower strength and tounghness.

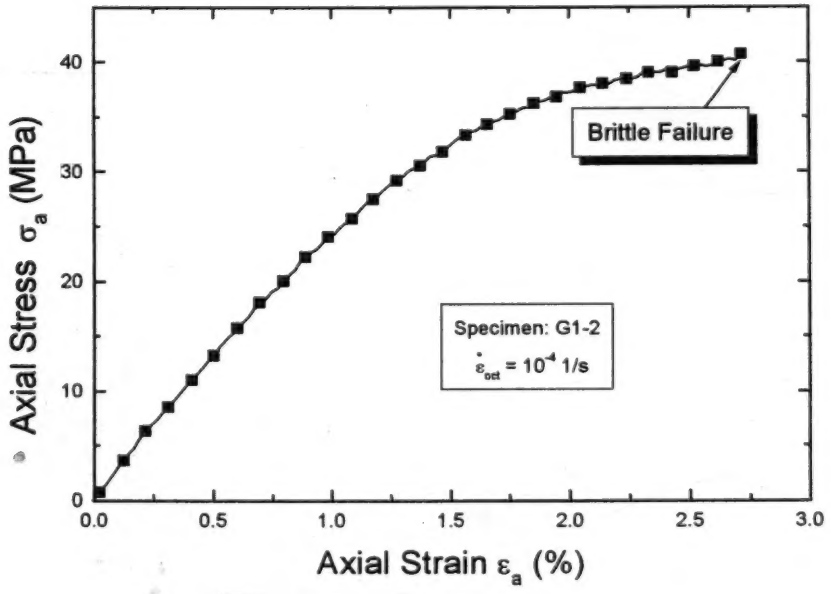

Fig.4.18 Tensile stress-strain curve to failure at an octahedral shear strain rate of $10^{-4}\ s^{-1}$

The equibiaxial stress-strain curves to failure at two different octahedral shear strain rates are shown in Fig. 4.19. It is evident that these typical biaxial stress-strain curves have some common features as the uniaxial curves shown in Fig. 4.18. For example, linear behavior can be distinguished at very low stress levels in both axial and hoop stress-strain curves. With the increased strain, the rate of increase in stress decreases in both loading directions. The axial and hoop stress-strain curves are slightly different. The equibiaxial tests also failed in a brittle mode and the magnitude of the failure stress increases with the increase in applied strain rate.

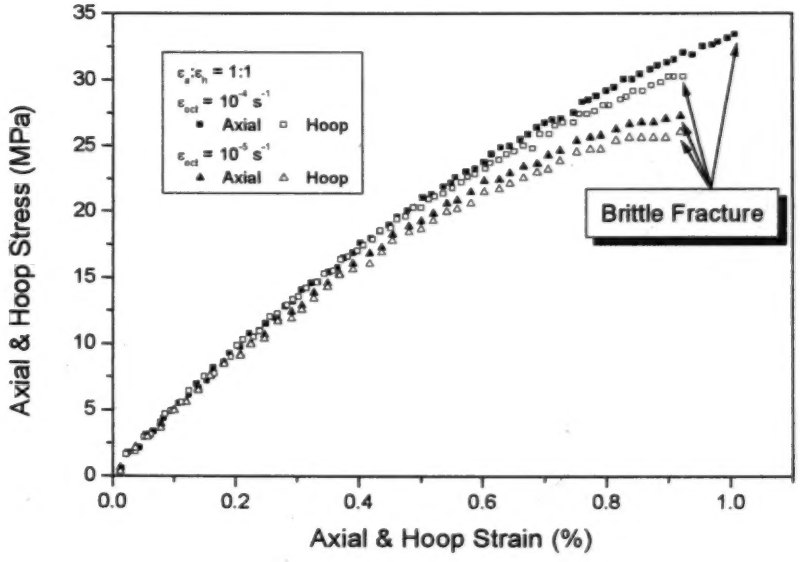

Fig.4.19 Equibiaxial stress-strain curves to failure at two different octahedral shear strain rates $10^{-4}\ s^{-1}$ and $10^{-5}\ s^{-1}$

The pure shear stress-strain curve to failure at an octahedral shear strain rate of $10^{-4}\ s^{-1}$ is shown in Fig.4.20. This curve has a maximum stress before it drops to its final failure and

shows a ductile yield behavior. Compared with the pure shear failure of EPON 826 epoxy at the same octahedral shear strain rate of $10^{-4}\ s^{-1}$, the failure stress and the failure strain for this epoxy are much lower.

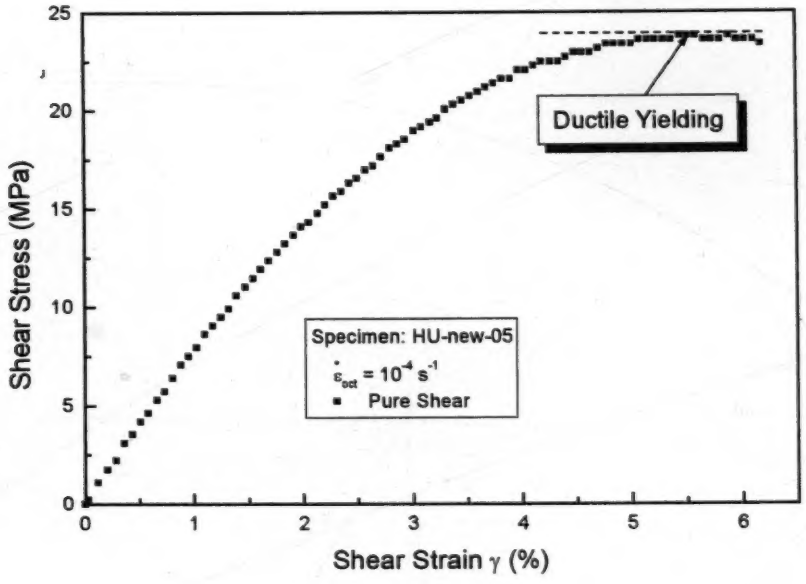

Fig.4.20 Shear stress-strain curve to failure at the octahedral shear strain rate of $10^{-4}\ s^{-1}$

Comparison of Figs. 4.18 to 4.20 shows that the failure modes are different: the failure mode for uniaxial tensile and equibiaxial tensile tests is brittle fracture while that of the pure shear test is ductile yielding. The failure modes show similar dependence on the hydrostatic stress as that of EPON 826 epoxy (see Fig. 3.16). There is a ductile-to-brittle transition between the uniaxial tensile and pure shear stress states.

The quantitative relationship between the failure stress and the hydrostatic stress is shown in Figs. 4.21 and 4.22. In these figures, the experimental failure data are compared with the modified von Mises and modified Tresca criteria of Eq. (3.7). Internal friction coefficient μ is also obtained by the best fit to the experimental data. The values of μ for the modified Tresca and modified von Mises criteria are 0.317 and 0.336, respectively. It is observed that the modified Tresca criterion has a better fit to the experimental data.

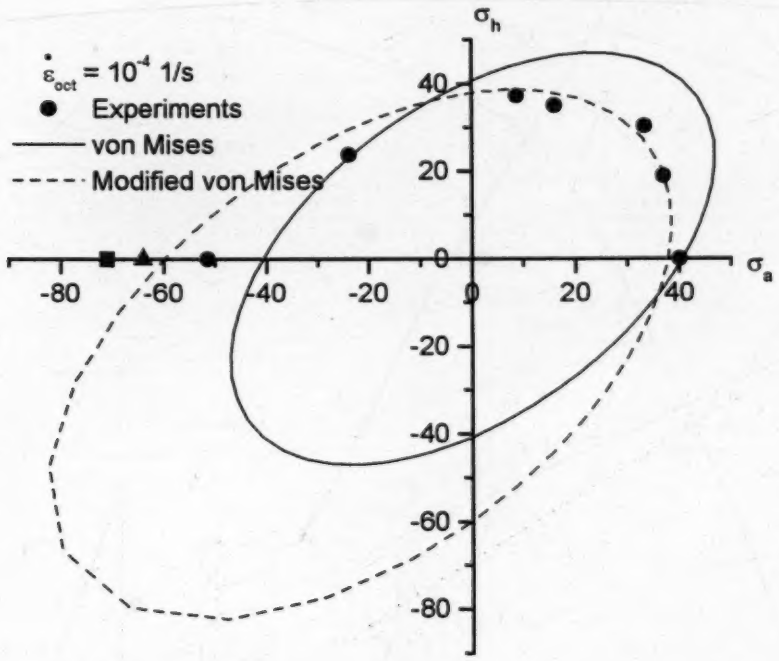

Fig.4.21 Comparison of experimental data with modified von Mises criterion

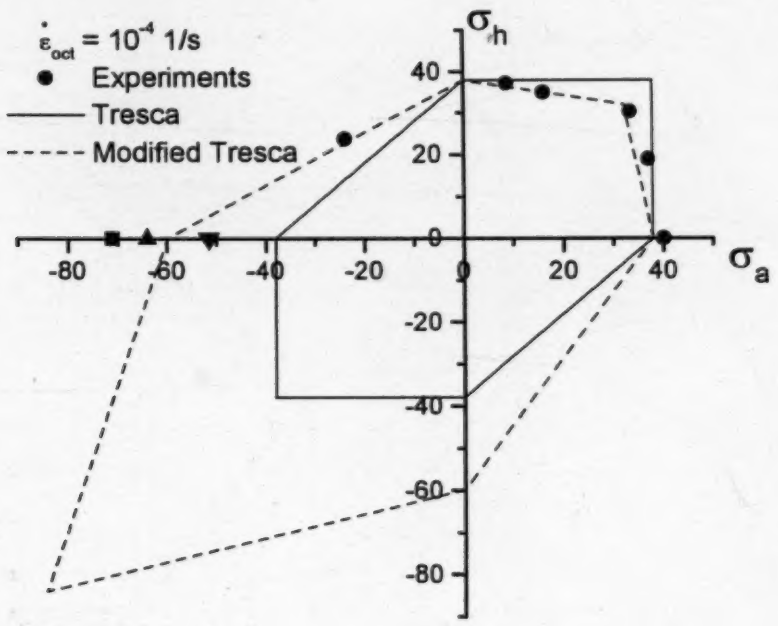

Fig.4.22 Comparison of experimental data with modified Tresca criterion

4.7 Concluding Remarks

From the results presented in this experimental investigation, the following conclusions are drawn for the ColdCure epoxy:

- The ColdCure epoxy shows strong nonlinear viscoelastic behavior. It has lower creep stresses and smaller creep strains than that of the EPON 826 epoxy. It also exhibits slower strain recovery and higher creep compliance, demonstrating much lower strengths and toughness than that of the EPON 826 epoxy.
- The deformation behavior of this epoxy resin is influenced by hydrostatic stress, whether in the form of hydrostatic pressure, or the combined hydrostatic part of any stress state. The compressive component increases the stiffness and strength of the polymer. Conversely, the hydrostatic pressure does not have significant effect on EPON 826.

- Multiaxial behavior of this epoxy can be best fitted by a Stassi equation. The particular characteristic of the equation is its inclusion of a hydrostatic stress term.
- A normal (shear) stress influences the shear (normal) stress-strain behavior. The presence of a normal (shear) stress reduces the shear (normal) stress that can be sustained, or the stiffness decreases due to the presence of a second stress component, similar to those of the EPON 826.
- This epoxy failed in two different modes and this can be explained by hydrostatic stress effect. The failure behavior is best fitted by a modified Tresca criterion, similar to that of the EPON 826 epoxy.
- Scatter of test data from different specimens is much larger than that of EPON 826 epoxy. The most possible reasons for this are attributed to different batches of the original materials and the trapped air inside the specimens.

Bibliography

1. Krempl, E. and Bordonaro, C.M., 1998, Non-proportional Loading of Nylon 66 at Room Temperature, International Journal of Plasticity, 14, 245-258.
2. Stassi-D'Alia, F., 1967, Flow and Fracture of Materials According to a New Limiting Condition of Yielding, Meccanica, 3, 178-195.
3. Ward I. M., 1971, Review: The Yield Behaviour of Polymers, Journal of Materials Science, 6, 1397-1417.
4. Whitney W., and Andrews R.D., 1967, Yielding of Glassy Polymers: Volume Effects, Journal of Polymer Science: Part C, 16, 2981-2989.
5. Wolodko, J., 1999, Biaxial Fatigue and Leakage Characteristics of Fiber Reinforced Composite Tubes, Ph.D. Dissertation, University of Alberta, Edmonton, Canada.

Chapter 5

Development of Nonlinear Viscoelastic Constitutive Model for Polymeric Materials

It has been shown in Chapters 3 and 4 that there are certain features of epoxy resins which are different from those of the elastic-plastic materials, e.g. time effect and hydrostatic stress dependency. These deformation characteristics have design implications. For example, due to time-dependent behavior, dimensional changes in polymeric structures occur during their service life, and these have to be considered during the design phase of such structures. Although experimental investigations provide very useful information for the design of polymeric structures, they are generally expensive and time consuming to perform, especially for long-term behavior testing.

With the advent of high-speed computation hardware and software, numerical methods are finding more and more applications in evaluating the behavior of polymeric structures. For example, finite element methods have been widely used for the stress analysis and strength evaluation of polymeric structures (Chen et al., 2001, Yi and Hilton, 1997, among others). However, the success of such applications is largely dependent on the accurate description of the deformation behavior of constituents involved, especially the properties of matrices since fibers can generally be considered to remain linear elastic within their application range. Therefore, a proper constitutive modeling of deformation behavior of polymer matrices is a prerequisite in attempting to predict the overall stress-strain responses of the

fiber-reinforced composites, as well as an understanding of their long-term performance and failure mechanisms.

It was mentioned in Chapter 1 that various types of constitutive formulations have been proposed to describe the mechanical behavior of polymeric materials. Because of the complex features exhibited by polymers, no single constitutive model is currently available which can describe all aspects of one polymer, let alone different polymers (Schapery, 2000).

A further objective of this research is the development of proper constitutive models to describe the mechanical behavior of epoxy resins including the typical deformation features exhibited by the two tested epoxy resins. Because of the nonlinear and multiaxial nature experienced by polymeric structures in practical engineering applications, a multiaxial nonlinear viscoelastic constitutive model is required for the reliable prediction of the deformation and strength of polymeric structures. The development of such a constitutive model is discussed in this chapter.

Here, a new nonlinear viscoelastic constitutive model, in differential form, is presented. In comparison with the previous differential models (Xia and Ellyin, 1998, Zhang and Moore, 1997), several modifications have been introduced in the present model. The modifications and improvements are made on the basis of the experimental observations of the deformation behavior of the two epoxy resins reported in Chapters 3 and 4. A distinctive feature of this model is the inclusion of a criterion to delineate loading and unloading in multiaxial stress states, and different moduli for loading and unloading behaviors. In

addition, the model contains only five material constants and one modulus function, which can be calibrated in accordance with a well defined procedure. An integral form of constitutive model is also included for a comparative purpose. The predictions of these two forms of constitutive model and the comparison with the experimental data are presented in the next two chapters.

5.1 Developed Differential Model

Differential models are physically based and rheological. They can be constructed by a combination of elastic springs and viscous dashpots in a uniaxial representation. The springs and dashpots obey Hook's law and Newton's law of viscosity, respectively. These types of rheological models ensure that the description of the deformation process is reliable and that the conservation laws of energy are preserved. Another advantage of the differential model is that it is relatively simple to insert into a general-purpose finite element code; thus facilitating its application.

The simplest models consist of a single spring and a single dashpot either in series or in parallel and these are known as the Maxwell model and the Kelvin (Voigt) models, respectively, as shown in Fig. 1.11, Chapter 1. However, both models describe the behavior of a viscoelastic material to a first approximation only, and neither model is adequate for the general behavior of a viscoelastic material. As a matter of fact, the models described above have only one relaxation or retardation time, whereas real materials often behave as though they have several relaxation times because of their complex micro-structure. Even two or three Kelvin (Voigt) elements connected in series was found to be very approximate in describing the deformation behavior of an epoxy polymer (Xia and

Ellyin, 1997). To deal with this situation, more elements have to be included and this will inevitably bring in the difficulty in determining the model constants and implementing complicated numerical analysis of the models. In certain cases, a trial-and-error method had to be employed. One of the examples is the differential model by Xia and Ellyin (1998). The proposed model alleviates the drawback of material constant calibration by using a similar procedure advocated by Zhang and Moore (1997).

5.1.1 General description of the model

In the current model, the total strain rate $\{\dot{\varepsilon}_t\}$ is assumed to be the sum of the elastic and creep strain rates, $\{\dot{\varepsilon}_e\}$ and $\{\dot{\varepsilon}_c\}$, respectively, i.e.,

$$\{\dot{\varepsilon}_t\}=\{\dot{\varepsilon}_e\}+\{\dot{\varepsilon}_c\} \tag{5.1}$$

The elastic strain rate is calculated through Hooke's law,

$$\{\dot{\sigma}\}=E[A]^{-1}\{\dot{\varepsilon}_e\} \tag{5.2}$$

In the above, $\{\dot{\varepsilon}_t\}$, $\{\dot{\varepsilon}_e\}$, $\{\dot{\varepsilon}_c\}$ and $\{\dot{\sigma}\}$ are corresponding strain and stress vectors (six components), E is an elastic modulus which is assumed to be a constant, and $[A]$ is a matrix related to the value of Poisson's ratio, defined by

$$[A]=\begin{bmatrix} 1 & -\upsilon & -\upsilon & 0 & 0 & 0 \\ -\upsilon & 1 & -\upsilon & 0 & 0 & 0 \\ -\upsilon & -\upsilon & 1 & 0 & 0 & 0 \\ 0 & 0 & 0 & 1+\upsilon & 0 & 0 \\ 0 & 0 & 0 & 0 & 1+\upsilon & 0 \\ 0 & 0 & 0 & 0 & 0 & 1+\upsilon \end{bmatrix} \tag{5.3}$$

For a number of Kelvin (Voigt) elements connected in series, creep strain rate $\{\dot{\varepsilon}_c\}$ is the sum of the strain rate of each element $\{\dot{\varepsilon}_{ci}\}$, i.e.

$$\{\dot{\varepsilon}_c\} = \sum_{i=1}^{n} \{\dot{\varepsilon}_{ci}\} = \sum_{i=1}^{n} \left(\frac{[A]}{E_i \tau_i} \{\sigma\} - \frac{1}{\tau_i} \{\varepsilon_{ci}\} \right) \tag{5.4}$$

In the above $\tau_i = \eta_i / E_i \ \ (i = 1, 2, \cdots, n)$ denotes the retardation time, E_i is the spring stiffness and η_i is the dashpot viscosity for the i-th Kelvin (Voigt) element, respectively. Thus, the combination of eqs. (5.1) and (5.4) represents a model of one linear spring and several nonlinear Kelvin elements connected in series in a unixial representation. It is to be noted that the retardation time τ_i in the eq. (5.4) has a damped exponential character as in an exponential-type function. Its value determines a time duration after which contribution from the individual Kelvin element becomes negligible. Therefore, the number of the Kelvin elements adopted in the constitutive equation depends on the required time range. For simplicity, we introduce a time scale factor α, and assume that

$$\tau_i = (\alpha)^{i-1} \tau_1 \tag{5.5}$$

In this way all τ_i are related through the scale factor α. α was taken to be 10 so that each Kelvin element in the series dominates one order of conventional time interval.

The experimental data in Chapters 3 and 4 also show clearly the nonlinear viscoelastic behavior of the studied epoxy polymers. There are several ways to incorporate the nonlinearity into the constitutive equation (Xia and Ellyin, 1998, Zhang and Moore, 1997 among others). The description of the nonlinear behavior in the current model was achieved by letting E_i be a function of the current equivalent stress, σ_{eq}. The reason for this stems from the experimental observation that creep compliance increases with the increase in applied stress as shown in Figs.3.3 and 4.3, i.e., creep stiffness E_i decreases with the decrease in applied stress and has a monotonic function form with regard to the

applied stress in a uniaxial stress state or an applied equivalent stress in a multiaxial stress state. Furthermore, a single function form for all E_i is assumed, i.e.

$$E_i = E_1(\sigma_{eq}) \tag{5.6}$$

The values of constants ($E, \upsilon, \alpha, \tau_1$) and the function form of $E_1(\sigma_{eq})$ can be determined from the uniaxial creep curves at different stress levels following a routine procedure. This will be described later on in section 5.1.4.

5.1.2 Description of unloading behavior

For most polymers, as pointed out in many references (see e.g., Ward (1983) and Pae and Bhateja, (1975)), the unloading behavior is usually significantly different from the loading response. This is also true for many other path- and history-dependent engineering materials. For example, for elasto-plastic materials, unloading usually indicates an abrupt change from plastic loading to elastic unloading. In an elasto-plastic constitutive model (Ellyin et al., 1995) three different loading cases (elastic loading, monotonic plastic loading and plastic reloading) have been distinguished in order to correctly describe the complex plastic behavior of materials. For the viscoelastic materials, it is also imperative that the constitutive model should have the ability to distinguish the loading and unloading cases. As such, one first has to have a criterion to distinguish unloading from loading. In plasticity, the mechanism associated with unloading is well understood and the criterion is well developed. The concept of unloading in plasticity is closely related to the yield surface (including the subsequent yield surfaces). In viscoelasticity, there is no such clear concept akin to the yield surface. However, it is possible to introduce a *current loading surface*, which is defined as a stress envelope on which the current stress resides. If σ_{ij}^t is

the current stress point at time t, σ_{ij}^0 is the stress point at which the last switch of loading/unloading takes place and $d\sigma_{ij}^t$ is the stress increment at time t, then

$$f\left(\sigma_{ij}^t - \sigma_{ij}^0\right) = R^2 \tag{5.7}$$

defines a current loading surface, and $(\frac{\partial f}{\partial \sigma_{ij}})_{\sigma_{ij}=\sigma_{ij}^t}$ represents the direction of the normal to the loading surface at the current stress point. A criterion thus can be introduced to define the change from loading to unloading or vice versa as follow (see Fig. 5.1):

- if $\frac{\partial f}{\partial \sigma_{ij}} d\sigma_{ij}^t \geq 0$, no chang in loading or unloading;
- if $\frac{\partial f}{\partial \sigma_{ij}} d\sigma_{ij}^t < 0$, either change from loading to unloading or vice versa.

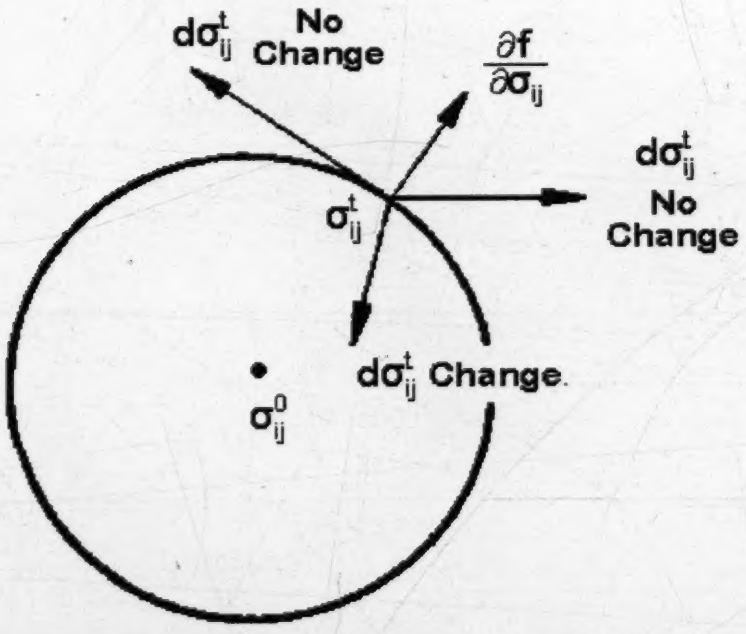

Fig. 5.1 Schematic representation of loading/unloading criterion

The functional form of f could be taken to be the same form as the von Mises surface, i.e.

$$f = \frac{3}{2}\bar{S}_{ij}\bar{S}_{ij} = \frac{3}{2}(S_{ij} - S_{ij}^0)(S_{ij} - S_{ij}^0) = R^2 \text{ and } R^2 = \frac{3}{2}(S_{ij}^t - S_{ij}^0)(S_{ij}^t - S_{ij}^0). \quad (5.8)$$

where $S_{ij} = \sigma_{ij} - \sigma_{kk}/3$ is the deviatoric part of the stress tensor.

If loading starts from virgin state, $\sigma_{ij}^0 = 0$. At the instant at which one switches from loading to unloading or vice versa, σ_{ij}^0 is updated to the stress point at that instant.

Having defined the criterion for the unloading, we now concern ourselves with the specification of the material constants and the modulus function for the unloading case. Phenomenological observation on the loading-unloading stress-strain curves indicates that the slope of the loading branch decreases with the incresing stress while the trend is opposite in the unloading branch. The slope is closely related to the value of $E_1(\sigma_{eq})$ in eq. (5.6). In the loading case, the $E_1(\sigma_{eq})$ has been defined as a decreasing function of the applied stress which is consistent with the experimental observations (See Fig. 5.2). If the same function of $E_1(\sigma_{eq})$ was used for the unloading case, an opposite trend for the slope change would be produced. As a first approximation, it is assumed that E_1 remains the same during the entire unloading process. In addition, to satisfy continuity with the loading modulus function, it is assumed that the constant value is just equal to the value of E_1 at the switch stress point, σ_{ij}^0, where unloading takes place. All other material constants remain the same for both loading and unloading regimes. It will be seen later on that by using such a simple unloading rule, the model does predict very well the various test results including unloading cases.

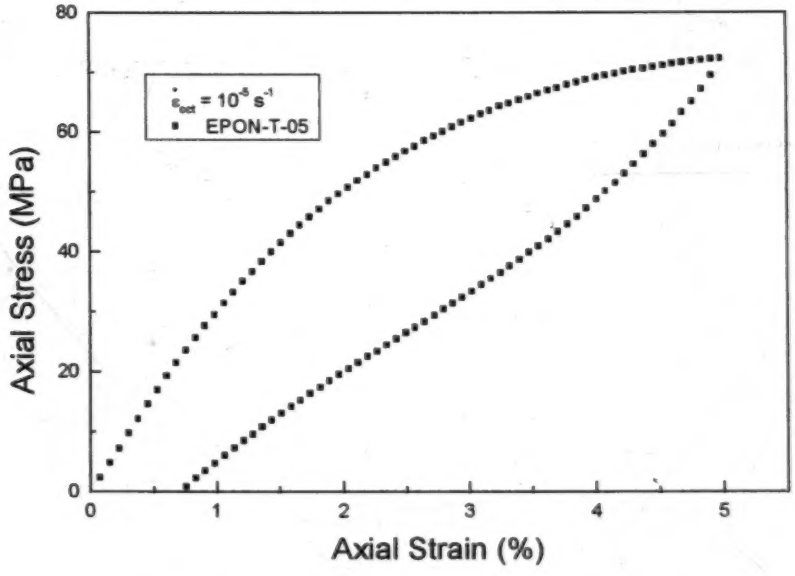

Fig. 5.2 Loading/unloading behavior of EPON 826/EPI-CURE 9551

5.1.3 Equivalent stress representation

For the EPON 826 and ColdCure epoxy resins, it was shown in Chapters 3 and 4 that the multiaxial behavior of the two epoxy resins can be described by a Stassi equation. For a multiaxial stress state, the corresponding expression is as follow:

$$3J_2 + (R-1)\sigma^* I_1 = R\sigma^{*2} \tag{5.9}$$

where $I_1 = \sigma_1 + \sigma_2 + \sigma_3$ is the first invariant of a stress state, $J_2 = s_{ij}s_{ij}/2$ is the second invariant of the deviotoric stress. In the above σ^* is a uniaxial tensile yield stress in the original Stassi equation (Stassi, 1969) and R is the ratio of a uniaxial compressive yield stress to a uniaxial tensile yield stress.

If σ^* in Eq. (5.9) is set to be the equivalent stress, σ_{eq}, then one gets,

$$\sigma_{eq} = \frac{(R-1)I_1 + \sqrt{(R-1)^2 I_1^2 + 12RJ_2}}{2R} \tag{5.10}$$

which is different from the von Mises equivalent stress, $\sigma_{eq} = \sqrt{3J_2}$. The equivalent stress expressed in Eq. (5.10) is used in the current model for calculating the modulus function, $E_1(\sigma_{eq})$. Note that when R=1 in Eq. (5.10), then σ_{eq} reduced to the von Mises equivalent stress.

5.1.4 Determination of material constants and modulus function

The proposed constitutive model contains a total of five material constants (E, υ, α, τ_1, R) and a modulus function, $E_1(\sigma_{eq})$. Except R, which has to be determined by comparison of a uniaxial tensile curve with that of a uniaxial compressive one, all other constant and function can be obtained from the experiment data of the stepped uniaxial tensile creep tests, (see Figs. 3.1 and 4.1). Assuming that the stress σ_0 is instantaneously reached from the zero stress state, the uniaxial strain can be reformulated from the Eqs. (5.1)-(5.6) as

$$\varepsilon = \frac{\sigma_0}{E} + \frac{\sigma_0}{E_1(\sigma_0)} \sum_{i=1}^{n} (1 - e^{-\frac{t}{\alpha^{i-1}\tau_1}}) \tag{5.11}$$

The elastic modulus, E, can be determined from the stress-strain response in the initial loading stage of the stepped creep tests. If a fast loading rate is adopted in the tests, then a stable linear relationship between the stress and strain is observed. The value of E becomes that of the slope of these straight lines. The Poisson's ratio, υ, is determined from the ratio of the transverse strain to the axial strain in the uniaxial creep tests. As shown in Fig. 3.4 of Chapter 3, a relatively stable value could be obtained. The time scale factor, α, can be

taken to be equal to ten. As far as the number of the nonlinear Kelven elements is concerned, a value of n = 5 to 6 will generally suffice. Finally, the $E_1(\sigma_{eq})$ function and τ_1 are determined from the experimental creep curves at different stress levels. For each creep stress σ_0, Eq. (5.11) is used to fit the corresponding creep curve by a nonlinear least squares fit procedure. Thus stress dependent functions $E_1(\sigma_0)$ and $\tau_1(\sigma_0)$ can be obtained. The fitting results show that τ_1 is usually weakly dependent on the stress, therefore, it could be set to be the average value of all $\tau_1(\sigma_0)$ values.

5.2 Integral Model

In general, the integral representation models have the advantage of describing the time dependency in a more general form, but at times this can lead to complicated mathematics (Findley et al., 1976). Here, an integral form of constitutive model is included for a comparative purpose. Among various integral representations, a modified version of the Schapery's model, proposed by Lai and Bakker (1996), is chosen as a representative model because it accounts for the difference in response of polymers due to both hydrostatic and deviatoric stresses.

5.2.1 Model formulation

For a thermo-rheologically simple isotropic viscoelastic material under a multiaxial state of stress, the constitutive law can be expressed as:

$$\varepsilon_{ij} = \frac{1}{2} J_0 g_0 s_{ij}(t) + \frac{1}{2} g_1 \int_0^t \Delta J[\psi(t) - \psi(\tau)] \frac{d(g_2 s_{ij})}{d\tau} d\tau$$

$$+ \frac{1}{9} B_0 g_0 \delta_{ij} \sigma_{kk}(t) + \frac{1}{9} \delta_{ij} g_1 \int_0^t \Delta B[\psi(t) - \psi(\tau)] \frac{d(g_2 \sigma_{kk})}{d\tau} d\tau \qquad (5.12)$$

where J_0 and B_0 are instantaneous shear and bulk compliances; ΔJ and ΔB are transient shear and bulk compliances, respectively; ψ is reduced time, $\psi = \int_0^t \frac{d\tau}{a_\sigma}$ and $\psi(\tau) = \int_0^\tau \frac{d\tau}{a_\sigma}$; g_0, g_1, g_2 and a_σ are functions of multiaxial stress state. According to Lai and Bakker (1996), g_0 and a_σ are functions of hydrostatic stress, σ_{kk}, and g_1 and g_2 are functions of σ_{eq}, $\sigma_{eq} = \sqrt{\frac{3}{2} s_{ij} s_{ij}}$ is the von Mises equivalent stress and $s_{ij} = \sigma_{ij} - \frac{1}{3}\sigma_{kk}\delta_{ij}$ is the deviatoric stress tensor. When $g_0 = g_1 = g_2 = a_\sigma = 1$, Eq. (5.12) reduces to the linear viscoelastic equation from Boltzmann's superposition principle.

J_0, B_0, ΔJ and ΔB are related to the instantaneous tensile compliance D_0 and the transient tensile compliance ΔD by the following relations

$$\begin{aligned} J_0 &= 2(1+\upsilon) D_0 \qquad & \Delta J(\psi) &= 2(1+\upsilon)\Delta D(\psi) \\ B_0 &= 3(1-2\upsilon) D_0 \qquad & \Delta B(\psi) &= 3(1-2\upsilon)\Delta D(\psi) \end{aligned} \qquad (5.13)$$

where υ is the Poisson's ratio and determined by experiments. ΔD is described by a simple power law as $\Delta D(\psi) = D_1 \psi^n$, D_1 and n are material constants to be determined through experiments.

As pointed out by Schapery (1969), all the above material constants can be determined by carrying out a series of uniaxial creep-recovery tests at different stress levels. The fitting method will be discussed in detail in the next section.

5.2.2 Model calibration

All the model constants and functions for the integral representation are calibrated from a set of uniaxial creep-recovery curves at different stress levels. The adopted method to determine functional forms and constants was that advocated by Schapery (1969) and widely used by other researchers, see e.g., Peretz and Weitsman(1983). The basic characterization procedure will be introduced as follows:

The uniaxial form of Eq. (5.12) is (Lou and Schapery, 1971):

$$\varepsilon = D_0 g_0 \sigma(t) + g_1 \int_0^t \Delta D[\psi(t) - \psi(\tau)] \frac{d(g_2 \sigma)}{d\tau} d\tau \tag{5.14}$$

For a creep-recovery stress history, the creep strain is given by

$$\varepsilon_c = D_0 g_0 \sigma_0 + C g_1 g_2 \sigma_0 \left(\frac{t}{a_\sigma} \right)^n \tag{5.15}$$

and the strain at recovery is

$$\varepsilon_r = \frac{\Delta\varepsilon_1}{g} \left[(1 + a_\sigma \lambda)^n - (a_\sigma \lambda)^n \right] \tag{5.16}$$

where $\lambda = \frac{t - t_1}{t}$ is the nondimensional recovery time and $\Delta\varepsilon_1 = C g_1 g_2 \left(\frac{t_1}{a_\sigma} \right)^n \sigma_0$ is the creep component of strain at time t_1 as shown in Fig.5.3.

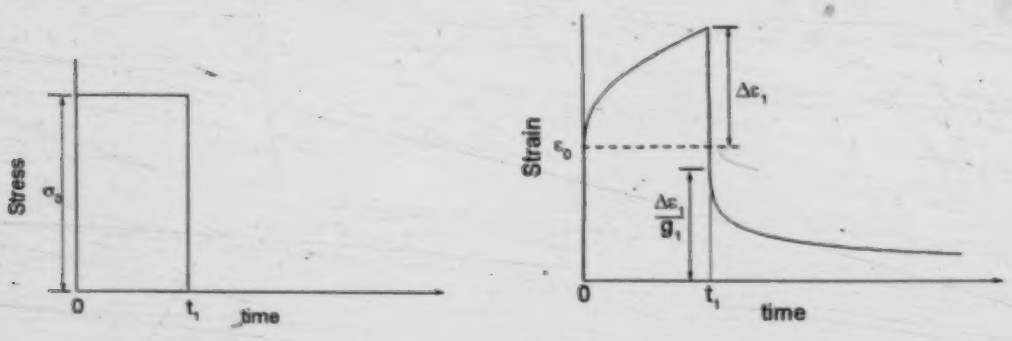

Fig.5.3 Creep-recovery stress history and corresponding strain response

Both creep and recovery data are required to determine the viscoelastic properties. At low values of creep stress the viscoelastic response is linear, Eqs. (5.15) and (5.16) reduce to the linear relations

$$\varepsilon_c = \left[D_0 + Ct^n\right]\sigma_0 \tag{5.17}$$

and the strain at recovery is

$$\varepsilon_r = \Delta\varepsilon_1\left[(1+\lambda)^n - (\lambda)^n\right] \tag{5.18}$$

As a first step, n, C, and D_0 can be determined by a least-square fitting of Eqs. (5.17) and (5.18) to a linear creep-recovery curve at low stress level. Whether a creep-recovery curve at a stress level is linear or not can be determined from the creep compliance curves as shown in Figs.3.4. For the case where linear creep-recovery curve is not available at all the tested stress levels (Fig.4.3), the curve corresponding to the lowest stress level is considered to be linear. As the strain at recovery was very small compared with the corresponding creep strain and was, therefore, easily influenced by the test system error and environments, only creep strain curve was used to obtain the values for n, C, and D_0.

For the nonlinear creep curve at high stress level σ_0, equation (5.15) can be rewritten in the form

$$\varepsilon_c = \left[D_0 g_0 + C g' t^n\right]\sigma_0 \tag{5.19}$$

where

$$g' = g_1 g_2 / a_\sigma^n \tag{5.20}$$

$g_0(\sigma_0)$ and $g'(\sigma_0)$ can be evaluated by a best fit of Eq.(5.19) to the nonlinear creep curve at the stress level σ_0. However, $g_1(\sigma_0)$, $g_2(\sigma_0)$ and $a_\sigma(\sigma_0)$ can not be seperated by the above fitting and, therefore, the strain at recovery has to be used to decompose g'. Fitting Eq.(5.16) to the strain recovery curve at the same stress level σ_0, $g_1(\sigma_0)$ and $a_\sigma(\sigma_0)$ are determined. After that, $g_2(\sigma_0)$ can be evaluated by substituting $g_1(\sigma_0)$ and $a_\sigma(\sigma_0)$ back into Eq.(5.20). Thus, the values for g_0, g_1, g_2 and a_σ at the stress level σ_0 are all determined. For a different stress level, another set of g_0, g_1, g_2 and a_σ can be found by the same procedure. When fitting Eqs. (5.15) and (5.16) to all the creep-recovery curves at different stress levels, different sets of the parameters g_0, g_1, g_2 and a_σ can be obtained. Similar to the fitting procedure for the differential representation, curve fitting can be used to produce stress dependent parameters $g_0(\sigma)$, $g_1(\sigma)$, $g_2(\sigma)$ and $a_\sigma(\sigma)$ based on those values at different stresses.

From the above description it can be seen that more material functions are introduced in the integral model (four functions compared to only one in the proposed differential model). The calibration procedure is also more complicated than that for the differential model.

5.3 Concluding Remarks

A nonlinear differential viscoelastic constitutive model has been developed. The features of this newly proposed model are as follows:

- The model can distinguish between loading and unloading cases by introducing a current loading surface and a corresponding switch rule. For the loading cases, a stress-dependent modulus function is defined; for the unloading case the modulus is assumed to be constant and is equal to the value of the modulus function at the loading/unloading switch instant.
- A new definition of equivalent stress based on the Stassi equation is used to characterize the multiaxial stress state, especially the anisotropy in the tensile and compressive behaviors and hydrostatic stress effect of epoxy resins.
- The model is relatively simple, it contains only five material constants, and a modulus function. The material constants and the modulus function can be easily determined from the uniaxial tensile creep curves at different stress levels through a routine procedure.

For a comparative purpose, an integral form of viscoelastic constitutive model is also included. The calibration process of the model constants and functions are briefly introduced.

In the next two chapters, the model constants and nonlinear functions of the two models are first obtained for the EPON 826 and ColdCure epoxy resins based on the calibration process outlined in this chapter. Then predictions have been compared with the comprehensive experimental data of the two epoxy resins including creep, recovery, various transient loading/unloading paths and multiaxial proportional or non-proportional

paths. Finally conclusions are drawn regarding the predictive accuracy of the newly proposed constitutive model.

Bibliography

1. Chen, Y., Xia, Z. and Ellyin, F., 2001, Evolution of residual stresses induced during curing processing using a viscoelastic micromechanical model, Journal of Composite Materials, 35, 522-542.
2. Ellyin, F., Xia Z. and Wu, J., 1995, New Elasto-plastic Constitutive Model Inserted into the User-supplied Material Model of ADINA, Computers and Structures, 56, 283-294.
3. Findley, W.N., Lai, J.S. and Onaran, K., 1976, Creep and Relaxation of Nonlinear Viscoelastic Materials, with an Introduction to Linear Viscoelasticity, North-Holland, Amsterdam.
4. Lai, J. and Bakker, A., 1996, 3-D Schapery Representation for Non-linear Viscoelasticity and Finite Element Implementation, Computational Mechanics, 18, 182-191.
5. Lou, Y.C. and Schapery, R.A., 1971, Viscoelastic characterization of a Nonlinear Fiber Reinforced Plastic, Journal of Composite Materials, 5, 208-234.
6. Pae, K.D and Bhateja, S.K., 1975, The Effects of Hydrostatic Pressure on the Mechanical Behavior of Polymers, Journal of Macromolecular Science – Reviews of Macromolecular Chemistry, C13(1), 1-75.
7. Peretz, D. and Weitsman, Y., 1983, The Nonlinear Thermoviscoelastic Characterization of FM-73 Adhesives, Journal of Rheology, 27, 97-114.
8. Schapery, R.A., 1969, On the Characterization of Nonlinear Viscoelastic Materials, Polymer Engineering and Science, 9, 295-310.
9. Schapery, R.A., 2000, Nonlinear Viscoelastic Solids, International Journal of Solids and Structures, 37, 359-366.

10. Stassi-D'Alia, F., 1969, Limiting Conditions of Yielding for Anisotropic Materials, Meccanica, 4, 349-364.

11. Ward, I.M., 1983, Mechanical Properties of Solid Polymers, Wiley, New York.

12. Xia, Z. and Ellyin, F., 1998, Time-Dependent Behaviour and Viscoelastic Constitutive Modelling of an Epoxy Polymer, Polymers and Polymer Composites, 6, 75-83.

13. Yi, S. and Hilton, H.H., 1997, Free Edge Stresses in Elastic and Viscoelastic Composites Under Uniaxial Extension, Bending, and Twisting Loadings, Transactions of the ASME, Journal of Engineering Materials and Technology, 119, 266-272.

14. Zhang, C. and Moore, D., 1997, Nonlinear Mechanical Response of High Density Polyethylene. Part II: Uniaxial Constitutive Modeling, Polymer Engineering and Science, 37, 414-420.

Chapter 6

Model Predictions for the Mechanical Behavior of Epon 826/EPI-CURE 9551 Epoxy System

A new differential model was proposed in the previous chapter based on the experimental observation of the deformation behavior of two epoxy resins: EPON 826 and ColdCure. In this chapter, the model (hereafter, it is called differential model or simply differential) is used to predict the deformation behavior of the EPON 826/EPI-9551 epoxy resin. The material constants and modulus function for the model are first calibrated. Then, the predictions from this model are compared with the experimental results reported in Chapter 3. For the sake of comparison, the predictive results of the integral model are also included.

6.1 Model Constants and Functions

Following the procedures described in Chapter 5, the material constants and functions for the two models were calibrated as follows:

6.1.1 Differential model

There are five material constants ($E, \upsilon, \alpha, \tau_1, R$) and the function form of $E_1(\sigma_{eq})$ to be determined for this epoxy. From the stress-strain curves of the first 5 seconds loading stage in the stepped creep tests (Fig.3.1), the slopes of these curves were found to be almost constant with very small variations, thus, the constant E was obtained by averaging the slopes for different stress levels. After E was obtained, $E_1(\sigma_{eq})$ and τ_1 were determined from fitting eq. (5.11) with the experimental creep curves at different stress levels as

shown in Fig.3.1. The Poisson's ratio, υ, was determined from the ratio of the transverse strain to the axial strain in the same set of uniaxial creep tests (Fig.3.3), a relatively stable value of 0.42 could be obtained. α was taken to be equal to ten, and six Kelvin (Voigt), together with one spring in series, were chosen to simulate the deformation behavior of the tested epoxy polymer. R was determined by comparison of a uniaxial tensile curve (Fig. 3.11) with that of a compressive one (Fig. 3.13).

Following the above described procedure, all the material constants and the modulus function in the differential constitutive model were calibrated. The material constants and the modulus function thus determined for the EPON 826 epoxy polymer are as follow:

$$E = 3400MPa,\ \upsilon = 0.42,\ \alpha = 10,\ \tau_1 = 6.116s,\ R = 1.15,\ \text{and}$$

$$E_1(\sigma) = 1.055 \times 10^5 e^{-\frac{\sigma - 22.764}{18.000}}\ MPa \tag{6.1}$$

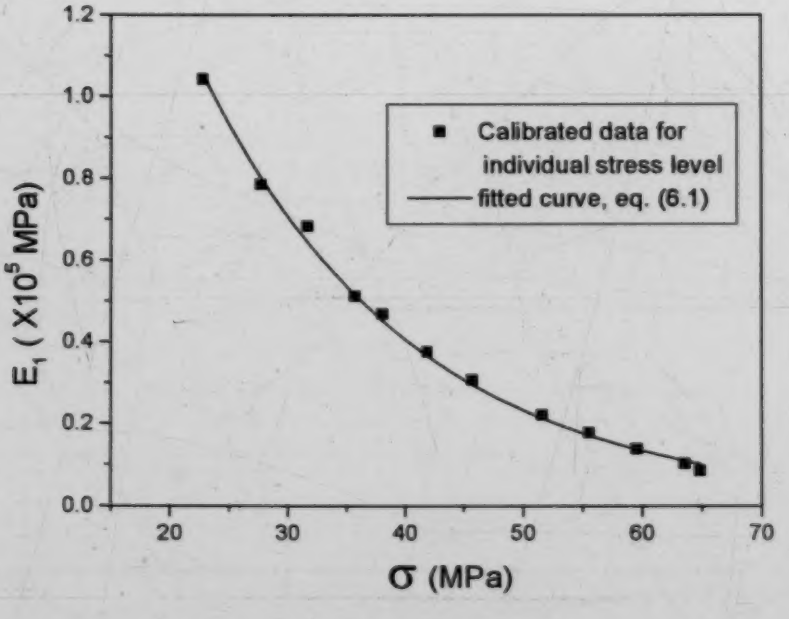

Fig.6.1 Creep modulus as a function of applied stresses

Note that the individual values of $E_1(\sigma_0)$ from fitting the creep curves at different stress levels are shown in Fig. 6.1, as well as the the final fitted curve for the function, $E_1(\sigma)$.

6.1.2 Integral model

The creep-recovery curves shown in Fig.3.1 are used to characterize the three material constants (D_0, D_1, n) and four nonlinear functions (g_0, g_1, g_2, a_σ) for the integral formulation. The constants and function relations thus obtained for the EPON 826 epoxy are listed in Table 6.1.

Table 6.1 Nonlinear viscoelasticity parameters for integral model

$D_0 = 2.86\times10^{-4}(MPa)^{-1}$, $D_1 = 9.819\times10^{-6}(\text{MPa})^{-1}$, $n = 0.145$
$g_i = \mathrm{C}_i + \mathrm{A}_i\left(\frac{\sigma}{\sigma_0}\right)^{B_i}$ (i = 0, 1, 2)
$a_\sigma = \begin{cases} 1 & for\ \sigma \le \sigma_1 \\ C_\sigma + A_\sigma e^{\frac{\sigma-\sigma_1}{B_\sigma}} & for\ \sigma > \sigma_1 \end{cases}$
$\mathrm{C}_0 = 1.0$, $\mathrm{A}_0 = 0.3250$, $\mathrm{B}_0 = 4.462$
$\mathrm{C}_1 = 1.0$, $\mathrm{A}_1 = 2.6629$, $\mathrm{B}_1 = 2.047$
$\mathrm{C}_2 = 1.0$, $\mathrm{A}_2 = 3.7015$, $\mathrm{B}_2 = 2.947$
$\mathrm{C}_\sigma = 0.2097$, $\mathrm{A}_\sigma = 0.7901$, $\mathrm{B}_\sigma = 13.845$
$\sigma_0 = 80.0$ $\sigma_1 = 18.97$

6.2 Comparison of Predicted Results with Experiments

6.2.1 Creep and recovery tests

The predicted creep and recovery curves by the differential and integral models are compared with the experimental data in Figs. 6.2 and 6.3, respectively. It is to be noted that in the current model a switch from loading to unloading occurs at the instant when the creep test is terminated. The comparision shows that the agreement is fairly good for both models. At the highest stress level, the predictive accuracy deteriorates as the nonlinear viscoelastic relations do not account for the damage which may occur at high stress levels.

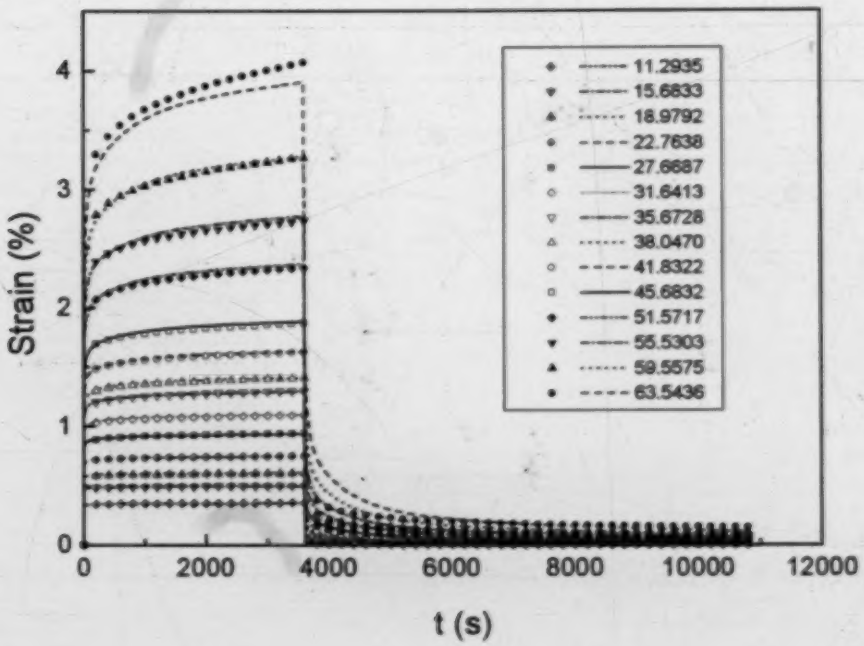

Fig.6.2 Comparison of experimental data with predicted creep-recovery curves by the differential constitutive model

As the strains at recovery are very small, especially at lower stress levels, enlarged figures only for the recovery parts of Figs. 6.2 and 6.3 are presented in Figs.6.4 and 6.5. It can be

seen that similar to the prediction ability in creep parts, the agreement at recovery parts is also fairly good at lower stress levels and the predictive accuracy deteriorates at higher stress levels. In general, the predictive capability for the creep behavior is better than that of the recovery.

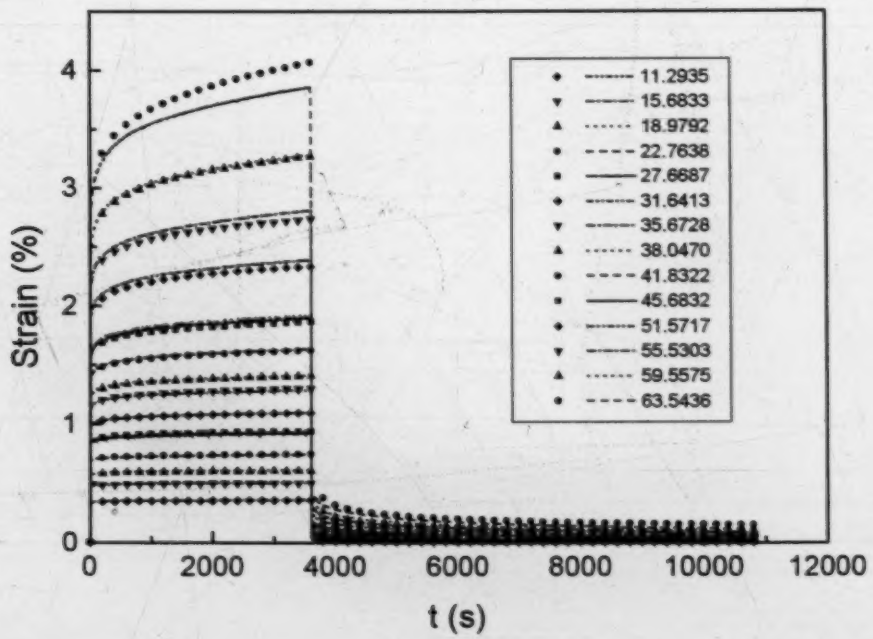

Fig.6.3 Comparison of experimental data with predicted creep-recovery curves by the integral constitutive model

Another characteristic to be noted is that for the recovery part the integral model has a better fitting to the experimental data than the differential one, which may be explained by the fact that the material parameters for the integral representation were calibrated from both the creep and recovery curves while only the creep parts were utilized for material constant and function calibration of the differential model.

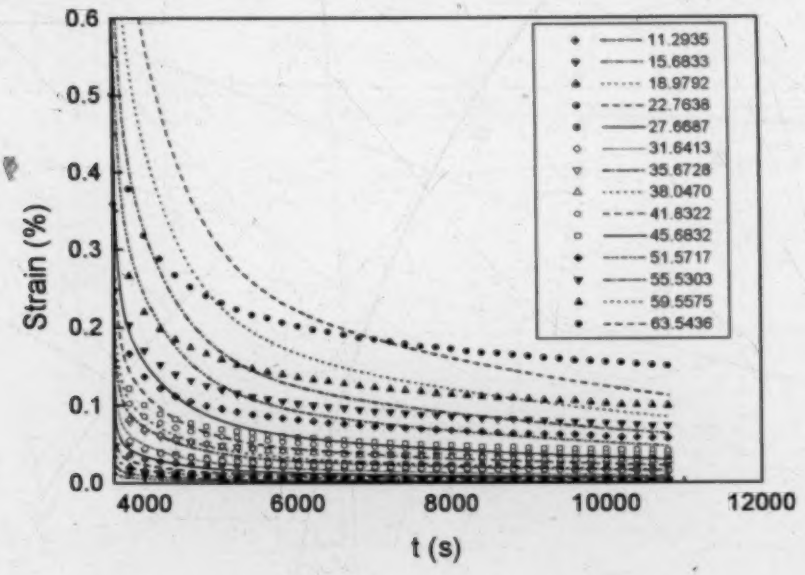

Fig.6.4 Comparison of experimental data with predicted strain curves at recovery by the differential constitutive model

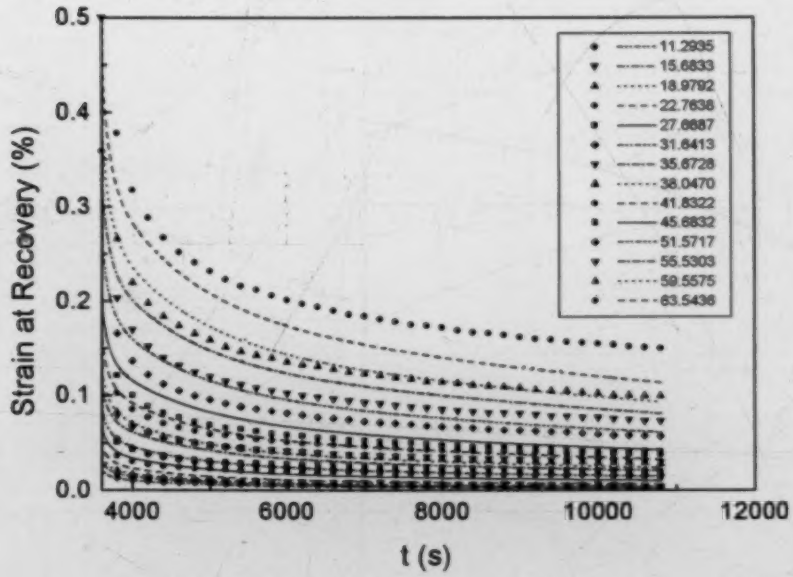

Fig.6.5 Comparison of experimental data with predicted strain curves at recovery by the integral constitutive model

Since the model parameters for the two constitutive representations were determined from the uniaxial tensile creep (and subsequent recovery for the integral model) tests, it is imperative to explore whether these models can accurately predict the response for other loading conditions. The prediction for a shear creep test at a stress level of 28.95 MPa is shown in Fig. 6.6. The predicted shear creep curve by the differential model is very close to the experimental data while that of the integral model is not as good.

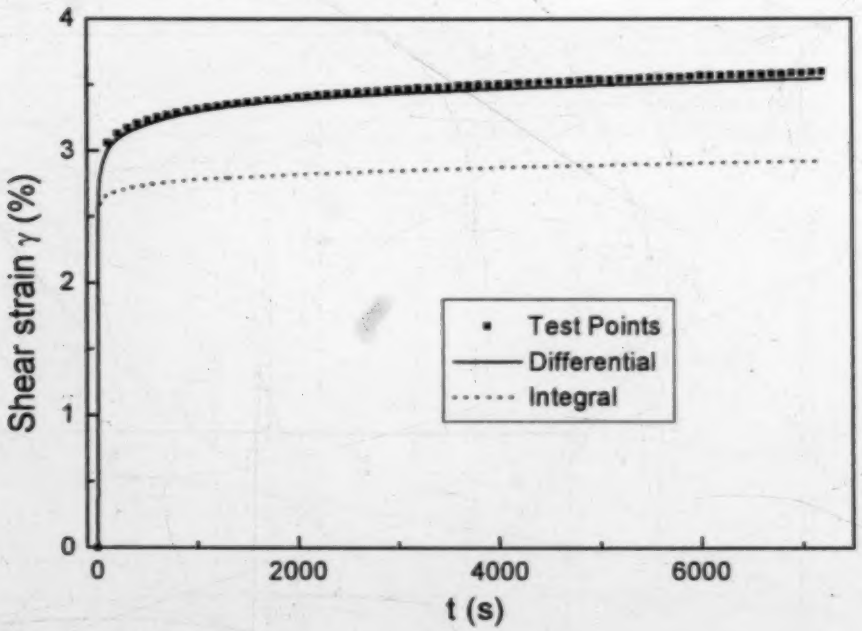

Fig.6.6 Prediction of shear creep deformation by the differential and integral constitutive models

6.2.2 Multiaxial behavior

The predicted stress envelopes for a fixed octahedral shear strain of $\varepsilon_{oct} = 2.5\%$ at three different octahedral shear strain rates of $10^{-3}\,s^{-1}$, $10^{-4}\,s^{-1}$ and $10^{-5}\,s^{-1}$ are depicted in Fig.

6.7. It is observed that both the differential and integral models can predict the anisotropic behavior of this epoxy. However, the predicted stress envelopes by the present differential model are in much better agreement with the experimental data than that of the integral model.

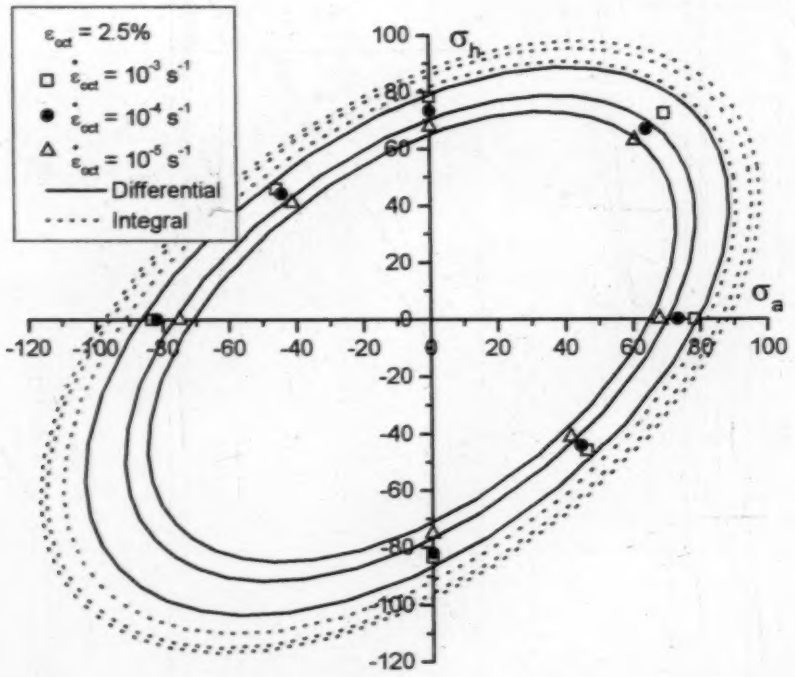

Fig.6.7 Comparison of the predicted stress envelopes by both the differential and integral models with the experimental data ($\varepsilon_{oct} = 2.5\%$)

The predicted stress envelopes for three strain values with the same octahedral shear strain rate of $10^{-4}\ s^{-1}$ are shown in Fig. 6.8. One notes significant differences between the predictions of the two constitutive models. The predicted stress envelopes by the differential model are closer to the experimental data than the integral model predictions. The latter overestimates the stress envelopes for all three strain levels.

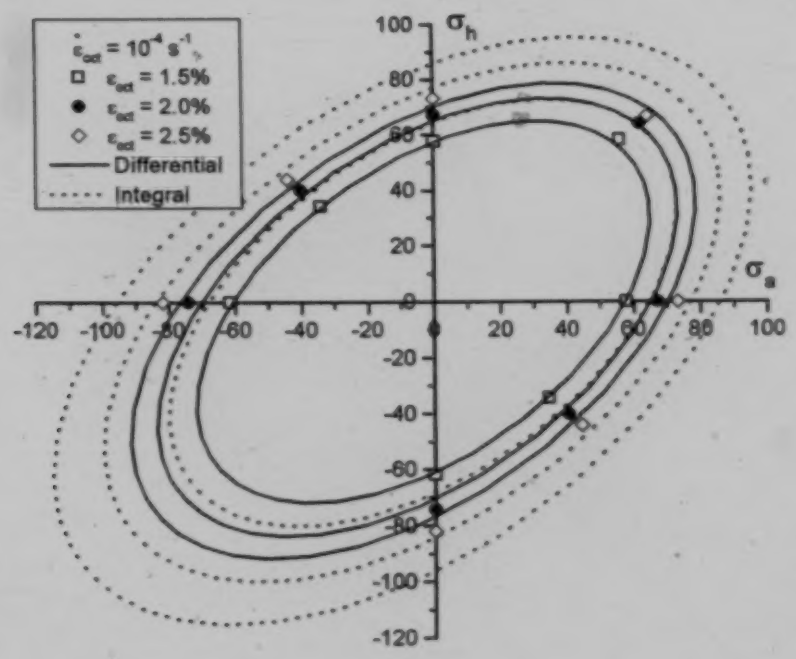

Fig.6.8 Comparison of the predicted stress envelopes by both the differential and integral models with the experimental data ($\varepsilon_{oct} = 1.5\%$, 2.0% and 2.5%)

6.2.3 Proportional loading paths

Figure 6.9 compares the experimental data of combined axial and shear proportional test at an octahedral shear strain rate of $10^{-5}\ s^{-1}$ with the predicted stress responses by the two models. It is seen that during the early loading, the predictions of both differential and integral constitutive models fit fairly well the experimental data. However, with the increase in stress level, the prediction by the differential model are in much better agreement with the experimental data than that of the integral model for both axial and shear stresses.

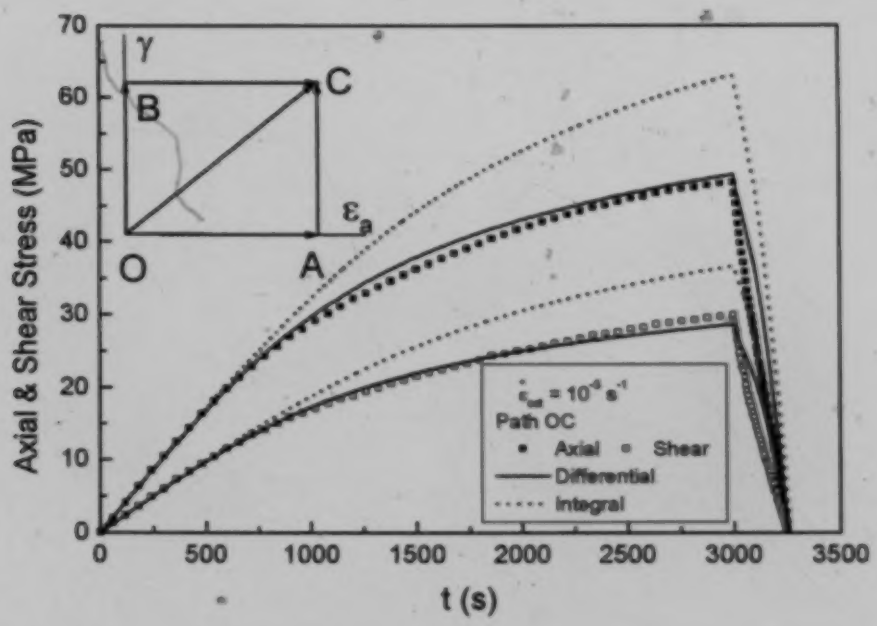

Figure 6.9 Comparison of combined axial-shear proportional test with the predicted stress responses by the two models ($\dot{\varepsilon}_{act} = 10^{-5}\ s^{-1}$)

6.2.4 Non-proportional loading paths

The predicted axial and shear stresses by the two models for the non-proportional paths OBC are compared with the experimental data as shown in Fig. 6.10. Again it is seen that the differential constititutive model predicts the stress responses which are very close to the experimental one while the prediction by the integral representation deviates significantly. At the proporitonal loading stage (Path OB) the integral model predicts a higher shear stress response and the same trend extends to the non-proportional stage (Path BC). In contrast, the predicted axial stress response is lower for the Path BC.

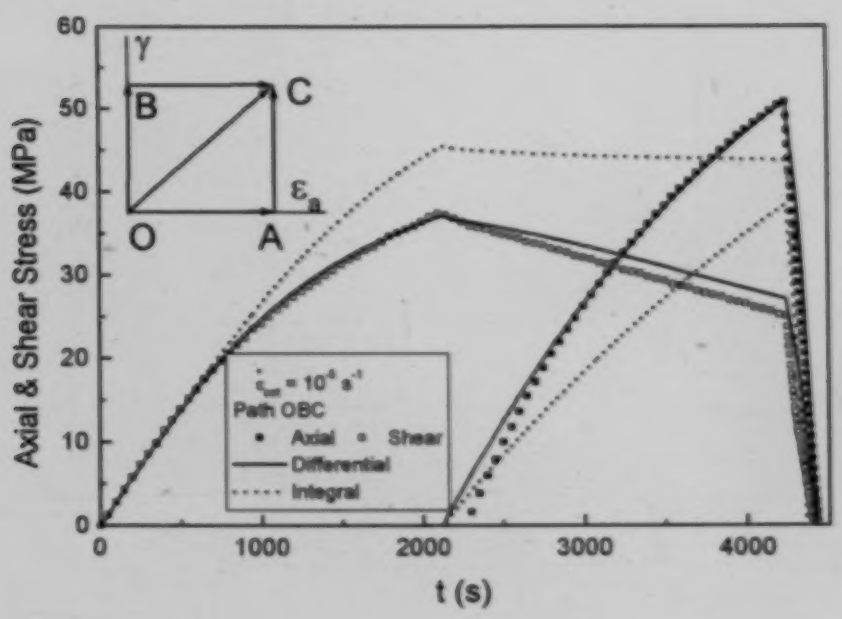

Fig. 6.10 Comparison of the experimental data for Path OBC with the predicted stress response by the two models ($\dot{\varepsilon}_{axl} = 10^{-5}\ s^{-1}$)

The predicted stress responses by the two models for another non-proportional paths OAC are shown in Fig. 6.11, together with the corresponding experimental data. The predicted trends for this loading path are similar to those shown in Fig.6.10, i.e., the different model predicts the stress variation very close to the experimental data while that predicted by the integral constitutive representation deviates significantly. In the axial loading stage (Path OA) the integral model predicted a higher axial stress response and that trend is also observed in the non-proportional path AC. A reversed trend is seen with respect to the predicted shear stress for the path AC, where the predicted values are lower than the experimental ones.

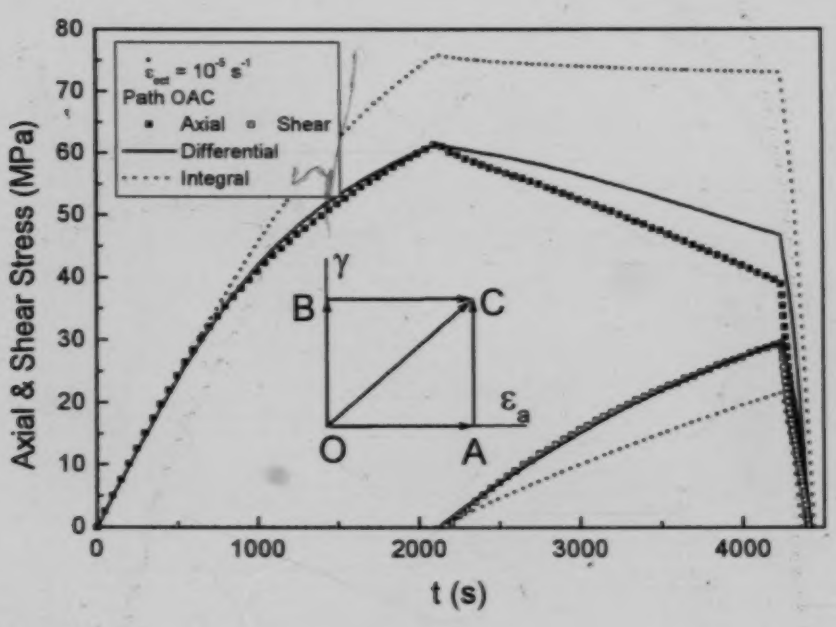

Fig. 6.11 Comparison of the experimental data for Path OAC with the predicted stress response by the two models ($\dot{\varepsilon}_{oct} = 10^{-5}\ s^{-1}$)

From the above comparison, it is clear that the predictions by the differential constitutive model are in good agreement with the experimental data, both qualitatively and quantitatively. However, in the case of the integral model, only a qualitative agreement is predicted. In summary, the differential model has a much better prediction capability of the deformation behavior of this epoxy resin compared to that of the integral one.

6.2.5 Transient loading paths

a. Uniaxial tensile loading with different strain rates

Figure 6.12 depicts the predictins for uniaxial tensile stress-strain curves at three different octahedral shear strain rates of $10^{-3}\ s^{-1}$, $10^{-4}\ s^{-1}$ and $10^{-5}\ s^{-1}$. The comparison of the

predictions with the experimental data shows that at low stress levels, the prediction by both the differential and integral models is close to each other and to the experiments. However, at high stress level, the integral model predicts much higher stress values. The prediction by the differential model is fairly good, especially for the two lower strain rates.

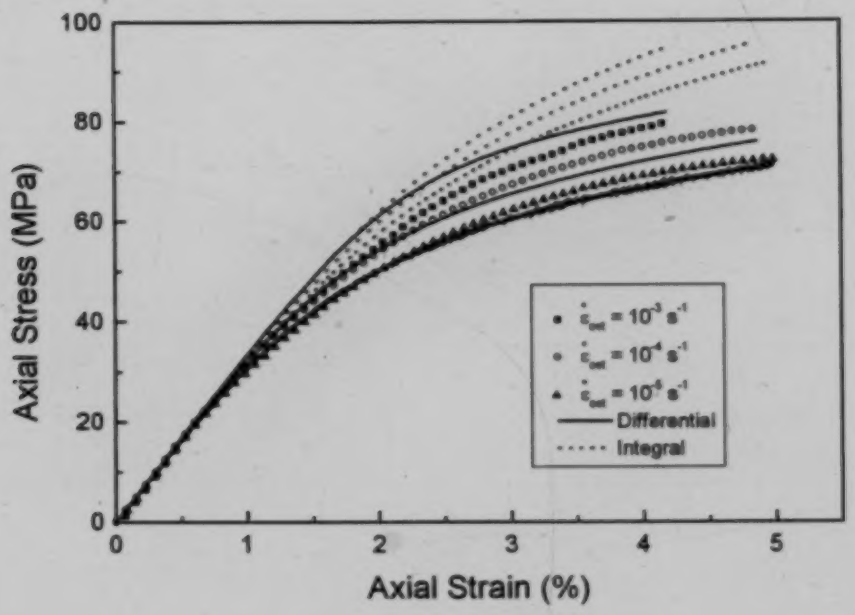

Fig.6.12 Comparison between the experimental and predicted tensile stress-strain curves to failure at three different octahedral shear strain rates ($10^{-3}\ s^{-1}$, $10^{-4}\ s^{-1}$ and $10^{-5}\ s^{-1}$)

b. Uniaxial Compressive loading with different stress/strain rates

The predictions for uniaxial compressive stress-strain curves at the same three octahedral shear strain rates as those for uniaxial tensile tests, are shown in Fig. 6.13. The similar trend with that of the uniaxial tensile loading is observed, i.e., at low stress levels, the prediction by both the differential and integral models is close to each other and to the

experiments. However, at high stress level, the integral model predicts much higher stresses. The prediction by the differential model is closer to the experimental data. However, both models cannot capture the yield and subsequent strain softening behavior of the experiments since there are no damage mechanisms included in both model formulations.

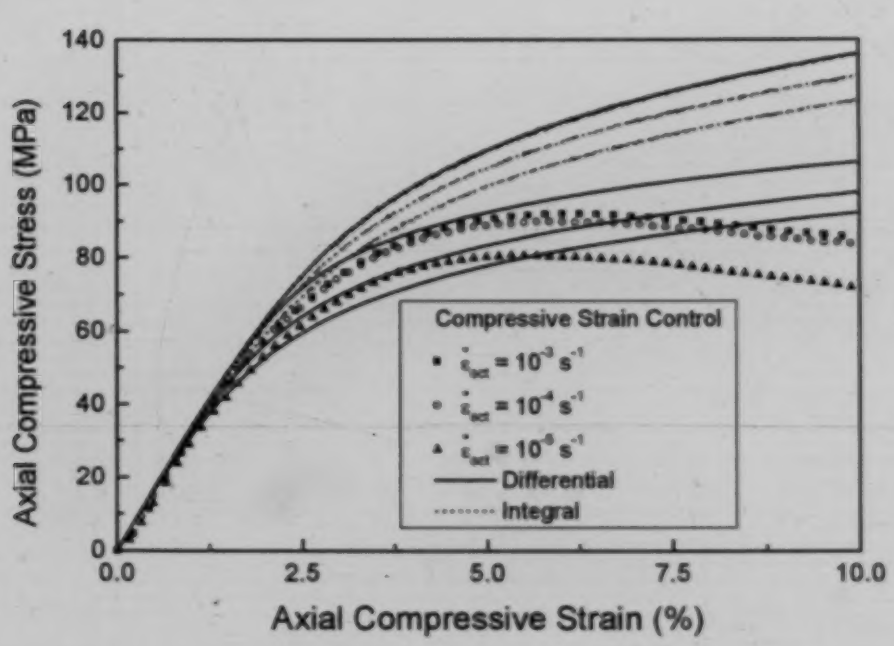

Fig.6.13 Comparison between the experimental and predicted compressive stress-strain curves to failure at three different octahedral shear strain rates ($10^{-3}\ s^{-1}$, $10^{-4}\ s^{-1}$ and $10^{-5}\ s^{-1}$)

Figure 6.14 shows the predictions for uniaxial compressive stress-strain curves similar to those shown in Fig.6.13. The only difference between these two figures is that the tests shown in this figure are all under stress controlled. The comparison of the predictions with the experimental data shows that although both models predict much lower strains at all

stress rates, their predictions are very close to the experimental data at low stress levels. At high stress level, the differential model predicts closer stress responses to the experiments.

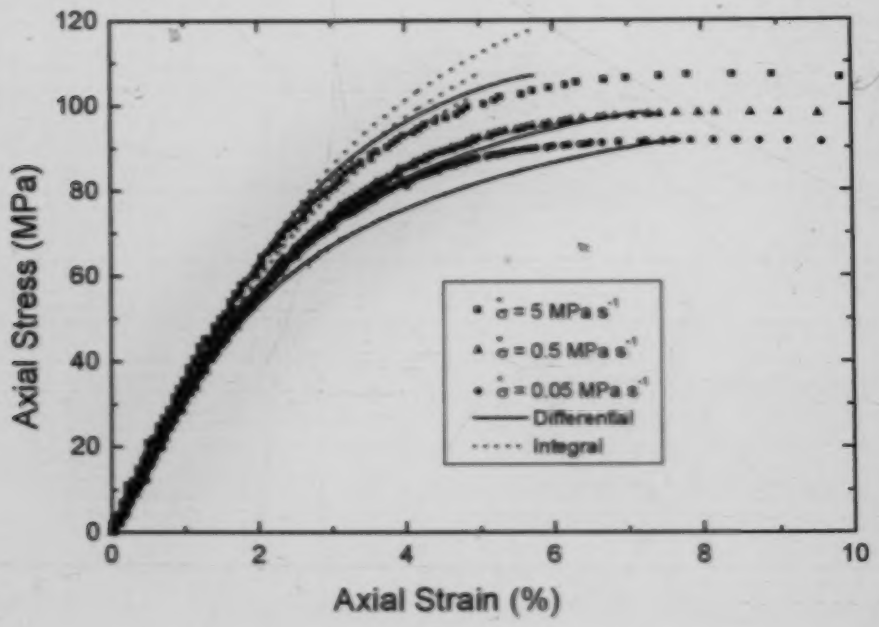

Fig.6.14 Comparison between the experimental and predicted compressive stress-strain curves to failure at three different stress rates (5MPa/s, 0.5MPa/s and 0.05MPa/s)

c. Pure shear loading with different strain rates

Figure 6.15 shows the predictions for pure shear stress-strain curves at three octahedral shear strain rates of $10^{-3}\ s^{-1}$, $10^{-4}\ s^{-1}$ and $10^{-5}\ s^{-1}$. The differential model predicts a very good agreement with the experimental data, especially at the two lower strain rates. The predictions for the three strain rates by the integral model are all higher than those of the experiments, especially at higher stress levels.

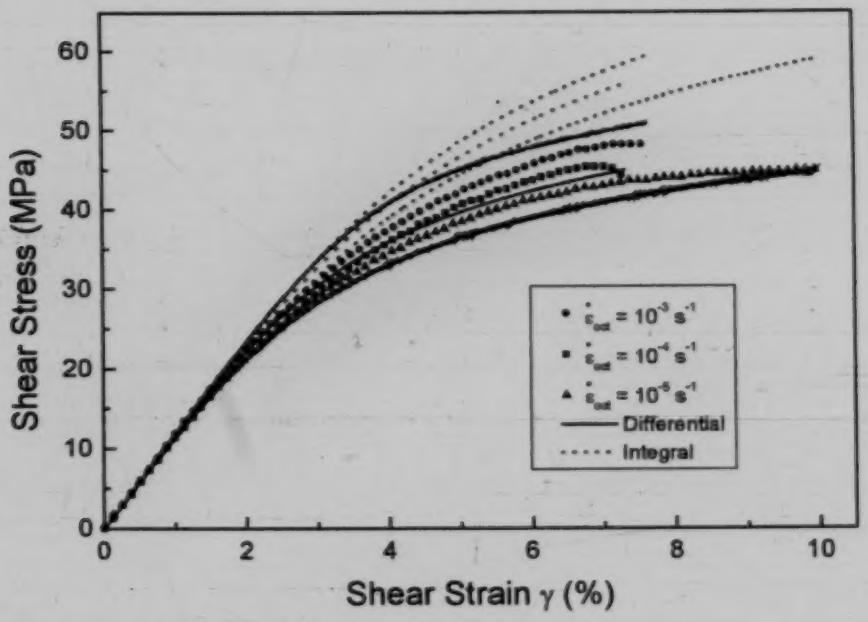

Fig.6.15 Comparison between the experimental and predicted shear stress-strain curves to failure at three different octahedral shear strain rates ($10^{-3}\ s^{-1}$, $10^{-4}\ s^{-1}$ and $10^{-5}\ s^{-1}$)

d. Equibiaxial tensile loading

For the equibiaxial loading case, the predicted axial and hoop stress responses for the octahedral shear strain rate of $10^{-3}\ s^{-1}$ are the same and collapse to one curve (Fig.6.16). Again the differential model predicts the experimental results better than the integral model. The integral model predicts much higher stress responses at high stress levels.

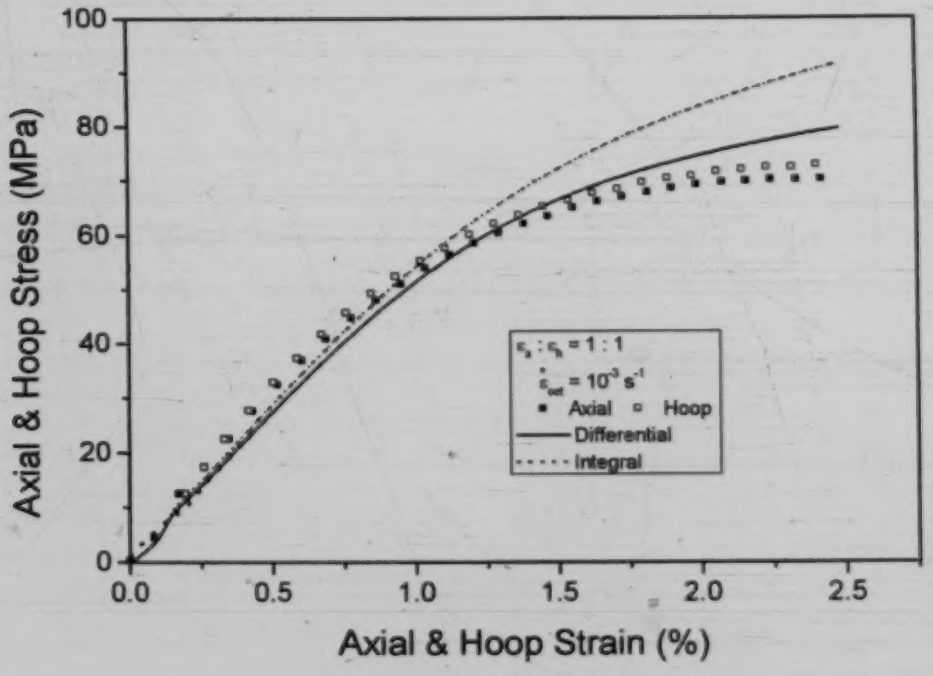

Fig.6.16 Comparison between the experimental and predicted equibiaxial stress-strain curves to failure at an octahedral shear strain rate of $10^{-3}\ s^{-1}$

From the above comparison, it is clear that both models can accurately predict the deformation behavior at low stress levels. With the increase in stress level, the predicted values by the two models are different from each other. In general, the integral model tends to overestimate the stress responses for the strain-controlled tests and underestimate the strain responses for the stress-controlled tests. The predictions by the differential model are in very good agreement with the experimental data for most loading cases, even at very high stress level. However, neither models can accurately predict the yield behaviors shown in the uniaxial compressive tests. This may be partially attributed to the occurrence

of damage in the material which is not included in the current models. As the stress increases, damage may develop and, therefore, the stiffness may decrease.

6.2 Unloading Behavior

In the following, the ability of the current differential model to predict the unloading behavior by using the newly proposed rule for the modulus E_1, is examined. For the sake of comparison, the results of the differential model with the same loading modulus function for both loading and unloading cases are also presented for the uniaxial tensile cases. The predictions by the integral model are included as well for the same purpose.

6.3.1 Uniaxial tensile loading-unloading

The predicted unloading behavior for the uniaxial tensile test with an octahedral shear strain rate of $10^{-5}\ s^{-1}$ is shown in Fig.6.17. This figure reveals that the strong nonlinear and viscoelastic response of the material is well predicted over the complete range of the test program. It is to be noted that the prediction of the unloading branch deviates significantly, if the same modulus function is applied in the differential model without distinguishing between loading/unloading cases, see dotted line in Fig.6.17. The prediction of the integral model is much higher than that of the experimental data and a wrong trend is predicted.

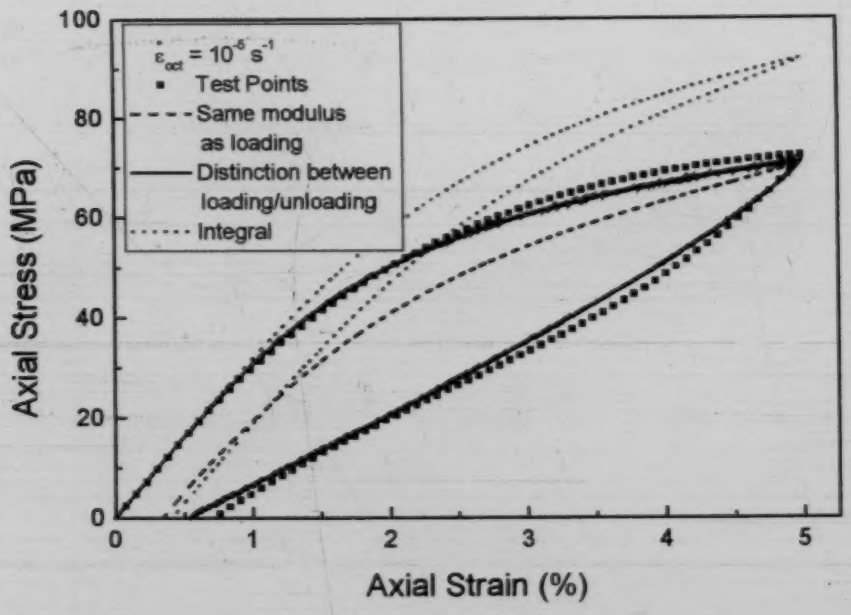

Fig.6.17 Comparison between the experimental and predicted loading-unloading curve for the octahedral shear strain rate of $10^{-5}\ s^{-1}$

6.3.2 Proportional loading/unloading along Path O-C-O

The predicted behavior for proportional path O-C-O with an octahedral shear strain rate of $10^{-5}\ s^{-1}$ is shown in Fig.6.18. It is noted that the proposed model can predict fairly well the biaxial (axial/shear) loading/unloading behavior of the proportional path O-C-O. The prediction of the integral model is much higher than that of the experimental data and, again, a wrong trend is predicted.

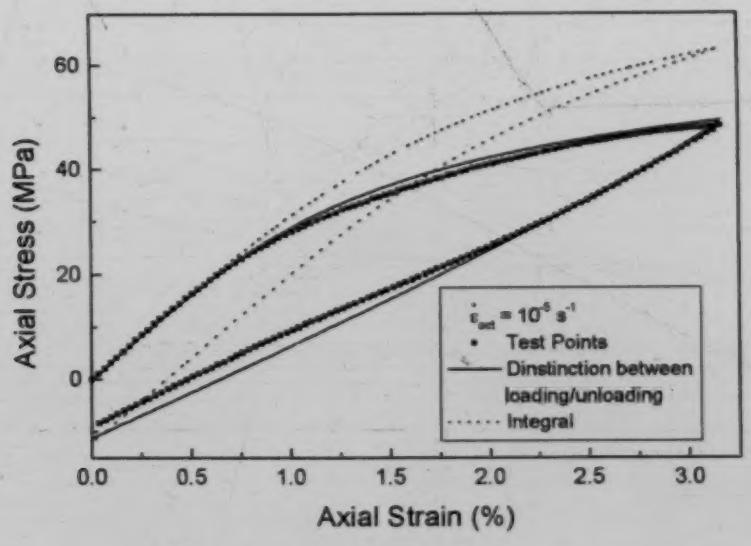

(a)

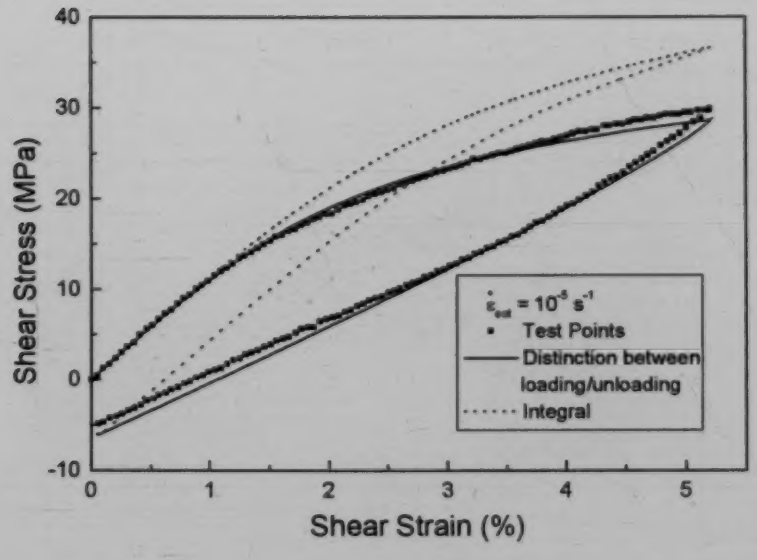

(b)

Fig.6.18 Comparison between the experimental and predicted loading-unloading curves for proportional Path O-C-O (a) Axial, (b) Shear

6.3.3 Non-proportional loading/unloading path

Figure 6.19 shows the current differential model prediction for both the axial and shear unloading behavior of the non-proportional path O-B-C-O. Similar trend is observed for the non-proportional path O-A-C-O as shown in Fig.6.20. It is seen that the loading/unloading response is well predicted, both qualitatively and quantitatively, by the new model. The predicted curves by the integral model for all non-proportional loading conditions deviates from the experimental data, especially in the high stress ranges, and the wrong trend is predicted again.

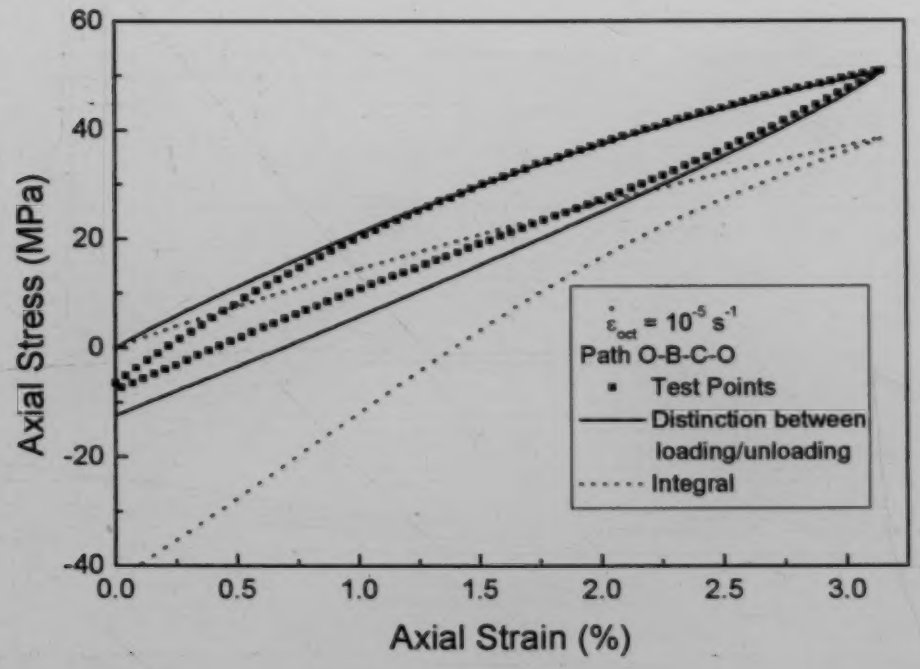

(a)

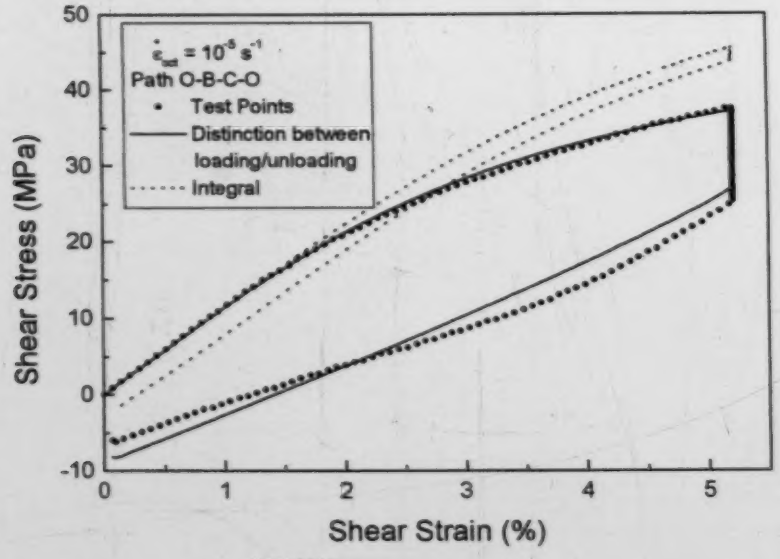

(b)

Fig.6.19 Comparison between the experimental and predicted loading-unloading curves for non-proportional Path O-B-C-O (a) Axial, (b) Shear

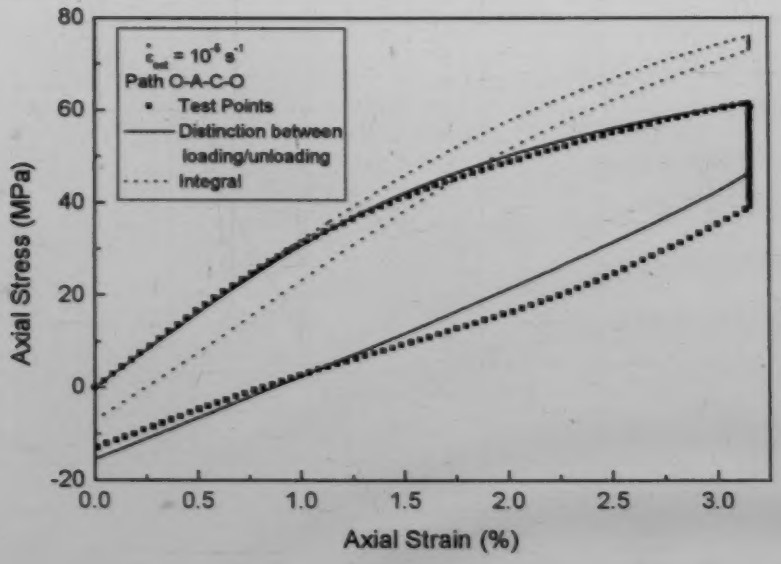

(a)

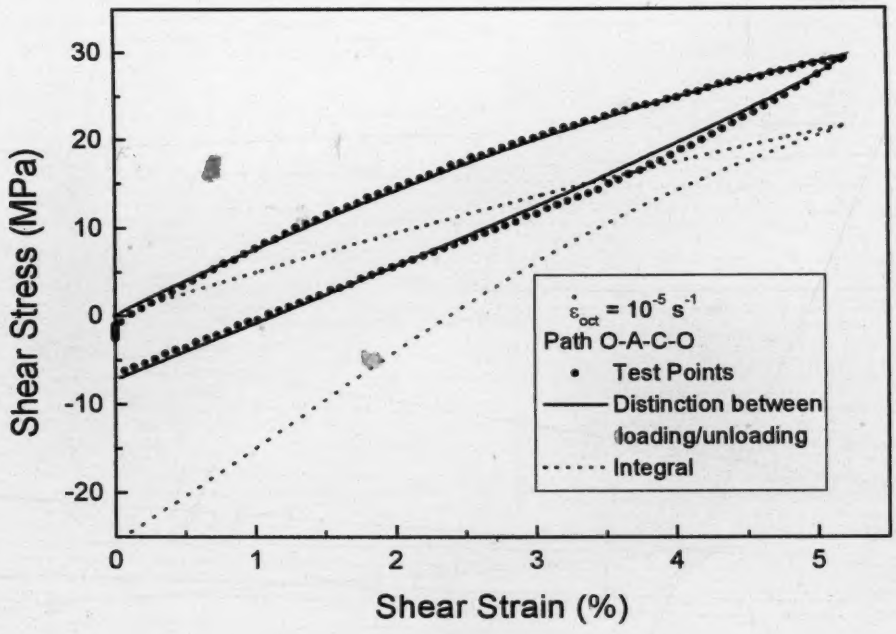

(b)

Fig.6.20 Comparison between the experimental and predicted loading-unloading curves for non-proportional Path O-A-C-O (a) Axial, (b) Shear

6.3 Concluding Remarks

The predictions from the differential viscoelastic constitutive model has been compared with the results of a comprehensive experimental investigation data of EPON 826 epoxy polymer including creep, recovery, various transient loading/unloading paths and multiaxial proportional or non-proportional paths. The Lai and Bakker model is also included for a comparative purpose. The comparison results show:

- Both models are very successful in predicting the tensile creep and recovery responses, from which the material constants and functions are calibrated.

- Both models can also accurately predict the deformation behavior at low stress levels. With the increase in stress level, the predicted values by the two models deviate from each other. In general, the integral model tends to overestimate the stress responses for the strain-controlled tests and underestimate the strain responses for the stress-controlled tests. The predictions by the differential model are in very good agreement with the experimental data for most loading cases, even at very high stress levels.
- Neither models can accurately predict the yield behaviors shown in the uniaxial compressive tests. This can be partially attributed to the occurrence of damage in the material which is not included in the current models. As the stress increases, damage may develop and, therefore, the stiffness may decrease.
- The newly proposed loading/unloading criterion and the simple unloading rule for E_1 can capture the unloading deformation features of the EPON 826 epoxy resins.
- The differential model predictions are in very good agreement with the experimental results not only qualitatively but also *quantitatively*.

Chapter 7

Model Predictions for the Mechanical Behavior of ColdCure Epoxy System

Both the differential and integral models were used to predict the deformation behavior of EPON 826/EPI-CURE 9551 epoxy system in the previous chapter. It was seen that the newly proposed differential model was capable of predicting the deformation behavior of the epoxy system. In this chapter, the predictive capability of the two constitutive models is further checked against the ColdCure epoxy system. As indicted in Chapters 3 and 4, the ColdCure epoxy is different in certain aspects from EPON 826, e.g., much lower strength and stiffness, much smaller failure strains and a bigger hydrostatic stress effect. These differences clearly indicate that the ColdCure epoxy has different deformation characteristics from those of the EPON 826. The predictions of the differential model are compared with the experimental results reported in Chapter 4. The predictions by the modified integral model by Lai and Bakke are also included for the comparative purpose.

7.1 Model Constants and Functions

Following the procedures described in Chapter 5, the material constants and functions for the two models were calibrated. The same procedure for the calibration of the material constants and functions as explained in Chapter 6 was followed for the ColdCure epoxy. The material constants and functions thus determined are listed as follow:

7.1.1 Differential model

Among the five material constants (E, υ, α, τ_1, R) and the function form of $E_1(\sigma_{eq})$ to be determined for the ColdCure epoxy, E, $E_1(\sigma_{eq})$ and τ_1 are determined from fitting eq. (5.11) with the experimental creep curves at different stress levels as shown in Fig.4.1. The Poisson's ratio, υ, is assumed to be 0.4, instead of being determined from experiments as for EPON 826. α is taken to ten, and six Kelvin (Voigt), together with one spring in series, were chosen to simulate the deformation behavior of the ColdCure epoxy resin. R was determined by comparison of a uniaxial tensile curve with that of a compressive one (Fig.4.10 and 4.11).

The five material constants and one modulus function for the differential constitutive model were calibrated as follow:

$$E = 2755MPa,\ \upsilon = 0.4,\ \alpha = 10,\ \tau_1 = 657.895s,\ R = 1.08,\ \text{and}$$

$$E_1(\sigma) = \begin{cases} 12245.6 - 432.6\sigma + 4.49\sigma^2\ (MPa) & \sigma \geq 27.5MPa \\ 3744.7 - 75.7\sigma\ (MPa) & \sigma \leq 27.5MPa \end{cases} \tag{7.1}$$

7.1.2 Integral model

The creep-recovery curves shown in Fig.4.1 are used to characterize the three material constants (D_0, D_1, n) and four nonlinear functions (g_0, g_1, g_2, a_σ) for the integral representation. The constants and function relations thus obtained for the EPON 826 epoxy are listed in Table 7.1.

Table 7.1 nonlinear viscoelasticity parameters for integral model

$D_0 = 3.556\times10^{-4}(MPa)^{-1}$, $D_1 = 7.118\times10^{-6}(\text{MPa})^{-1}$, $n = 0.373$
$g_0 = 1$
$g_1 = \begin{cases} 1 & for\ \sigma_{eq} \le 11.293MPa \\ 0.505 + 0.0438\sigma_{eq} & for\ \sigma_{eq} > 11.293MPa \end{cases}$
$g_2 = -2.066 + 3.066e^{\frac{\sigma_{eq}}{65.5}}$
$a_\sigma = \begin{cases} 1 & for\ \sigma_{kk} \le 12.74MPa \\ 1.611 - 0.048\sigma_{kk} & for\ \sigma_{kk} > 12.74MPa \end{cases}$

7.2 Comparison of Predicted Results with Experiments

7.2.1 Creep and recovery behavior

The creep and recovery curves predicted by the two constitutive representations are compared with the experimental data as shown in Figs 7.1 and 7.2, respectively. It can be seen that the agreement is fairly good. In general, the predictive capability for the creep behavior is better than that of the recovery. The predictive accuracy also deteriorates at higher stress levels probably because damage may be introduced at high stress levels.

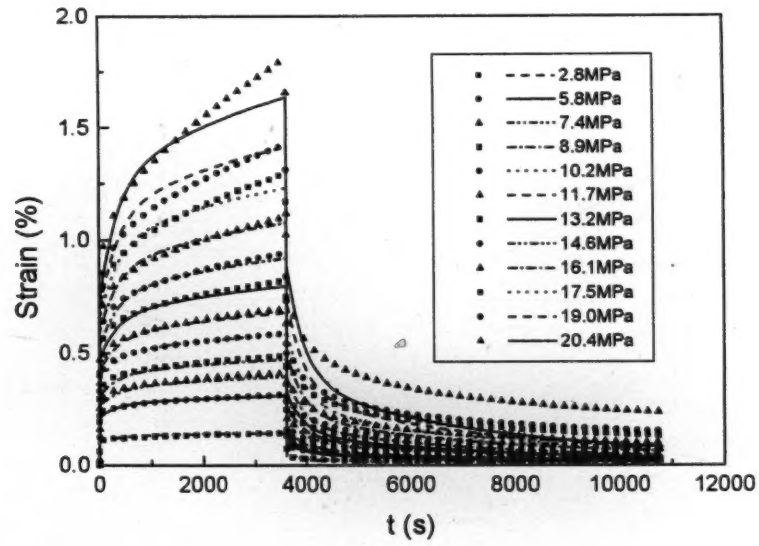

Fig.7.1 Comparison of experimental data with predicted creep-recovery curves by the differential constitutive model

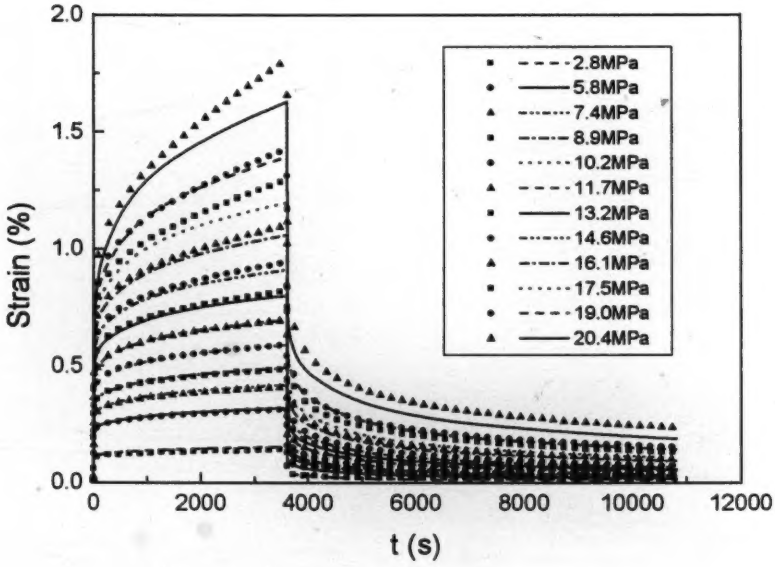

Fig.7.2 Comparison of experimental data with predicted creep-recovery curves by the integral constitutive model

For other loading conditions, the prediction on the equi-biaxial creep behavior by the two models is checked against the experimental data. Two stress levels of 6.3 MPa and 10.5 MPa are utilized as shown in Fig.7.3. Both models are in good agreement with the test data at the lower stress level of 6.3 MPa, but at the higher applied stress level of 10.5 MPa, the predicted values are much lower than the experimental data.

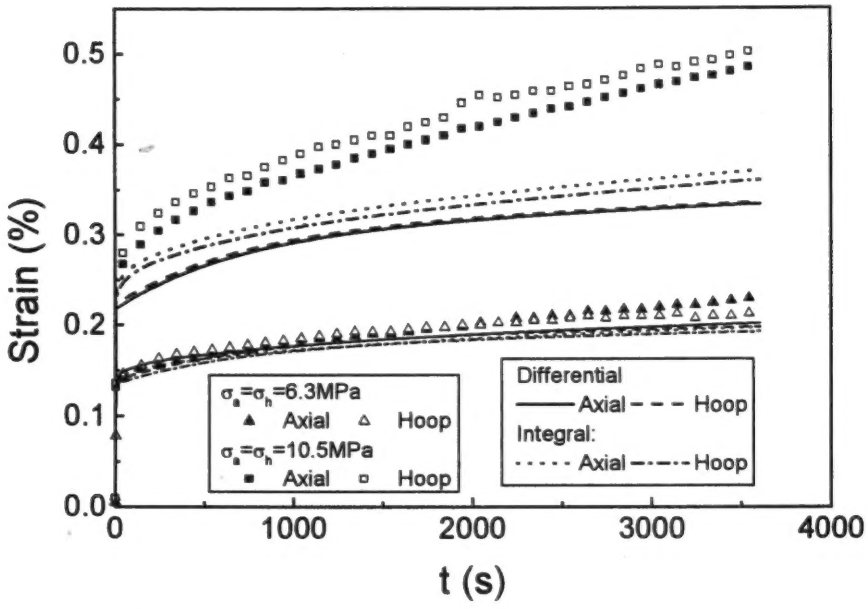

Fig.7.3 Model predictions of equibiaxial creep deformation for two stress levels

7.2.2 Hydrostatic stress effect

The predictive capbility of the two models on the hydrostatic stress effect is explored by two sets of predictions versus experimental data. In the first set, the creep behavior of two different combinations of axial and shear stressse is predicted. The second set includes the prediction of the shear creep behavior with or without a superimposed hydrostatic pressure.

a) Shear creep under combined axial and shear stresses

The predicted shear creep deformations at two different combinations of axial and shear stresses by the two models are shown in Fig 7.4, along with the experimental data. Generally, the predictions by the two models are only in qualitative agreement with the experimental results. Quantatively, the predicted creep curves by the two models overestimate the exprimental results. It is also observed that the two representations do predict a hydrostatic stress effect as seen in Fig.7.4, where the predicted shear creep deformation curves are influenced by the superimposed axial stresses.

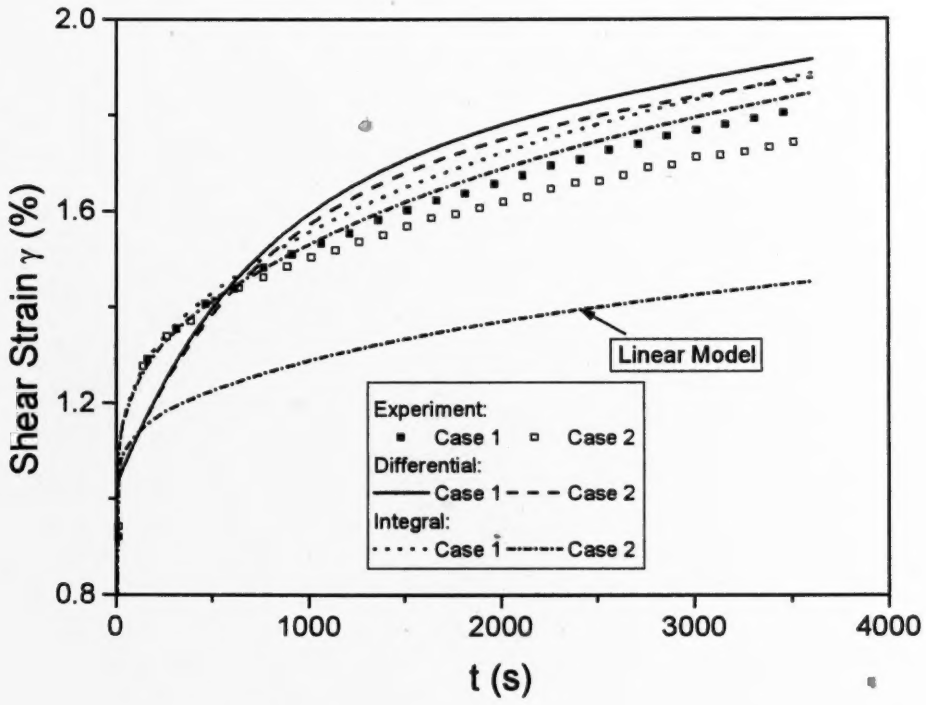

Fig.7.4 Model predictions on shear creep for two axial stress cases:

Case 1: $\tau = 10\,\text{MPa}$, $\sigma_a = 14\,\text{MPa}$; Case 2: $\tau = 10\,\text{MPa}$, $\sigma_a = -14\,\text{MPa}$

Also included in this figure is the prediction from linear viscoelastic theory. The linear model cannot distinguish the difference between the two loading cases. The predicted creep deformations by the two models are significantly different from the linear prediction, therefore, the two models do predict nonlinear characteristics.

b) Hydrostatic pressure effect

The prediction on shear creeps under constant shear stresses with or without a superimposed hydrostatic pressure is shown in Fig.7.5. The prediction by the two models is also in qualitative agreement with the experimental results. Both the differential model and the integral model predict two different curves and, therefore, have the hydrostatic pressure effect predictive capability.

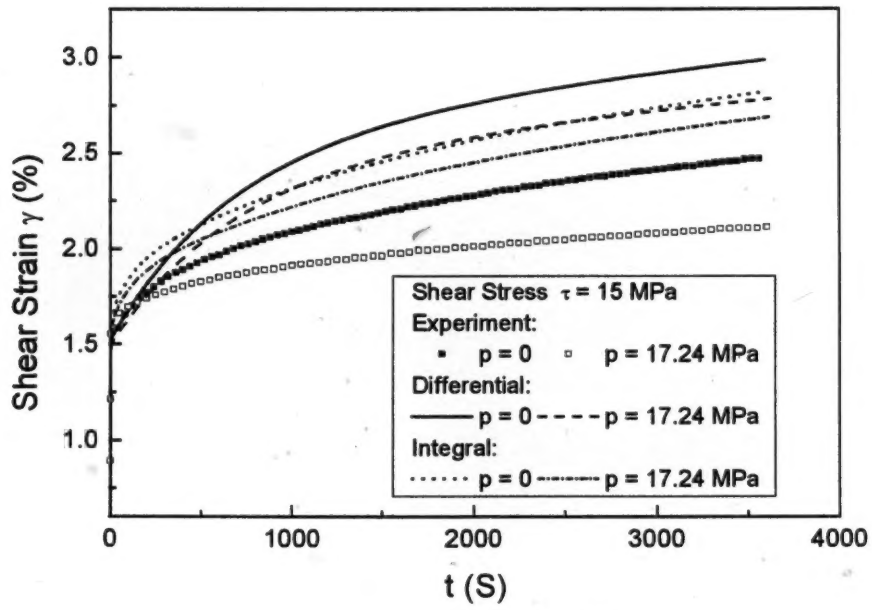

Fig.7.5 Model predictions on shear creep with or without hydrostatic pressure p

7.2.3 Multiaxial behavior

a) Stress envelopes at different strain rates

The predicted stress envelopes for a fixed octahedral shear strain of ε_{oct}=0.4% at two different strain rates of $10^{-3}\ s^{-1}$ and $10^{-5}\ s^{-1}$ are depicted in Fig.7.6. The stress envelopes predicted by both the differential and the integral models agree fairly well with the experimental data in the first, second and fourth stress quadrants, especially for the higher strain rate of $10^{-3}\ s^{-1}$. In the third quadrant a significant deviation is observed for both models.

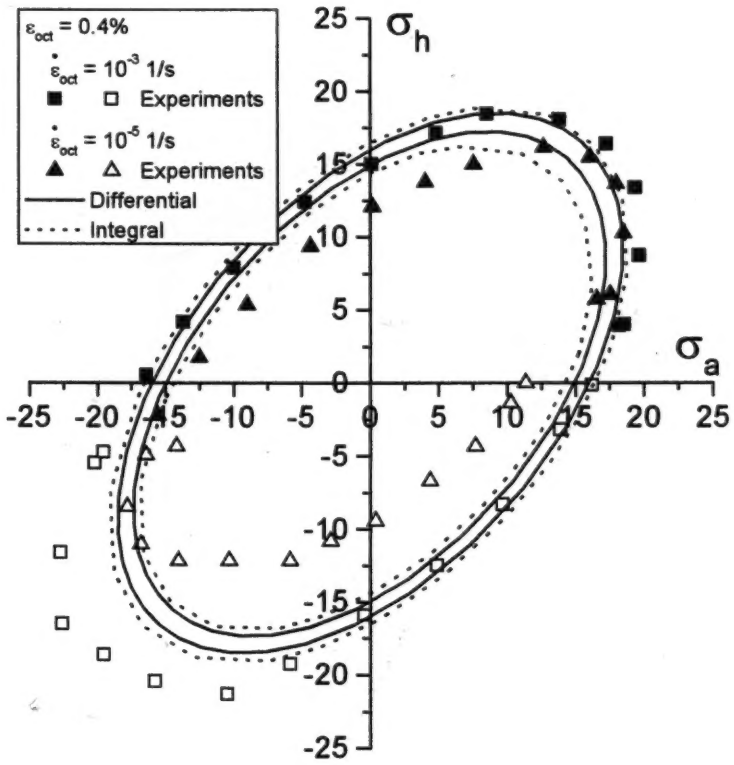

Fig.7.6 Comparison of the predicted stress envelopes by both the differential and integral models with the experimental data (ε_{oct}=0.4%)

b) Stress envelopes at different octahedral shear strains

The predicted stress envelopes for two different octahedral shear strains of ε_{oct}=0.4% and ε_{oct}=0.8% at an octahedral shear rate of $10^{-4}\ s^{-1}$ are shown in Fig.7.7. The stress envelopes predicted by the two constitutive representations fit the experimental data very well for the octahedral shear strain of 0.4% while a higher prediction than the experimental data is noted for the octahedral shear strain rate of 0.8%.

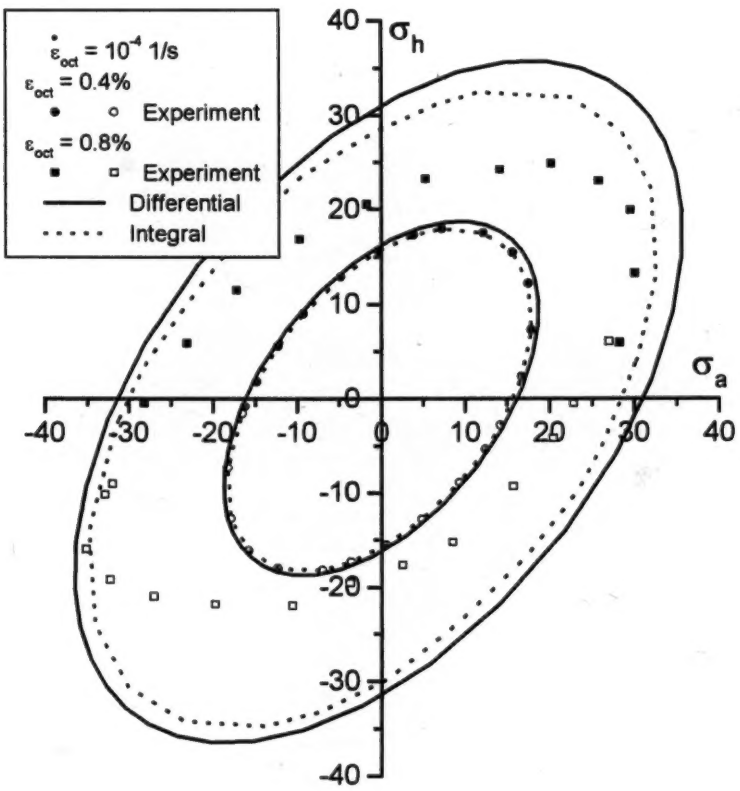

Fig.7.7 Comparison of the predicted stress envelopes by both the differential and integral models with the experimental data ($\dot{\varepsilon}_{oct}$=$10^{-4}\ s^{-1}$)

7.2.4 Transient loading paths

a) Uniaxial tensile

Figure 7.8 shows the predictions for uniaxial tensile stress-strain curves at the octahedral shear strain rate of $10^{-4}\ s^{-1}$. The comparison of the predictions with the experimental data shows that at low stress levels, the prediction by both the integral and differential models is close to each other and also to the experiments. However, at high stress level, both the differential and integral models predict a higher stress response.

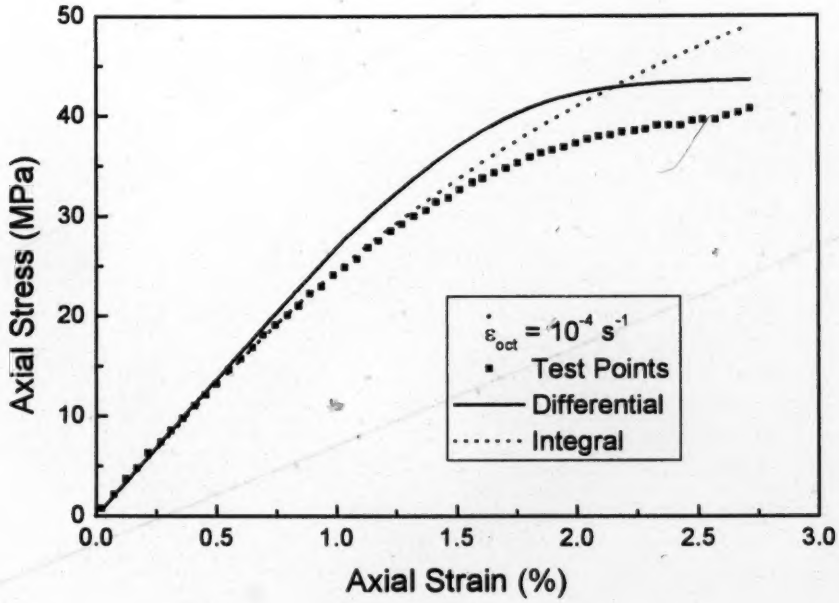

Fig.7.8 Comparison between the experimental and predicted tensile stress-strain curve at the octahedral shear strain rate of $10^{-4}\ s^{-1}$

b) Pure shear

Figure 7.9 shows the predictions for pure shear stress-strain curves at the octahedral shear strain rate of $10^{-4}\ s^{-1}$. The prediction for the the strain rate by both the differential and

integral models are much higher than that of the experiment, especially at higher stress levels.

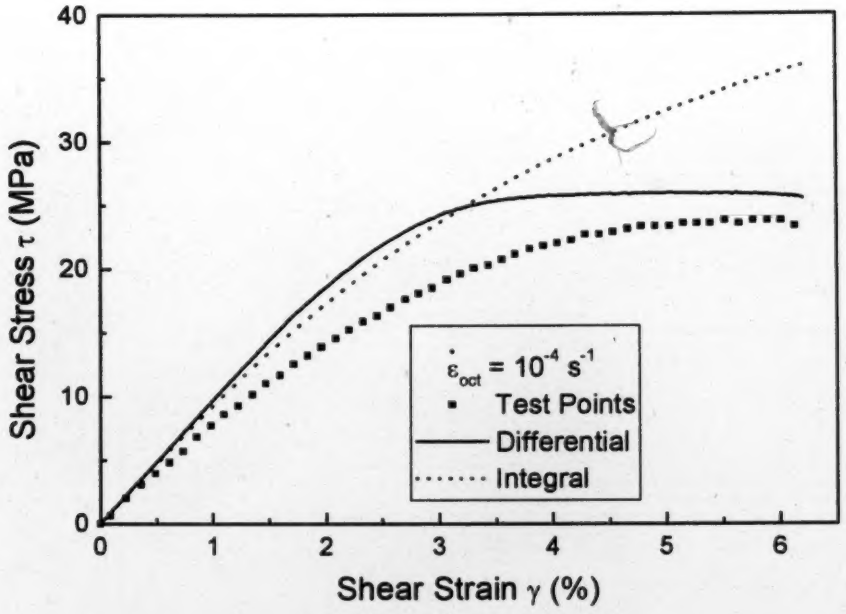

Fig.7.9 Comparison between the experimental and predicted shear stress-strain curve at the octahedral shear strain rate of $10^{-4}\ s^{-1}$

c) Equibiaxial with different strain rates

Figure 7.10 depicts the equibiaxial stress – strain curves at two octahedral shear strain rates of $10^{-4}\ s^{-1}$ and $10^{-5}\ s^{-1}$. For the equi-biaxial loading cases, the predicted axial and hoop stress responses for each strain rate are the same and collapse to one curve. From this figure it is observed that the integral model predicts fairly well with the experiments for the two tested strain rates while the differential model has a higher stress prediction, especially at the higher stresses.

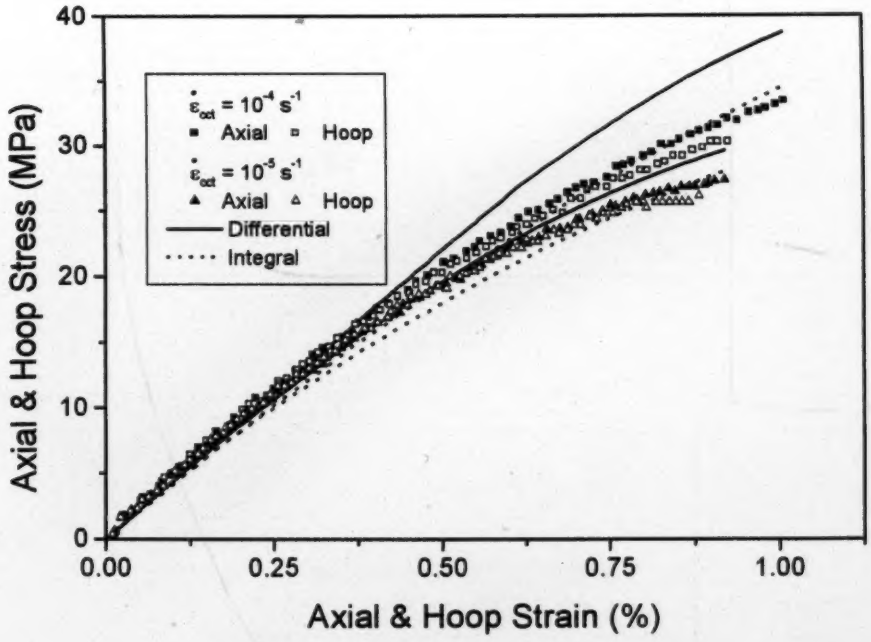

Fig.7.10 Comparison between the experimental and predicted equibiaxial stress-strain curves at two different octahedral shear strain rates ($10^{-4}\ s^{-1}$ and $10^{-5}\ s^{-1}$)

7.2.5 Non-proportional loading paths

a) Strain-controlled tests

The predicted axial and shear stress – strain curves by the nonlinear models for the two non-proportional strain paths at the octahedral shear strain rate of $10^{-4}\ s^{-1}$ are depicted in Figs 7.11 and 7.12, respectively. The predictions by both models are only in qulitative agreement for axial and shear stress responses.

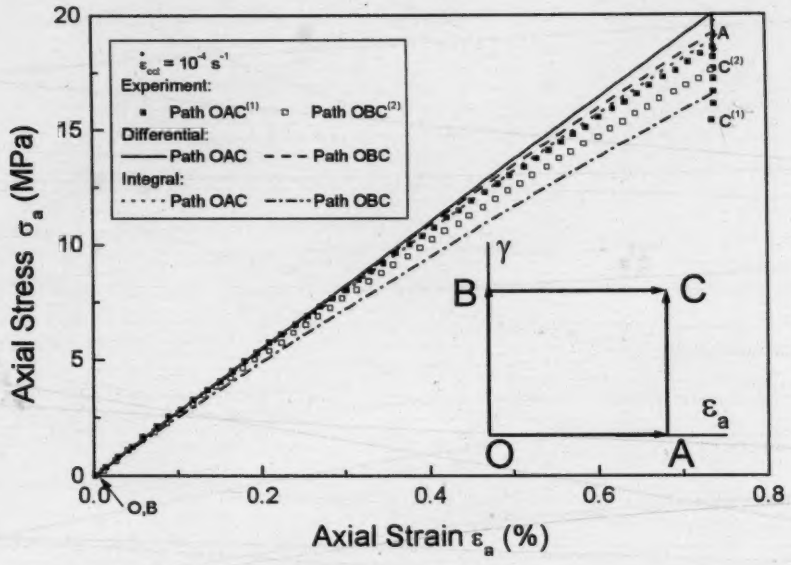

Fig.7.11 Experimental and predicted axial stress-strain curves for two different loading paths with an octahedral shear strain rate of $10^{-4}s^{-1}$

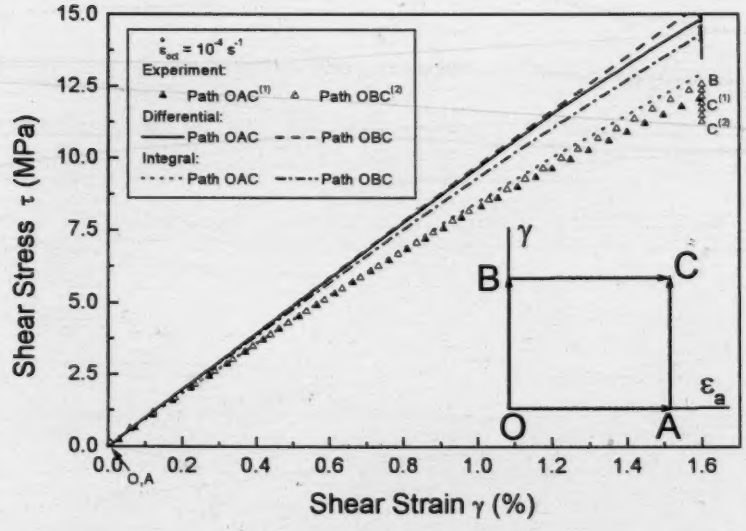

Fig.7.12 Experimental and predicted shear stress-strain curves for two different loading paths with an octahedral shear strain rate of $10^{-4}s^{-1}$

b) Strain rate effect

The differential model predictions for the axial and shear stress – strain curves for the paths $\overline{OAC}$ and $\overline{OBC}$ at two octahedral shear strain rates of $10^{-4}s^{-1}$ and $10^{-5}s^{-1}$ are shown in Figs 7.13 and 7.14, respectively, and the integral model predictions for the same paths shown in Figs 7.15 and 7.16, respectively. It is noted that an increased stiffness is predicted with the increase in the octahedral shear strain rate, which qualitatively agrees with the experimental results.

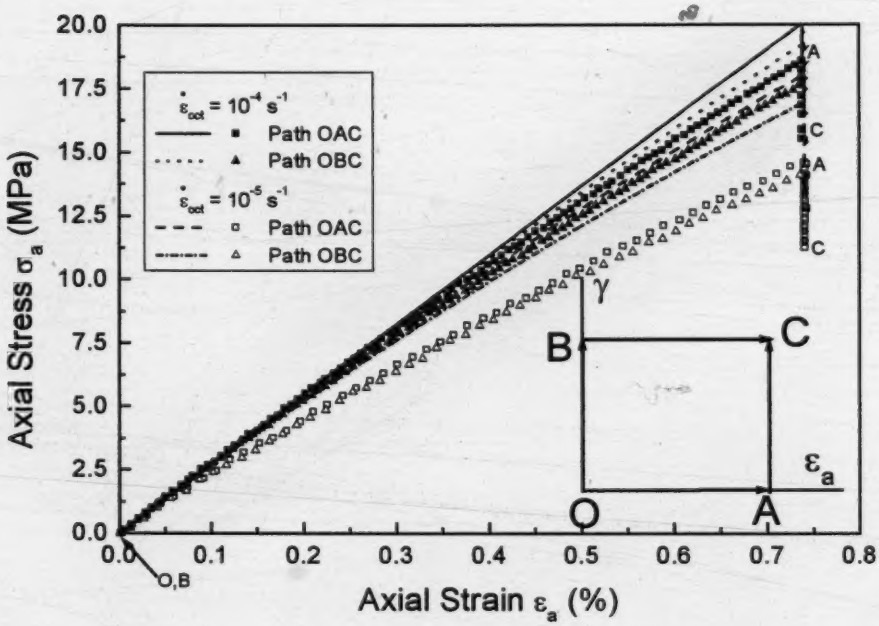

Fig. 7.13 Experimental axial stress-strain curves and predictions by differential model for two different loading paths at two octahedral shear strain rates of $10^{-4}s^{-1}$ and $10^{-5}s^{-1}$

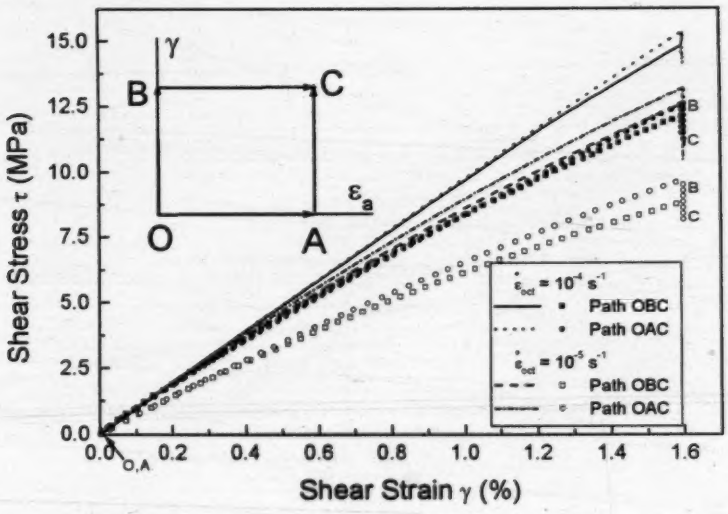

Fig. 7.14 Experimental axial stress-strain curves and predictions by differential model for two different loading paths at two octahedral shear strain rates of $10^{-4}s^{-1}$ and $10^{-5}s^{-1}$

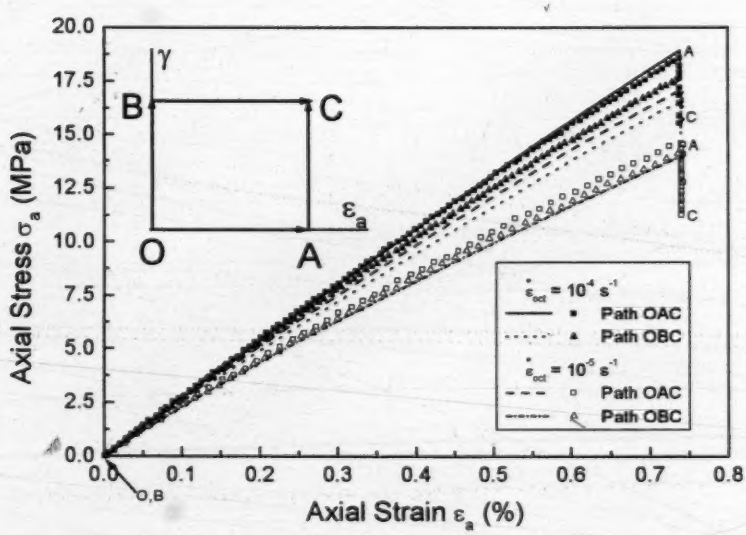

Fig. 7.15 Experimental axial stress-strain curves and predictions by integral model for two different loading paths at two octahedral shear strain rates of $10^{-4}s^{-1}$ and $10^{-5}s^{-1}$

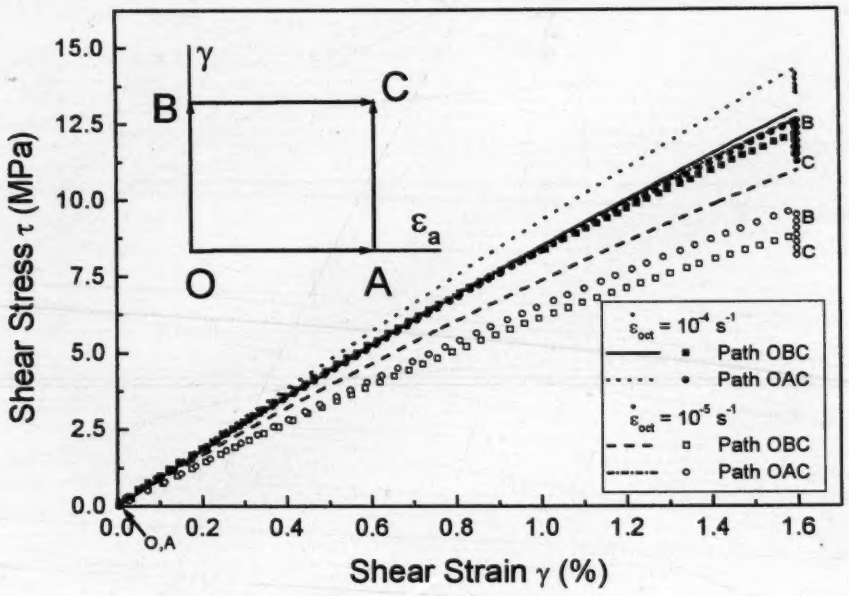

Fig. 7.16 Experimental axial stress-strain curves and predictions by integral model for two different loading paths at two octahedral shear strain rates of $10^{-4}s^{-1}$ and $10^{-5}s^{-1}$

7.3 Concluding Remarks

The deformation behavior of the ColdCure epoxy system is simulated by the differential model. The deformations used for the model evaluation include uniaxial creep (and subsequent recovery), equibiaxial creep, creep under combined axial-shear stresses, creep under hydrostatic pressure, multiaxial deformations, transient loading, as well as non-proportional deformations. These tests are used to check the predictive capability of the differential model in four aspects, i.e., nonlinear viscoelastic behavior, hydrostatic stress effect, multiaxial behavior and loading history effect.

From the comparison between the test results and the differential model predictions, it can be concluded that the model can predict qualitatively all the features of the deformation behavior of the ColdCure epoxy system. Quantitative agreement between the predicted values and the experimental data is observed for some loading cases, especially at lower stress levels. The prediction deteriorates at high stress levels.

The integral model shows similar predictive capability to that of the differential model, i.e., the deformation features of the tested epoxy can be captured qualitatively by the integral model while quantitative agreement was only obtained for some loading cases.

Two reasons may explain the difference between the prediction and the experimental data. One reason is attributed to the different batches of the ColdCure epoxy resin used in these experiments. Since the material properties of polymers are strongly dependent on their production processes, the produced material at different runs may have different properties. The other reason could be attributed to the air bubbles inside the specimens. The superior low temperature curing property of the ColdCure epoxy may be an advantage in some engineering applications, however, it prevents air bubbles from escaping due to the higher viscosity of the solution. Trapped air bubbles change the microstructures of cured products and causes variations in material properties from specimen to specimen, even from the same batch.

Chapter 8

Conclusions

The focus of this dissertation has been on the deformation behavior and its constitutive modeling of epoxy resins. Special attention has been paid to the multiaxial nonlinear viscoelastic behavior of two epoxy systems: EPON 826/EPI-CURE 9551 and ColdCure epoxy (EPON 826). EPON 826/EPI-CURE 9551 is designed as a matrix material for composites and, therefore, requires high strength and toughness. ColdCure epoxy system has excellent curing capability even at very low temperature and is mainly used as a structural adhesive.

The mechanical behavior of these two epoxy resins under various loading schemes was investigated and the deformation features were analyzed. The failure behavior of the two epoxy systems was also studied and the failure characteristics were discussed. A differential constitutive model was developed to predict the observed features. Through extensive experimental investigations and the corresponding constitutive modeling, a better understanding of the mechanical behavior of polymers has been achieved, and a powerful analysis tool -- the nonlinear viscoelastic constitutive model has been developed.

8.1 Mechanical Behavior

The mechanical behavior of the two epoxy resin systems was investigated by carrying out extensive experiments under various loading conditions. The typical features include:

- The two epoxy resin systems showed strong nonlinear viscoelastic behavior with its manifestation in time effect, full recovery after deformation at not very high stress levels, and the stress dependence of the creep compliance above certain stress levels. If the materials are unloaded prior to failure, the unloading behavior for both epoxies is significantly different from their loading behavior. When the applied stress is high enough, the materials experience the entire three stages of creep deformation, i.e., creep at a decreasing rate; then at a nearly constant rate; and finally at an increasing rate and terminate in fracture.

- Hydrostatic component of stress does not have significant influence on the deformation behavior of EPON 826 at a hydrostatic pressure level up to 17.24 MPa. In contrast the ColdCure epoxy shows strong hydrostatic stress dependence. These tests indicate that EPON 826 has a very compact structure, while the molecular arrangement for ColdCure epoxy is loose with relatively larger free volume.

- A multiaxial stress state also changes the deformation behavior of the two epoxy resins and shifts the stress envelopes along the equibiaxial compressive stress direction in the stress space. The multiaxial deformation characteristics indicate that von Mises equivalent stress criterion is no longer valid. A Stassi equation was found to describe the multiaxial behavior of the two epoxy resins fairly well. The Stassi equation is different from the von Mises one in that it includes a compression-to-tension ratio and a hydrostatic stress term.

- A normal (shear) stress influences the shear (normal) stress-strain behavior of both the EPON 826 and ColdCure epoxy. The presence of a normal (shear) stress reduces the shear (normal) stress that can be sustained, or the stiffness decreases due to the presence of a second stress component. The above common phenomenon indicates the strong nonlinear and loading history dependent characteristics of the two epoxy systems.

- Both the epoxy resins share the same failure modes: brittle fracture or ductile yielding, and the failure modes are same for the same stress state. Brittle fracture occurs where hydrostatic stress is high while ductile yielding takes place where low or negative hydrostatic stress is dominant. Therefore, the difference in failure modes may be explained by hydrostatic stress effect. The failure behavior of the two materials is best fitted by a modified Tresca criterion. It is also noted that the EPON 826 epoxy shows much higher failure stress and larger elongation to failure, indicating much higher strength and toughness.

- The EPON 826 specimens are very consistent, with highly repeatable experimental results while the test results from the ColdCure epoxy specimens display a noticeable scatter from batch to batch, even within the same batch. This variability affects the predictive accuracy of the proposed constitutive model.

8.2 Constitutive Modeling

A new nonlinear viscoelastic model in differential form is proposed to overcome the drawbacks of the available models and to encompass the experimental observations of the deformation characteristics of the two tested epoxy resins. The new features of the model include:

- The model can distinguish between loading and unloading cases by introducing a current loading surface and a corresponding switch rule. For the loading cases, a stress-dependent modulus function is defined; for the unloading case the modulus is assumed to be constant and is equal to the value of the modulus function at the loading/unloading switch instant.

- A new definition of equivalent stress based on the Stassi equation is used to characterize a multiaxial stress state, especially the anisotropy in the tensile and compressive behaviors and the hydrostatic stress effect of epoxy resins.

- The model is relatively simple, it contains only five material constants, and a modulus function. The material constants and the modulus function can be easily determined from the uniaxial tensile creep curves at different stress levels through a routine procedure.

8.3 Model Predictions

The predictions of the proposed differential model have been compared with the comprehensive experimental data of the two epoxy resins, including creep, recovery, various transient loading/unloading paths, multiaxial stress states and non-proportional loading histories. Special attention was paid to the predictive capability of the model on the nonlinear viscoelastic behavior, hydrostatic stress effect, multiaxial behavior, as well as loading history effect.

A modified form of the Schapery integral model by Lai-Bakker is also included here for a comparison with the newly proposed differential model. The Schapery model and its modified forms are widely used in the prediction of the deformation and failure behavior of some polymers and fiber-reinforced composite materials because of its generality, simple data reduction procedure for determining material properties, as well as easy incorporation of the effect of temperature, moisture and physical aging.

The comparison between the model predictions and the experimental data for EPON 826/EPI-CURE 9551 and ColdCure epoxy systems shows:

- The newly proposed differential model is capable of capturing the deformation characteristics of the two epoxy resin systems, including the strong nonlinear behavior, hydrostatic stress effect, difference in uniaxial tensile and compressive, multiaxial behavior, as well as non-proportional loading histories. The predictions are in very good agreement with the experimental data for most loading cases, even at very high stress levels. However, the model cannot accurately predict the failure behaviors shown in the transient loading tests. This may be partially attributed to the occurrence of damage in the material which is not included in the current model. In general, the integral model tends to overestimate the stress responses for the strain-controlled tests and underestimate the strain responses for the stress-controlled tests.

- The newly proposed loading/unloading criterion for the differential model and the simple unloading rule for the modulus function can capture the unloading deformation

characteristics of the epoxy resins, while the integral model has no predictive capability for the unloading behavior.

- The predictions for the EPON 826 by the two constitutive models, especially the newly developed differential model, are much better that those for the ColdCure epoxy. Two reasons may explain the difference. The first reason is attributed to the different batches of the ColdCure epoxy resin. Since the material properties of polymers are strongly dependent on their production processes, the test results from different batches may vary. The other reason is attributed to the air bubbles trapped inside the specimens. The superior curing capability of ColdCure epoxy may be an advantage in some engineering applications, but it also impedes air bubbles from escaping. Trapped air bubbles change the microstructures of cured products and causes variations in material properties from specimen to specimen, even for the same batch.